A Master's Dissertation

# Investigation into the Steady-State Load Sharing of Weak Sources in a Low Voltage Three-Phase Islanded Microgrid

**Meng-Chun Merelda Wu**

A dissertation submitted to the Faculty of Engineering and the Built Environment, University of the Witwatersrand, in fulfilment of the requirements for the degree of Master of Science in Engineering.

Johannesburg, 2016

## DECLARATION

I declare that this dissertation is my own unaided work. It is being submitted for a Degree of Master of Science to the University of the Witwatersrand, Johannesburg. It has not previously been submitted for any degree or examination to any other university.

____________________________ ______________________

Meng-Chun Merelda Wu Date

# ABSTRACT

This research investigates the power sharing between distributed energy resources with voltage and frequency droop control. A case study based on voltage sources in an islanded microgrid is set up in the laboratory, referred to as: The Example Microgrid. The Example Microgrid consists of two synchronous generators, active and reactive power loads.

A simulation model is constructed based on the laboratory set-up, where component-wise and system-wise testing are completed. The simulation results are validated with the experimental set-up, and it is concluded that the model accurately represents the physical system under steady-state conditions. Further simulation studies on conventional droop controllers are conducted based on the Example Microgrid model. The results indicate that the use of conventional droop control is inappropriate for small, low-voltage islanded microgrids.

As a possible application of this work, three variations of adapted droop controllers are simulated and their performance evaluated. It is found that with the adapted droop controllers, the power sharing error can be minimised.

# ACKNOWLEDGEMENTS

The author would like to acknowledge her supervisors Prof. Willie Cronje and Dr. Mercy Shuma-Iwisi for their guidance and support, as well as Prof. Ian Hofsajer and Mr. James Braid for their valuable input. The author would also like to express her gratitude to the Machines Research Group and the staff in Genmin laboratory for their support towards this research.

The following organisations are gratefully acknowledged for funding and supporting this research:

- The National Research Foundation (NRF).
- ALSTOM through the Machines Research Group.

*To my loving family, and Pebbles.*

# CONTENTS

# LIST OF FIGURES

# LIST OF TABLES

# GLOSSARY

**Distributed Resources**

Local installation of generation sources of electric power that are not directly connected to a bulk power transmission system, including both generators and energy storage devices, which typically provides load control [7].

**Islanded Microgrid**

An electric power system that is not connected to the utility. It consists of distributed resources and loads that have the ability to operate autonomously [7].

**Load Sharing**

The sharing of both active power and reactive power load between generators. *Load Sharing* refers to the power sharing of loads based on the generators' output ratings.

**Load Sharing Test**

The specific test cases used in this research where the SGs are connected in parallel with the loads under various operating conditions in order to validate the Example Microgrid model.

**Load Test**

The specific test cases used in this research where the SGs are loaded independently under various operating conditions to validate the SG model and its parametrisation.

**Low Voltage**

A nominal AC voltage with an upper limit of 1000V.

**Point of Common Coupling**

The interface between sources and loads on an electrical system [7].

**Steady-state**

This research defines steady-state to be reached reached when the oscillation of voltage and frequency are sufficiently close to their nominal values.

**Three Phase**

A three phase system is investigated in this research. All diagrams are either in the single-line diagram form, or in the 3- or 4-wire representation unless otherwise stated.

**Weak grid**

A *Weak Grid* is characterised by a system with a high AC impedance and low mechanical inertia. An AC system of low strength is classified by having an Effective Short-Circuit Ratio (ESCR) of less than 3 [8].

**Weak Sources**

Weak sources imply that the sources have relative ratings to one another. The sources whose ratings are within ten times of one another are considered *Weak Sources*.

# ACRONYMS

| | |
|---|---|
| AVR | Automatic Voltage Regulator |
| DFIG | Doubly-Fed Induction Generator |
| DR | Distributed Resource |
| LPF | Low Pass Filter |
| LV | Low Voltage |
| MCB | Main Circuit Breaker |
| PCC | Point of Common Coupling |
| PE | Power Electronic |
| PID | Proportional Integral Derivative |
| PLL | Phase-Locked Loop |
| PST | Phase-Shifting Transformer |
| RM | Rotating Machine |
| SG | Synchronous Generator |
| VSD | Variable Speed Drive |
| VSI | Voltage Source Inverter |

# LIST OF SYMBOLS

| | |
|---|---|
| $I_a$ | Armature Current |
| $I_f$ | Field/Excitation Current |
| $J$ | Moment of Inertia |
| $L_m$ | Magnetising Inductance |
| $\omega$ | Rotational Speed |
| $P$ | Active Power |
| $Q$ | Reactive Power |
| $Q_c$ | Circulating Reactive Power |
| $IM_L$ | Induction Motor Load |
| $R_L$ | Resistive Load |
| $L_r$ | DFIG Rotor Leakage Inductance |
| $L_s$ | DFIG Stator Leakage Inductance |
| $R_r$ | DFIG Rotor Resistance |
| $T$ | Torque |
| $R_s$ | DFIG Stator Resistance |
| $S$ | Apparent Power |
| $R_{TL}$ | Resistive component of line impedance |
| emf | Electrio-motive force |
| $X_{TL}$ | Inductive component of line impedance |
| $Z_{TL}$ | Line Impedance |
| $I_1$ | Output Current of 75kW Generator |
| $I_2$ | Output Current of 22kW Generator |
| $V_1$ | Output Voltage of 75kW Generator |
| $V_2$ | Output Voltage of 22kW Generator |
| $V_{pcc}$ | Voltage at the Point of Common Coupling |
| $f$ | Frequency |

# CHAPTER 1

## Introduction

With an increase in energy demand around the world, Distributed Resources (DRs) emerge as an alternative solution to the conventional centralised electricity grid. A *Microgrid* is formed with an aggregation of these DRs as small-scaled and decentralised grid technologies. This creates a paradigm shift, where large power plants in a network are rapidly replaced by various DRs to form an intelligent, flexible and reliable grid. This research aims to investigate the load sharing between the DRs to allow for the stable and reliable operation of microgrids.

### 1.1 Background to Microgrid Research

With the benefits of reduced pollution, higher efficiency of energy utilisation, installation flexibility and less transmission losses, DRs have become increasingly popular worldwide. The majority of DRs are coupled via Power Electronic (PE) converters to connect to the grid, which introduces undesirable problems, such as system resonance and protection interference [9]. The *microgrid* concept is first proposed to resolve these problems by allowing for distributed power management through aggregating the DRs [9].

A typical microgrid architecture is shown in Figure 1.1, which integrates rotating micro-generators, converter-fed renewable energy sources, storages devices and electric and heat loads into a controllable system. The Main Circuit Breaker (MCB) separates the microgrid from the utility grid, forming an *islanded microgrid* that operates independently and autonomously from the latter [7, 9].

Even though microgrids are complex entities with numerous technological challenges, researchers around the world recognise the environmental and economical benefits and widely advocate their adoption. The potential is evident since the five most

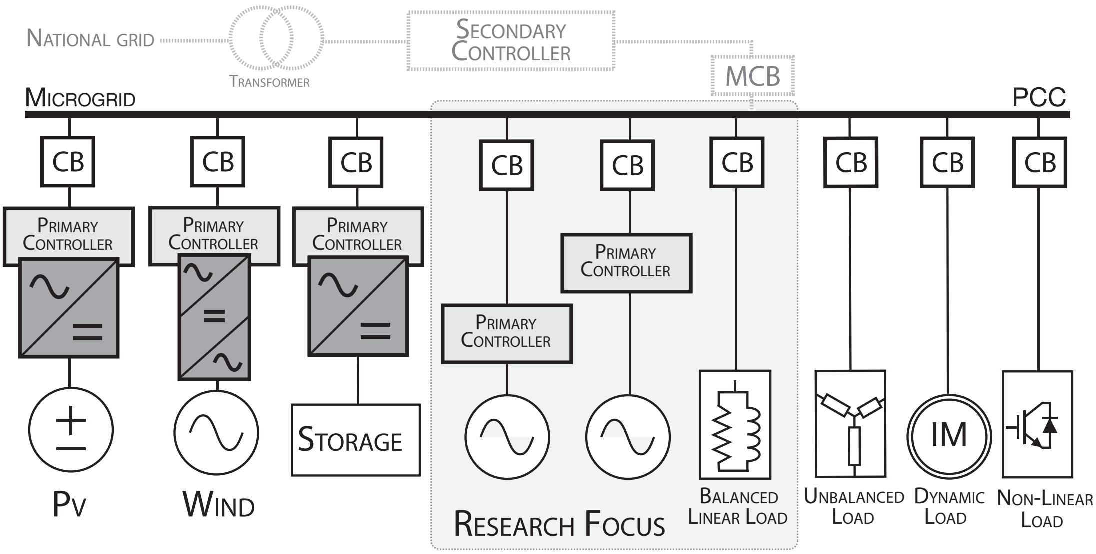


**Figure 1.1** A typical architecture of an Islanded Microgrid.

popular articles in *IEEE Power & Energy Magazines* are smart grid and microgrid related topics [10–14]. Table 1.1[1] includes common research topics and separates them into various fields, including Control and Power Management, Fault and Protection Studies, Power Electronics, Network and Communications and others.

**Table 1.1** Common research topics in microgrids.

| Control | Protection | PE | Telecom | Others |
|---|---|---|---|---|
| PQ Control | Fault Detection | Inverters | Protocols | Topology |
| Vf Control | Protection | Converter | Infrastructures | Planning |
| Load Control | False Tripping | Storage | Standard | Power Flow |
| Black Start | Recloser | FACTS | Network | Economics |
| Islanding | Groundings | Power Quality | Metering | Load Profile |
| Synchronising | Stability | Chargers | | Scheduling |

This research aims to investigate the load sharing between DRs. To ensure that the load power is shared proportionally between the DRs, the droop control method is most commonly adopted [9, 14–16]. Droop control is developed for synchronous generators in conventional power plants, where the generators are located in close proximity and distribution takes place via high voltage cables [17]. An islanded microgrid is typically a low voltage power grid where the generation, transmission and distribution are dispersed within a local network. The resistive-dominant line impedance for low voltage cables results in a couple effect between the active and reactive power, reducing the efficacy of conventional droop controllers in islanded microgrids.

[1]These topics are selected based on the popular papers related to the microgrid and smart grid topic in the *IEEE Power & Energy Magazine*.

## 1.2 Overview of Dissertation

*Chapter 2* discusses the ***background*** that is associated with islanded microgrids. The common assumptions for islanded microgrids research are identified from a literature survey. The generator speed and voltage control, as well as droop control are presented. The challenges in load sharing are identified and the existing solutions are summarised.

*Chapter 3* evaluates the ***methodology*** adopted by this research. The problem statement is first presented and the methodology is subsequently discussed with distinct research objectives. The ***Example Microgrid*** case study is proposed based on the assumptions and research objectives.

*Chapter 4* describes the ***experimental set-up*** of the Example Microgrid. The microgrid components, including the generators, loads, line impedance and auxiliary devices are described in detail. The physical operation of the experiments and the instrumentation set-up are discussed.

*Chapter 5* describes the ***simulation set-up*** of the Example Microgrid. The modelling of the components are explained in detail and the models of the generators are validated by comparing the simulation and experimental results of the generator's load test.

*Chapter 6* presents the ***results*** of the various experiments conducted. The Example Microgrid simulation model is validated through corroborating the simulation and experimental results. In addition, the experiments demonstrate the effects of a resistive line impedance on weak sources. The limitations of the set-up are evaluated and the boundary conditions for an accurate simulation are identified.

*Chapter 7* analyses the ***load sharing*** in an islanded microgrid through conducting further simulations. The effects of a resistive line impedance on conventional droop controllers are highlighted and the probable parameters that may affect the efficacy of the controllers are investigated. The voltage and frequency regulation of an islanded microgrid is discussed in light of these results.

*Chapter 8* presents the possible application of this work, which is to study different ***primary control*** strategies. Three variations of droop controllers are simulated in the Example Microgrid and their trade-offs discussed.

*Chapter 9* provides a ***review*** of the work conducted based on the success of the deliverables on the research objectives. Considerations for improving the work, as well as extensions of the work, are proposed as ***future work***.

*Appendix A* includes ***additional background*** on the research. The summary of assumptions based on the 10 most cited islanded microgrid papers, as well as the mathematical derivation of droop equations in low voltage grids, is provided.

*Appendix B* summarises the ***experimental set-up*** of the Example Microgrid in the laboratory. The complete wiring diagram, instrumentation list, and photographs of the set-up are included. The settings for the ***simulation environment*** options are also included.

*Appendix C* includes the ***parameter estimation*** procedure of the SGs used in the Example Microgrid. Additional ***results*** of the SG Load Tests at 180 $V_L$ are included and the trade-offs between using the asynchronous machine and synchronous machine Simulink block are discussed.

*Appendix D* includes additional ***experimental results*** of the Example Microgrid. Supporting graphs are shown for the Example Microgrid operating at both 180 $V_L$ and 120 $V_L$. The drawbacks of operating the Example Microgrid at 180 $V_L$ are discussed in light of the magnetic saturation of the SGs.

# CHAPTER 2

# Research Background

This chapter contextualises this research by first introducing the islanded microgrid, then the DRs within the islanded microgrid and finally the primary control of the DRs. The scope of the research problem is first outlined through reviewing the extensive work in the islanded microgrid field. The formulation of droop control is presented and its limitations and existing solutions are subsequently discussed. The challenges in droop control in islanded microgrids are identified and the existing solutions compared and contrasted.

## 2.1 Introduction

To approach a general standardisation of microgirds, hierarchical control is proposed by *Guerrero et al.* that consists of three levels [18]: (1) The primary control includes voltage and frequency regulation as well as load sharing control, (2) the secondary control restores the voltage and frequency deviation produced by the primary control, as well as the synchronisation with surrounding electrical grids, (3) the tertiary control manages the power flow between the microgrid and its distribution system. The primary control is achieved locally at each DR and the secondary control is implemented at a bus where there is an aggregation of DRs [18]. Figure 1.1 shows the location of the primary and secondary controller in a microgrid.

## 2.2 Common Assumptions Identified in Literature Survey

This section forms the cornerstone of the Example Microgrid that is proposed in Chapter 4. The identifications of these assumptions prevent the proposed microgrid to be too far removed from the work of others. This also allows for the subsequent investigation of the experimental and simulation results to be compared with similar studies.

To identify and understand the common assumptions that are prevalent in the field of islanded microgrids, a survey of the most cited papers [1] [3, 15, 19–26] is conducted. In order to focus the scope on islanded microgrids, only papers that are directly related to this research are reviewed.

Papers that discuss primary control and load sharing in islanded microgrids are summarised, whereas topics such as black start and resynchronisation, fault detection and protection, or economic dispatch are not included. This means that certain assumptions only hold true for this work in order to examine the effects of primary control on load sharing.

From the survey, various assumptions are recognised. These assumptions are grouped into three categories and presented in Table 2.1: system simplifications, engineering design choices and observations on early islanded microgrid research.

**Table 2.1** Common assumptions of islanded microgrid operating conditions.

| | **Simplifications** | **Design Choices** | **Observations** |
|---|---|---|---|
| 1 | Balanced, 3$\phi$ Loads | No Communication | LV Grid |
| 2 | Generation-Load Balance | Two-mode Operation | PE-based |
| 3 | Fast Transients Neglected | Droop Control | At least one VSI |

For the sections below, each assumption is denoted with the number of papers that adopts it. For example, (7/10) means that 7 out of the 10 papers surveyed are in agreement with that particular assumption. The actual reference is tabulated in Table A.1 in Appendix A to prevent spurious citation.

### 2.2.1 Assumptions based on Simplifications

Three assumptions are commonly made to minimise the computation time, simplify engineering problems, or both.

- A microgrid has balanced three-phase loads. (7/10)
- There is sufficient energy to achieve generation-load balance. (7/10)
- Fast transients are either not examined or ignored. (10/10)

Out of the three papers that do not consider balanced three-phase loads, two were examining single-phase microgrids, which assumed the controller can be extended to three-phase. In addition, although *Majumder et al.* [24] includes unbalanced

[1] Only the papers published in the past decade are considered and the number of citations are extracted on IEEE Xplore as of July 2014.

local loads for each DR, only balanced three-phase loads are being shared between multiple DRs.

In a PE-based microgrid with little or no spinning reserve, disturbances may lead to large deviations during transients. Most references assume that there is enough generation to supply the load, either via storage devices with a large capacity, or a load shedding approach must be taken. The references that do not assume a generation-load balance acknowledges the effect of frequency sag when imbalances occur, but did not provide a strategy to mitigate the effect.

All the referenced papers focus on the dynamics of a microgrid, such as the energy balance and the response of the primary control. These dynamics occur in the milliseconds to seconds time range, therefore transients that are shorter or effects that take longer to manifest are not examined. For example, the switching transients of inverters and the mechanical vibrations of generators are neglected. This allows the inverters to be modelled based on their control functions without affecting the power simulation results [15].

### 2.2.2 Assumptions based on Design Choices

Common design choices that are made in the literature:

- Primary control does not involve any communication. (6/10)
- Load sharing is achieved through some form of droop control. (10/10)
- A two-mode operation, i.e. islanded and grid-connected mode. (10/10)

Most of the references acknowledge that a communication network incurs an extra cost and maintenance to a microgrid, therefore only local information should be used to regulate the voltage and frequency at each DR. *Kim et al.* [20] proposes the use of low bandwidth communication to achieve both active and reactive load sharing, while *Majumder et al.* [21] uses communication to change the inverter control mode. *Li and Kao* [3] suggest an add-on communication layer for more accurate sharing, and *Kim et al.* [23] uses communication only for reactive power management.

Droop control is adopted for all the surveyed papers to achieve proportional load sharing, although different variations are proposed. Further discussion of the droop control is included in Section 2.4.

All the surveyed papers assume that a microgrid has to be able to operate in both islanded and grid-connected mode. The intended microgrid application for this dissertation is aimed towards a remote rural community. Since the possibilities of being connected to the national grid is minimal, it is unnecessary to provide provision for connections to the utility grid. In this research, only the islanded operation is investigated.

### 2.2.3 Assumptions based on Observations

Through mathematical analysis, simulations and experimentations, a couple of observations have been made by various authors. These observations impact the fundamental engineering decisions in designing a microgrid. The three that directly concern this research include:

- An islanded microgrid is a low-voltage grid. (8/10)
- A microgrid consists mainly of PE-based sources. (10/10)
- At least one Voltage Source Inverter (VSI) is used if a rotating machine is not available. (10/10)

It is observed that since microgrids provide power to a local network, low voltage lines are used. This renders the conventional droop control ineffective, resulting in unproportional or inaccurate load sharing due active power and reactive power coupling.

All the literature assumes that microgrids mainly consist of PE-based sources. This means that there is a lack of rotating inertia, hence poor voltage and frequency regulation ability. As a result, an energy storage device with a large capacity is essential in regulating the voltage and frequency. All the PE-based sources are required to be equipped with an inverter, and at least one VSI is required in synthesising the voltage at the desired amplitude and frequency.

## 2.3 Generators as the Primary Source

The common sources in a microgrid are directly-coupled Rotating Machines (RMs), PE-based inverters, and inverters coupled with RMs. The state-of-the-art microgrid assumes a majority of PE-based resources as they offer higher controllability, faster response time, and integrated protection mechanism [27]. Although it is beneficial to examine the load sharing of inverters in an islanded microgrid as they are the state-of-the-art sources, the university laboratory does not have islanding inverters available for experimentation.

This section discusses the properties of the three common sources. Through such, the choice of using doubly-fed induction generator operating as separately-excited synchronous generator as the generation source in this research is rationalised.

*Inverters*

Depending on the output waveform, inverters can be classified as either Voltage Source Inverters (VSIs) or Current Source Inverters (CSIs). VSIs have a low output impedance and produce a controlled voltage waveform, whereas CSIs have a high output impedance and produce a controlled current waveform [28]. Furthermore, inverters with grid-forming controls are classified as VSIs and others with grid-feeding controls are classified as CSIs [29]. Table 2.2 summarises the four types of inverter controls and their characteristics [29].

**Table 2.2** Classification of Inverter Controls

| **Inverter** | **Type** | **Characteristic** |
|---|---|---|
| Grid-Forming | VS | Cannot parallel with other VS, therefore often in standalone applications |
| Grid-Feeding | CS | Require grid-forming voltage sources in the grid |
| Grid-Supporting-Grid-Forming | VS | Able to parallel with both voltage and current sources |
| Grid-Supporting-Grid-Feeding | CS | Require Grid-forming voltage sources in the grid |

Grid-supporting-grid-feeding inverters are droop controlled current sources, which are typically driven with phase-locked-loops and require another voltage source in the grid for voltage regulation [29]. Grid-supporting-grid-forming inverters are droop controlled voltage sources, which allow them to be paralleled with other voltage sources [29].

PE-based grids have a much faster response time than conventional RM-based grids [30]. The fast response time of an inverter poses a significant challenge in limiting the drop of the system frequency during large load steps. The lack of spinning reserve to supplement the sudden increase in power demand may cause the system to lose synchronisation. As a result, a large capacity storage device is necessary to improve the stability and reliability of a microgrid [30].

Several authors propose the use of at least one storage device equipped with a VSI to emulate a synchronous generator [23, 30–32]. The state-of-the-art VSIs in an islanded microgrid are typically engineered to mimic a generator's droop response. This feature allows the VSI to behave as a more flexible synchronous generator.

*Synchronous Generators*

Synchronous generators are the principal source of electrical energy in power systems [8]. They are desirable because their output voltage and frequency can be controlled directly through the field excitation and shaft speed [8]. In addition, compared to the stochastic nature of renewable energy, a generator is able to provide a constant output when given sufficient fuel. This makes it an ideal source in an islanded microgrid, supplying energy to critical loads as the renewable energy fluctuates.

Synchronous generators are therefore widely installed as backup, emergency power supplies in private and commercial settings, or as standalone generators in remote areas [33]. Other than being used with traditional high power turbines, the most prevalent set-up in a microgrid is a genset, which is a diesel engine coupled with a separately-excited wound field synchronous generator [29].

#### *Doubly-Fed Induction Generators*

Doubly-Fed Induction Generators (DFIGs) are often coupled with back-to-back converters with wind turbines as prime movers, because both the stator and rotor terminals of DFIGs can be accessed externally [34–36]. The rotor-side converter is connected to the slip rings, controlling the excitation of the rotor [36]. The grid-side converter regulates the voltage of the DC bus, while supporting the voltage of the grid by generating and absorbing reactive power [36].

Since the rotor terminals are externally accessible, the DFIGs can also be configured as synchronous generators. Instead of exciting the rotor with a three-phase AC voltage, a DC excitation can be used to directly control the stator voltage. The mechanical energy of a DFIG is provided by its coupled prime mover, while the speed is controlled by a speed governor on the prime mover. This arrangement allows a DFIG to act fundamentally as a synchronous generator with three-phase output voltage operating at synchronous speed.

Although both voltage and current source inverters may be present in an islanded micrgorid, there will be at least one grid-forming voltage source present either as a synchronous generator or as a VSI. In addition, current sources can be easily paralleled with a voltage source. Therefore, the laboratory work of this research focuses on voltage sources. Since the load sharing control of inverters is based on droop control for generators, it is argued that investigating the load sharing of synchronous generators is the first step in understanding the load sharing in a microgrid with different forms of sources.

DFIGs are the only available generators in the laboratory, they are configured to operate as synchronous generators and selected as the primary source in this research. The detail of this set-up is described in Chapter 4 and the next section describes the generic voltage and speed control for synchronous generators.

## 2.4 Primary Control in Islanded Microgrids

The operating mode of a generator in an islanded microgrid is first identified in this section. With the understanding of the operation, the primary control strategies are subsequently defined: both voltage and frequency regulation as well as load sharing control are required.

### 2.4.1 Operation Mode of an Islanded Microgrid

A grid-feeding source aims to inject sinusoidal current into the grid, while a grid-forming source controls the amplitude, frequency and phase of the sinusoidal voltage. Generators as grid-forming voltage sources adopt different control strategies when operating under different modes. Table 2.3 summarises the three different operating modes a generator can have as a voltage source: (1) a standalone generator, (2) a generator connected to an infinite bus, and (3) generators paralleled in a weak grid [37].

When a generator operates in standalone mode, the apparent power supplied by the generator is fixed by the demand of the load. In this mode, increasing the shaft speed of the generator increases the frequency of the grid and increasing the back terminal voltage of the generator raises the grid voltage.

On the other hand, when a generator feeds into an infinite bus, the frequency and terminal voltage are fixed. Changing the generator shaft speed (output torque) changes the real power. The reactive power flow is varied through changing the field voltage of the generator.

**Table 2.3** Operating conditions of the generators.

| **Operation Mode** | **1. Standalone** | **2. Infinite Bus** | **3. Parallel** | |
|---|---|---|---|---|
| Affected Generator | 1/2 | 1 & 2 | 1 | 2 |
| Fixed Parameters | $P, Q$ | $V, f$ | $P_1 + P_2 = P_{load}$<br>$Q_1 + Q_2 = Q_{load}$ | |
| ↑ Speed | $f \uparrow$ | $P \uparrow$ | $f_1 \uparrow, f \uparrow$<br>$P_1 \uparrow P_2 \downarrow$ | $f_2 \uparrow, f \uparrow$<br>$P_2 \uparrow P_1 \downarrow$ |
| ↑ emf | $V \uparrow$ | $Q \uparrow$ | $V_1 \uparrow, V \uparrow$<br>$Q_1 \uparrow Q_2 \downarrow$ | $V_2 \uparrow, V \uparrow$<br>$Q_2 \uparrow Q_1 \downarrow$ |

Figure 2.1 depicts the a typical islanded microgrid, which is the third operation mode. When two generators are paralleled in a weak grid, there are many variables that are dependent on one another. The only fixed parameter in this system is that the sum of real and reactive powers between the two generators must be equal to

the load demand. Note that $V_i, f_i, P_i, Q_i$ are variables for the individual generators, whereas V, f are the value at the PCC. The frequency and terminal voltages are not fixed and more importantly, the individual active and reactive powers delivered by the generators are also not constrained.

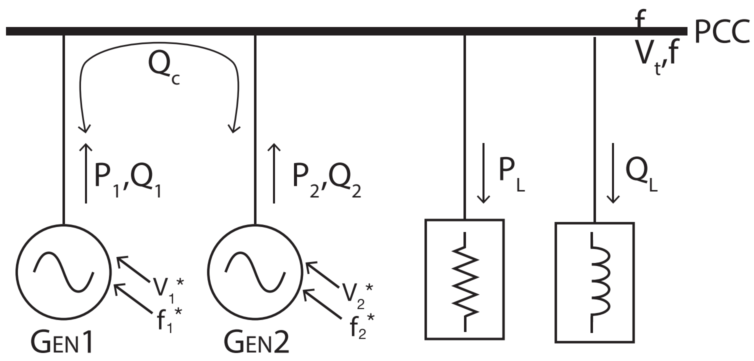


**Figure 2.1** Generators paralleled in a weak (islanded) grid.

The primary control of islanded microgrids is difficult since they are classified as weak electrical grids. A weak electrical grid has an effective short-circuit ratio less than 3, which means that it has a high AC impedance and a low mechanical inertia [8]. Therefore, there is a lack of swing bus to act as the buffer to absorb and provide any excess and deficit active and reactive power, making the voltage and frequency regulation more challenging.

In the paralleled mode, each generator is required to regulate their voltage and frequency in a weak grid [38], as well as to properly (generally proportionally) share the load demand. Usually, the droop control method is adopted for proportional load sharing, eliminating the use of critical communication networks.

### 2.4.2 Generator Control: Voltage and Frequency Regulation

DFIGs configured as synchronous generators are used in this research. It is important to note that the fundamental operating principles between DFIGs and synchronous generators are the same. Figure 2.2 shows the block diagram of the control of gensets. In this section, the speed governor and the Automatic Voltage Regulator (AVR) are discussed, while the next section presents the PF- and QV-droop control.

Conventionally, synchronous generators operate in parallel and feed power into an infinite bus, which requires controllers to keep the voltage and frequency within a tight margin [2]. The requirements for islanded operation is not as strict as grid-

[2]IEEE 1547.4 specifies the grid-connected steady-state frequency to be within 0.05Hz [7]. In addition, various abnormal frequencies and voltages must be cleared within a certain time according to Table 1 and Table 2 respectively in IEEE 1547-2003 [7].

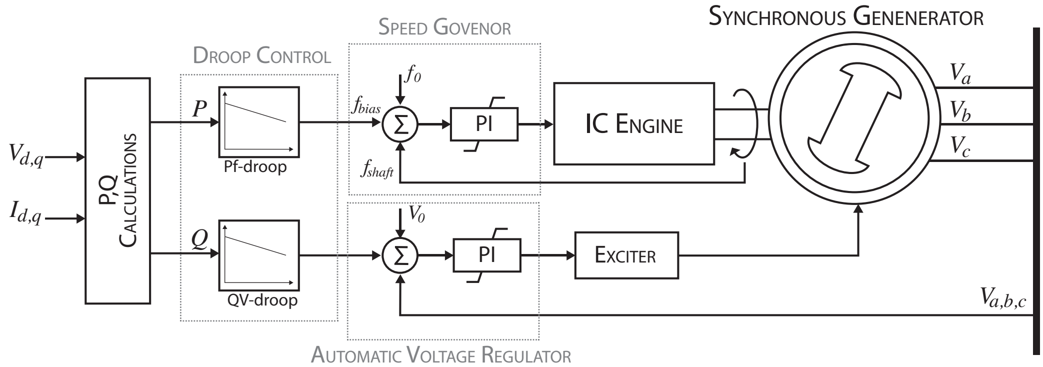


**Figure 2.2** Synchronous generator with AVR and speed governor, adapted from Figure 11 of [1] and Figure 6.1 of [2].

connected mode, but the voltage and frequency still need to be regulated to ensure a reliable operation [7]. A genset typically consists of a wound-field synchronous generator and an internal combustion engine as the prime mover [1]. The speed governor acts on the engine to regulate the frequency, while the AVR acts on the exciter to regulate voltage.

An exciter is the power supply for the synchronous generator field excitation. The AVR controls the exciter with a Proportional Integral Derivative (PID) controller, where the negative-feedback is used to track the voltage set-points. By controlling the exciter, the emf and hence the stator voltage of synchronous generator can be controlled [8]. This means that the DC currents in the field (rotor) windings control the voltage of the armature (stator) windings [8].

The speed governor controls the throttling of the engine, which is also achieved with a PID controller [1]. Negative feedback is used to track the speed set-point as well as to achieve zero steady-state errors, as shown in Figure 2.2 [39].

### 2.4.3 Conventional Droop Control: Load Sharing

For controlling DRs in islanded microgrids, communication-based control, such as master/slave or central control [18, 20], can be used. However, for microgrids with reliability and modularity in mind, droop control is the preferred solution [16, 23, 40, 41]. This section presents the formulation of conventional droop controllers on the balancing and sharing of the fundamental active and reactive power, as well as discusses its performance in an islanded microgrid.

Droop control is a mechanism used in conventional power systems to allow generators operating in parallel to share the load according to their power ratings. PF-droop defines the output power of each source based on its frequency droop curve, allowing the sharing of loads between the generators with changing grid frequency.

Although the frequency is designed to sag in order to support active power, the voltage is conventionally regulated at a constant value [29]. This may introduce a large circulating reactive current when the DRs operating in an islanded condition have incorrect voltage references [42]. The circulating reactive power not only decreases the efficiency and increases component ratings, it may also cause a loss of synchronism during a disturbance [42].

To alleviate this effect, the Reactive Power to Voltage (QV-droop) is often employed in an islanded microgrid [29]. Droop control is the most popular way to provide stable real and reactive power sharing without the use of a communication system [9, 29].

### Droop Control Derivation

The droop equation is formulated by considering the active and reactive power flow between two AC voltage sources separated by a line impedance ($Ze^{j\theta} = R + jX$), as illustrated in Figure 2.3.

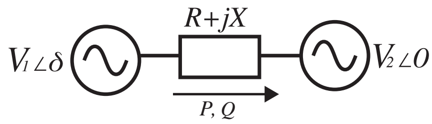


**Figure 2.3** Power flow between two voltage sources linked by a line impedance.

The real and reactive power can therefore be expressed as [8]:

$$\begin{aligned} P &= \frac{V_1}{R^2 + X^2}[\ R(V_1 - V_2\cos\delta) + XV_2\sin\delta] \\ Q &= \frac{V_1}{R^2 + X^2}[-R\ V_2\sin\delta + X(V_1 - V_2\cos\delta)] \end{aligned} \tag{2.1}$$

where $V_1, V_2$ are the voltages of the two sources, and $\delta$ is the phase angle difference between them. The line impedance is separated into the resistive and reactive components $R$ and $jX$. In conventional droop control formulation, two assumptions are made [3, 8, 26, 43–45]:

> *Assumption 1: The line resistance (R) is often neglected.* In conventional grids, the impedances representing the HV transmission lines, transformers and generators are inductive-dominated.
>
> *Assumption 2: The angle $\delta$ is small.* As two generators are synchronised, the phase difference between the two generators are small. This allows the small angle approximation and the simplification of $\sin\delta = \delta$ and $\cos\delta = 1$ can be used.

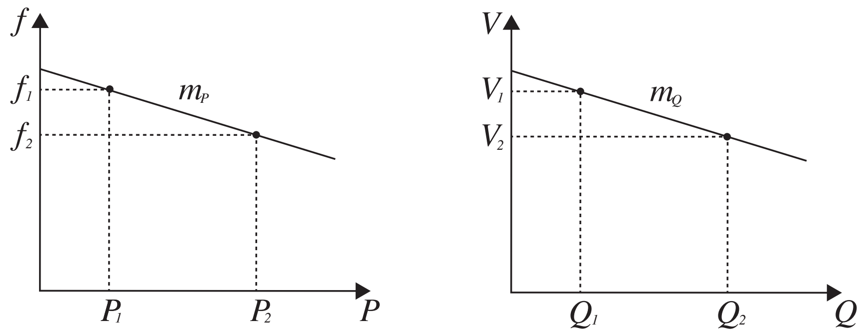


**a.** Power to Frequency droop. **b.** Reactive Power to Voltage droop.

**Figure 2.4** Droop control for distributed generators.

With the two assumptions stated above, Eq.(2.1) is simplified to [8]:

$$\begin{aligned} P &= \frac{V_1\ V_2}{X}\delta \\ Q &= \frac{V_1}{X}(V_1 - V_2) \end{aligned} \tag{2.2}$$

From Eq.(2.2), the generator output real power (P) is proportional to the phase angle difference (i.e. $P \propto \delta$) and the generator output reactive power (Q) is proportional to the voltage magnitude difference (i.e. $Q \propto (V_1 - V_2)$). Since the phase angle difference is difficult to obtain in practice, the output frequency is used to control the active power by varying the shaft speed with the speed governor, as shown in Figure 2.4 (a). Similarly, the generator excitation current is used to control the reactive power through the AVR, as illustrated in Figure 2.4 (b). It is shown that the frequency decreases as the active power increases and the voltage varies as the reactive power changes from capacitive to inductive.

### Power to Frequency (PF-) Droop

With the power flow equation simplified to Eq.(2.2), the droop equation is formed [3]:

$$\begin{aligned} \omega_i &= \omega^* + m_{P_i}(P_i - P_i^*) \\ m_{P_i} &= \frac{\omega^* - \omega_{min}}{P_i^* - P_{i,max}} \end{aligned} \tag{2.3}$$

where $\omega_i$ and $P_i$ are the actual frequency and the actual real power output for generator $i$ ($i = 1, 2, ...n$). $\omega^*$ and $P_i^*$ denote the dispatched operating frequency and the real power of generator $i$, respectively. $P_{i,max}$ is the rated power of the generator $i$, $\omega_{min}$ is the minimum operating frequency of the grid and $m_{P_i}(< 0)$ is the droop slope.

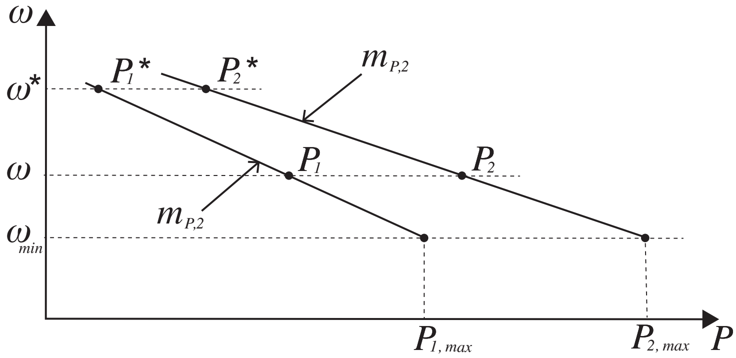


**Figure 2.5** Active power sharing through PF-Droop, adapted from Figure 2 of *Li and Kao* [3].

To demonstrate the droop concept, Figure 2.5 illustrates the real power sharing between two generators. The two generators are initially operating at $\omega^*$, dispatching power $P_1^*$ and $P_2^*$ to the loads. With an increase in load demand, the two generators droop to a lower system frequency $\omega$ according to their droop characteristics, hence increasing their output power $(P_1, P_2)$ and allowing the proportionality to be maintained.

*Droop Coefficients for Proportional Load Sharing*

To choose the droop coefficients for proportional load sharing, consider a two-generator system that experiences a change in active power demand from no load to full load. Based on Eq.(2.3), the response can be written as:

$$\begin{aligned} \Delta\omega_1 &= m_{P_1}\ P_{1,max} \\ \Delta\omega_2 &= m_{P_2}\ P_{2,max} \end{aligned} \tag{2.4}$$

where $\omega_i, P_i$ are the individual rotational frequency and power of the generators. $P_{i,max}$ is the maximum active power of the generator, which is typically 80% of the nameplate rating for a synchronous generator. $\omega_{min}$ is specified by the islanded microgrid operator, which is defined as 0.97 p.u. for this research as discussed in Table 8.1.

Since the two generators are locked in synchronism and are connected in parallel, the change in frequency is identical, i.e. $\Delta\omega_1 = \Delta\omega_2$. As a result, in order to achieve a proportional active power sharing, the droop slopes of the generators must be indirectly proportional to their power ratings [45]:

$$\frac{m_{P_1}}{m_{P_2}} = \frac{P_{2,max}}{P_{1,max}} \tag{2.5}$$

### Reactive Power to Voltage (QV-) Droop

Similar to the PF-droop, the QV-droop characteristic can be expressed as [3]:

$$\begin{aligned} V_i &= V^* + m_{Q_i}(Q_i - Q_i^*) \\ m_{Q_i} &= \frac{V^* - V_{min}}{Q_i^* - Q_{i,max}} \end{aligned} \tag{2.6}$$

where $Q_i$ and $V_i$ are the actual voltage and the actual reactive power outputs of generator $i$ ($i = 1, 2, ...n$). $V^*$ and $Q_i^*$ denote the dispatched operating voltage and reactive power of generator $i$, respectively. $Q_{i,max}$ is the rated power of generator $i$, $V_{min}$ is the minimum operating voltage of the grid, and $m_{Q_i}(< 0)$ is the droop slope.

From Eq.(2.2), the reactive power does not have a direct relationship with voltage, but rather the difference in voltage magnitude ($V_1 - V_2$). Therefore, active power sharing is easily achieved through droop control, but reactive power sharing is less accurate due to unequal and resistive-dominant line impedances.

## 2.5 Load Sharing Challenges in Islanded Microgrids

The greatest challenge in achieving proportional load sharing in an islanded microgrid is due to the Low Voltage (LV) power cables. The resistive-dominant line impedances of the LV power cables result in an undesirable active and reactive power coupling, as well as an increase in the reactive power sharing error. These effects are reviewed in this section to provide a benchmark for the results obtained in this research.

### 2.5.1 Active and Reactive Power Coupling

Droop control is effective in achieving load sharing between generators; however, the theory is developed based on large synchronous generators exporting power via high voltage transmission lines. In a low voltage microgrid, the assumption of an inductive-dominant line impedance is invalid, as seen in Table 2.4 [17, 40].

**Table 2.4** Typical characteristics of small, medium and large power system.

| **Grid Size** | **Grid Characteristics** | | | |
|---|---|---|---|---|
| | Line Type | $R + jX$ ($\Omega/km$) | X/R | Dominant Term |
| Large | HV line | $0.060 + j\ 0.191$ | 3.18 | $X \gg R$ |
| Medium | MV line | $0.161 + j\ 0.190$ | 1.18 | $X \approx R$ |
| Small | LV line | $0.642 + j\ 0.083$ | 0.13 | $X \ll R$ |

When the X/R ratio of the line impedance is below 0.5, the line exhibits resistive characteristics [8]. This means that the assumption of $X \gg R$ cannot be used, hence the line resistances cannot be neglected. This creates an undesirable coupling effect between the active and reactive power, resulting in an inaccurate load sharing. Therefore, conventional droop control cannot be applied in resistive-dominant line impedances. The amount of coupling is dependent on the line impedance angle, given by $\theta = \arctan \frac{X}{R}$ [46].

### 2.5.2 Reactive Power Sharing Error

*Gu et al.* [47] derive the droop control transfer function, and find that the active power of the generator is dependent only on well-defined parameters: its active power reference ($P_i^*$), angular frequency ($\omega_i^*$) and droop coefficient ($m_i$). This means that by setting these three parameters correctly, an active power load sharing can be achieved.

Contrary to the PF-droop, where the steady-state frequency of the grid is constant across all the DRs, the voltage at the output of each DR is not the same for the QV-droop. The reactive power is dependent on not only its well-defined parameters, $Q_i^*, E_i, n_i$, but other variables too. Appendix A includes the derivations of the equations that show the dependency of these parameters. Researchers including *Gu et al., He and Li* [47, 48] identify that the reactive power sharing is affected by the existence of local loads, unequal voltage drops on impedances, and variations of the droop slope. In addition, other researchers identify that unequal line impedances between generators and loads have a large impact on the accuracy of load sharing due to unequal voltage drops [3, 15, 24].

The parameters that affect load sharing are obtained from complex mathematical derivations; however, the extent and significance of each parameter have not been explored.

## 2.6 Variations of Droop Control

In order to improve the accuracy of proportional load sharing in LV islanded microgrids, variations of droop control have been proposed. This section reviews the adapted droop control strategies and Chapter 8 implements two of the strategies based on the analysis presented.

Although most of the top 10 papers agree that RMs are likely to exist in a microgrid, only *Li and Kao* [3] provide provisions in designing the control for generators that can be directly coupled to the microgrid. This is because inverters do not have the physical limitations as machines with rotating inertia, therefore different variations of droop control can be easily implemented.

The most popular approach amongst inverters is the use of virtual impedance to decouple the active and reactive power [3, 46, 49]. This method is effective in power decoupling, but without additional compensation mechanisms it may worsen the reactive power sharing error [3].

Different droop variations are proposed for inverters using a virtual output impedance. The QV- and PF-droop are used when the inverter output impedance is inductive, whereas the Qf- and PV-droop are used when the output impedance is resistive [25, 26, 49]. Another variation is the Power to Angle (P$\delta$-) droop, where the phase angle of the DR, relative to the grid, is drooped [21, 41].

Inverters equipped with these variations of droop control cannot be used with synchronous generators due to machine loading characteristics. The inherent droop of frequency when the active power demand increases makes the synchronous generator unable to adapt to different droop variations.

There are also different variations of droop controls that are applicable to RMs found in literature. The techniques include line impedance compensation [17], the use of communication [3, 44], frame transformation [50], signal injection [48, 51] and online estimation of voltage drop [3].

*De Brabandere et al.* [52] propose an orthogonal linear rotational transformation technique to decouple the active and reactive power through the coupling impedance. This method is ineffective when the line resistance and inductance are comparable with one another [44]. In addition, even when the decoupling is successful, the proportional sharing of active and reactive power cannot be directly achieved [3].

The signal injection technique adjusts the output voltage according to an estimated reactive power sharing error. The estimation of the reactive power sharing error is done by comparing the system response before and after a small control signal (such as an active power harmonic) is injected into the grid [48, 53]. A variation of the signal injection technique aims to estimate the grid impedance through intentionally varying the output active and reactive power of the DRs [51]. This method relies on a large enough excitation for an accurate impedance estimation, which is difficult to achieve in practice. The complexity of the signal injection technique increases drastically and the power quality may be severely degraded due to voltage and current distortions [3].

*Li and Kao* [3] propose to bias the voltage set-point by the ratio of voltage line drop to reactive power. As this ratio is estimated during the grid-connected mode, it is therefore invalid for the islanded microgrid proposed for this research.

*Engler and Soultanis* [17] suggest biasing the voltage set-point of the QV-droop control with the voltage drop across the estimated line impedance. This method is effective provided that the characteristics of the line impedance are known and accurate. This however, is difficult to obtain in practice, especially in a complex power network.

The use of low-bandwidth communication on top of the droop control is recommended to improve the reactive power sharing [3, 44]. This method is the most effective, but has the disadvantage of incurring additional costs in the installation of the extra communication layer. The robustness of the droop control is also compromised.

## 2.7 Summary

The common assumptions in the research of islanded microgrids are identified based on simplifications, observations and design choices. Certain assumptions are adopted in order to allow this work to be comparable to the work of others. This research investigates a balanced, three-phase low voltage islanded microgrid. The generation is assumed to be sufficient within the operating conditions, and droop control is chosen as the load sharing strategy.

SGs are selected as the primary source used in this research. The speed governing control, voltage regulation with AVR and droop control of a genset are discussed. Droop control is developed to allow large synchronous generators to achieve proportional load sharing in conventional power grids. The resistive-dominant line impedance in LV islanded microgrids reduces the efficacy of droop controllers. The undesirable active and reactive power coupling, as well as a poor reactive power sharing between DRs may render the conventional droop controller ineffective. However, the extent of the effect and the parameters that causes these effects are not discussed in the literature.

Different variations of droop controllers are discussed, each with varying degrees of complexity and success. However, the majority of the droop controllers proposed are for inverters in a PE-based microgrid. The strategies that are applicable for generators include: frame transformation, signal injection, online estimation of voltage drop, line impedance compensation and the use of a communication network. The line impedance compensation and the use of a communication network are explored in Chapter 8.

This chapter reviews the state-of-the-art microgrid research with the background of conventional load sharing control. Based on the literature survey performed in this chapter, a case study islanded microgrid is proposed in the following chapter to meet the research objectives.

# CHAPTER 3

## Research Methodology

This chapter discusses the methodology adopted for the feasibility and limitations on the execution of this research. The problem is first stated based on the literature survey and the research objectives are subsequently outlined. With the envisaged application in mind, an islanded microgrid case study is proposed as the Example Microgrid. The methodology of this work is discussed and its feasibility and limitations are analysed.

### 3.1 Problem Statement

The architecture of an islanded microgrid is significantly different from the utility grid, challenging the conventional means of sharing active and reactive power between DRs. Droop control has been used for decades in the utility grid to achieve a desirable load sharing profile between large synchronous generators. In an islanded microgrid, the unequal, resistive-dominant line impedance results in undesirable active and reactive power coupling as well as reactive power sharing error between DRs.

To illustrate this effect, two generators with relative ratings to one another are connected in parallel with an active power load. The two generators are connected via a low voltage power cable with $R_{TL} = 0.642 + j\,0.083$ ($\Omega$/km). Both generators are equipped with PF- and QV-droop controllers, allowing them to share the load proportionally according to their ratings. Figure 3.1 shows the active and reactive power sharing of the generators at a physical distance of 0.5 m, 250 m, and 500 m apart from one another, where the load is midway between the generators.

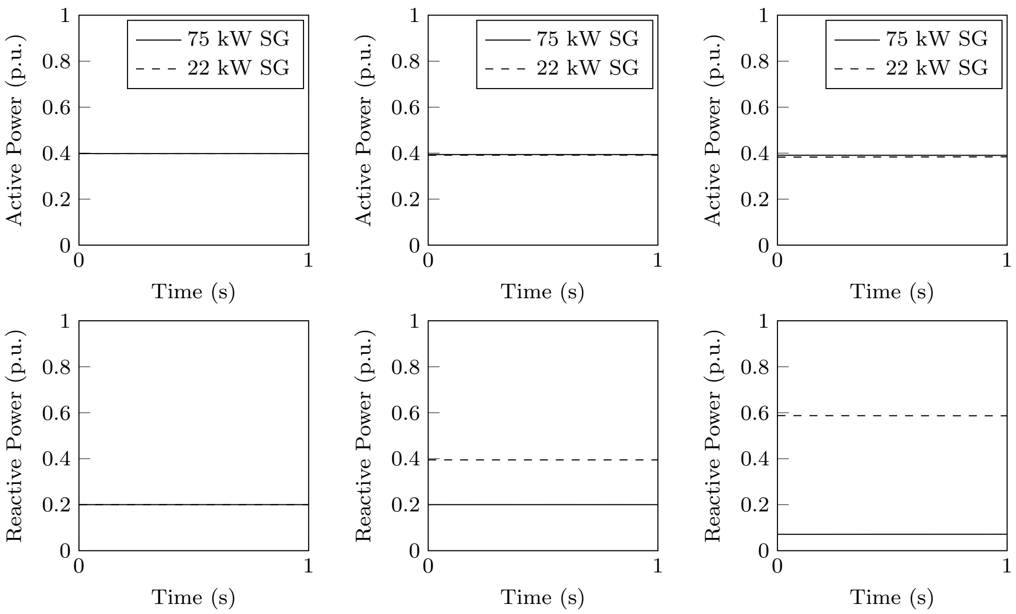


**a.** 0.5 m Apart. **b.** 250 m Apart. **c.** 500 m Apart.

**Figure 3.1** The effect of distance on the active and reactive power sharing between two generators.

Since there is no reactive load, the reactive power shown in Figure 3.1 is circulating between the generators. It is shown that with an increase in distance and hence line resistance, the circulating reactive power increases. In addition to the decrease in efficiency, the circulating reactive power causes an increase in reactive burden on the system [8]. When the DRs cannot sustain the reactive power demand, the voltage will collapse and compromise the reliability of the grid [8].

To reduce the error in reactive power sharing, variations of droop controllers have been proposed for inverters in PE-based microgrids, as discussed in the previous chapter. The performance of these controllers are rarely investigated for RMs, even though synchronous generators are expected to play a major role in microgrid installations. It is widely cited in the literature that conventional droop control is ineffective to achieve proportional load sharing in islanded microgrids. However, little investigation is done to identify the parameters that may influence in the cause.

There is a need to investigate the load sharing between generators in an islanded microgrid. The causes and effects need to be identified to allow a comprehensive solution to be developed.

## 3.2 Research Objectives

The aim of this research is twofold. Firstly, to set up a simulation environment and validate that it is able to represent the physical system. Secondly, to investigate the effects of resistive-dominant line impedance and the parameters that influence the load sharing in a LV microgrid. The main research objectives are:

- To review the state-of-the-art technology in islanded microgrid research and subsequent identification of the challenges faced by conventional droop controllers.
- To propose an islanded microgrid case study as the Example Microgrid for this research.
- To set up the Example Microgrid in the laboratory.
- To represent the experimental set-up of the Example Microgrid in simulation.
- To validate that the simulation model is able to represent the experimental set-up under defined conditions.
- To investigate the effects and the parameters that influence the load sharing in an islanded microgrid. Identify, if possible, the maximum allowable distance for two generators in an islanded microgrid before the classical droop controller becomes ineffective.
- As a possible application of this research, to demonstrate that the simulation of the Example Microgrid can be used to study primary control strategies.

The scope of this research is limited to primary control within a two-generator microgrid. The set-up may be adapted for microgrids with multiple generators with slight modifications. This research focuses on the steady-state performance of the controller while ensuring that the generators are operating within their ratings during both steady-state and transient conditions.

## 3.3 Research Methodology

Based on the research objectives defined, the methodology to achieve the objectives is proposed. Figure 3.2 illustrates the task definition of this research. An Example Microgrid is proposed based on the literature survey conducted and the research objectives defined. An experimental test bed of the Example Microgrid is set-up in the laboratory. The simulation set-up is subsequently derived, where the model parameters are estimated through experimental measurements. The experimental and simulation set-up of the Example Microgrid contain identical components. The

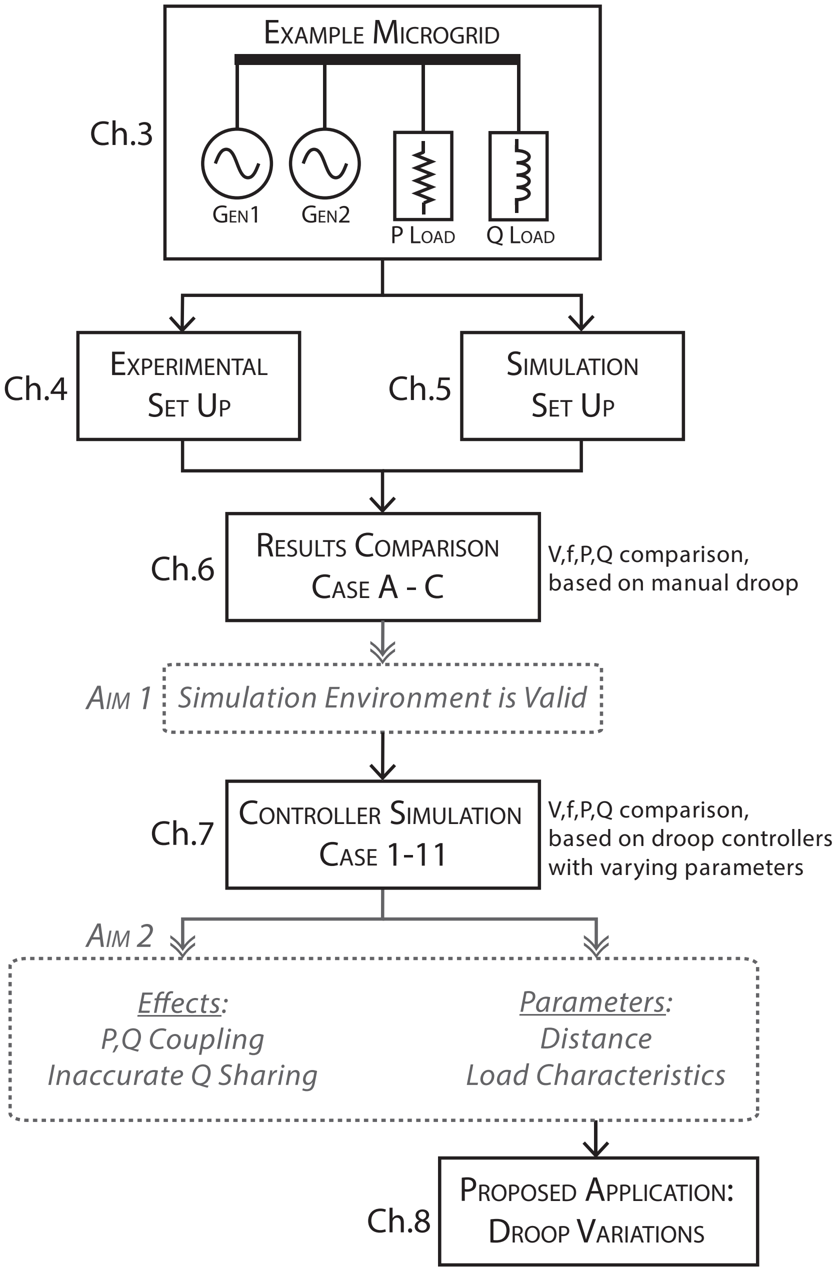


**Figure 3.2** Dissertation outline and the approach taken.

same control variables are applied to both the experimental and simulation set-up and the system response $(V, f, P, Q)$ are compared and contrasted.

This research focuses on the steady-state load sharing between weak sources, but transient experiments are conducted to allow the boundary condition of the simulation environment to be identified. Based on developed test Cases A - C, the simulation environment is confirmed to be accurate under steady-state operations and the conditions when the model is less accurate is presented with transient tests.

After validating the simulation environment, investigations that cannot be performed in the experiment are conducted in the simulation within the boundary conditions specified. Test Case 1 to Test Case 11 compare the system response with various control variables. The effects of resistive-dominant line impedance on the load sharing are demonstrated, including active and reactive power coupling and poor reactive power sharing. The parameters that cause the aforementioned effects are identified and discussed. As a future application to this research, three variations of droop controllers are tested in the simulation environment and the trade-off between each control strategy is discussed.

This research is heavily constrained by the components that are available in the laboratory. Compromises on many design choices are made due to the lack of appropriate physical components; however, the research objectives stated previously are not compromised.

## 3.4 Islanded Microgrid Example Case

Based on the common assumptions summarised in Section 2.2, an islanded microgrid case study is proposed for this research. The Example Microgrid described in this section is used throughout this study, where the envisaged application includes the development of a generator controller, as well as the study of the system dynamics.

### 3.4.1 Envisaged Application for this Research

While the world deems the access to electricity as a rudimentary necessity, the rural areas of Africa still suffer from poor energy security and reliability. These remote locations are beyond the reach of current transmission network, leaving its inhabitants without access to electrical energy [54]. An islanded microgrid that operates independently from the utility grid is proposed as a possible solution.

A typical islanded microgrid for rural electrification is depicted previously in Figure 1.1, Chapter 1, which includes multiple generators, loads and low voltage power lines. As rural microgrids are not provisioned to be connected to the utility grid, a combination of various generation technologies may exist to enhance the energy security. These technologies include renewable sources, storage devices and diesel generators. Often, there is no one dominant source in an islanded microgrid, but the different generation technologies all have relative sizes to one another.

Loads such as cooking and heating equipment, water pump, lighting, TV/radio, refrigerators and cell phone charger are commonly found in rural households [54]. This means that there is a combination of both active and reactive loads that may be unbalanced, nonlinear or both. In addition, the dwellings may be far apart from one another, resulting in a physically long distribution line over low voltage cabling.

This means that in a real life operating scenario, the microgrid may consist of both PE- and machine-based generators and suffer from unbalanced and nonlinear loads. In order to reduce costs, the generator redundancy is low, resulting in a tight reserve margin. With the load demand close to installed generation capacity, fast transients may occur frequently. Moreover, the physical distances between the generators and the loads are substantial, causing a significant drop of voltage through the low voltage line impedance. The dynamics of a microgrid with multiple generators and loads are complex and the analysis cannot be easily carried out without a sophisticated model.

### 3.4.2 Example Case Description

In order to focus the study on the load sharing between the sources, this dissertation strips a microgrid down to its bare minimum based on the assumptions identified in Chapter 2. As the first step in understanding the behaviours of islanded microgrids, the Example Microgrid is set-up to investigate the load sharing between the DRs to achieve a stable and reliable operation. With this application in mind, the following characteristics are essential:

1. A minimum of two fully controllable generators, where the output voltage and frequency can be regulated independently.
2. The lack of a swing bus in the grid, where the generators are classified as weak sources.
3. The generators and loads are connected through low voltage power lines.
4. There are both active and reactive load for the investigation of both the active and reactive power sharing.

Figure 3.3 depicts the Example Microgrid, where there are two fully controllable sources, two loads and a series resistance to represent the power cable line. A well-controlled microgrid is a scalable system, it is therefore possible to predict how a larger system would react based on its reduced scale equivalent. It is valuable to study a smaller and well-defined system prior to tackling a more complex scenario.

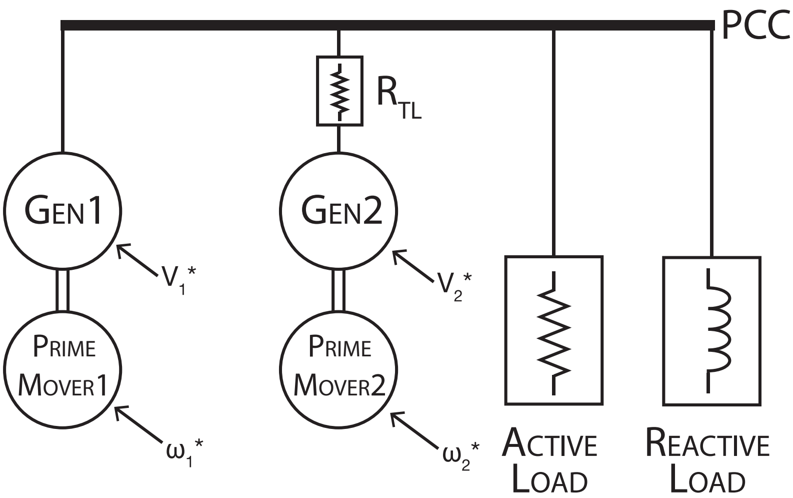


**Figure 3.3** Example Microgrid: an islanded microgrid test case.

### 3.5 Significance of Research

It is well documented in the literature that the resistive-dominant line impedance reduces the efficacy of droop controllers. Although different variations of droop controls are proposed to mitigate this effect, little research has been done to investigate the parameters that contribute to this effect. It is advantageous to investigate the load sharing under various operating conditions, hence understand the causes and effects and possibly predict what are the necessary conditions that may cause the droop controller to become ineffective.

It is detailed in Chapter 4 that the Example Microgrid set-up uses non-standard machines to emulate conventional synchronous generators. This exact set-up is not likely to be seen in real operating conditions, however, the power flow at the Point of Common Coupling (PCC) is the same as with using conventional synchronous generators. Therefore, the experimental results can be analysed as any islanded microgrid with two weak sources.

This research proposes a framework that can be used to investigate the load sharing between DRs in a LV islanded microgrid. Future researchers may build onto the existing test bed, simulation set-up and the knowledge gained from this work and perform further studies on similar subjects.

# CHAPTER 4

## Microgrid Example Case: Laboratory Experiment

This chapter discusses the experimental set-up of the Example Microgrid, where the microgrid components, including the prime movers, generators, loads, line impedances and auxiliary devices, are described in detail. The starting and operating of the experiment, its limitations, the instrumentation devices and data acquisition procedures are reviewed.

### 4.1 Experimental Set Up

The Example Microgrid is set up in the Genmin Laboratory of the University of Witwatersrand. Figure 4.1 shows the single-line diagram of the set-up, where there are two motors, two generators, one series resistance and two loads in an islanded mode.

The motors emulate the prime movers and import power from the campus grid, converting the electrical energy to the mechanical torque. The generators then convert the mechanical torque to electrical energy and export the power to the islanded microgrid loads. Therefore, the electrical power flow in the campus grid is independent of the electrical power flow in the Example Microgrid. The generator field current determines the generator output voltage, while the motor output torque determines the generator output frequency. The overview of the set-up is described below.

Two DFIGs are configured as synchronous generators by exciting the rotor windings with DC currents, allowing the terminal voltages to be varied independently with the two DC sources ($V_1^*, V_2^*$). This is similar to the field excitation of a synchronous generator, where $V_1^*, V_2^*$ are analogous to the set-points determined by the AVRs described earlier. The DFIGs are henceforth referred to as the SGs in the context of the Example Microgrid for this research.

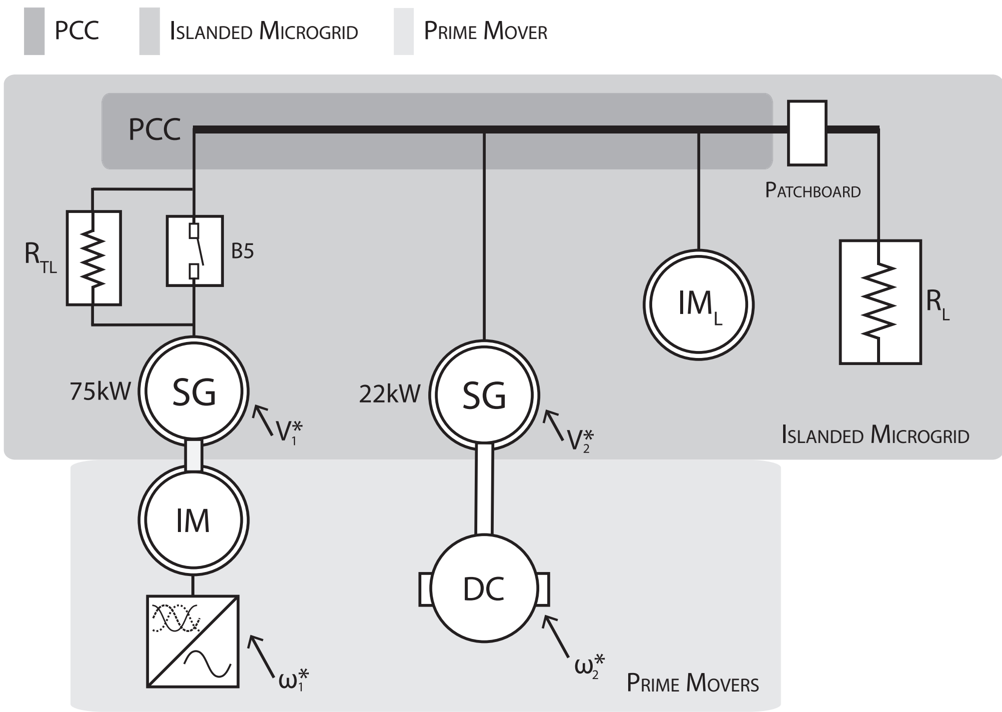


**Figure 4.1** Single line diagram for $R_{TL}$ case of the islanded Example Microgrid.

The smaller 22 kW SG is driven by a DC machine, where the shaft speed is controlled with the armature voltage of the DC machine (denoted as $\omega_2^*$ in Figure 4.1). The larger 75 kW SG is driven by an induction motor, where the shaft speed is controlled by a Variable Speed Drive (VSD) coupled to the induction motor (denoted as $\omega_1^*$). The control of the shaft speed with $\omega_1^*, \omega_2^*$ is analogous to the set-points determined by speed governors.

Similar to the Pf- and QV-droop, the output active and reactive power of the SGs are also controlled with speed and voltage. The output active power is controlled with the shaft speed of the prime movers, while the reactive power is controlled through the DC excitations of the SGs.

The resistive load is a reconfigurable, three-phase balanced wound resistor bank. It is physically further away from the rest of the microgrid components and is connected to the PCC via a patchboard. The inductive load is a 5 kW induction motor running at no load, drawing reactive power to magnetise its core.

The Example Microgrid operates with a voltage of 120 $V_L$ at 25 Hz for reasons discussed in Section 4.4. The machine and component ratings, a complete three-phase wiring diagram, operating conditions, list of instrumentations and photographs of the set-up can be seen in Appendix B.

## 4.2 Microgrid Components

This section describes the major components of the Example Microgrid in detail, including the SGs, prime movers, loads, power line impedances, the variac-and-rectifier set and the VSD. The operating conditions, three-phase wiring diagrams and parameter estimations are presented.

### 4.2.1 Separately-Excited Synchronous Generators

Two doubly-fed induction generators are configured as separately-excited synchronous generators in the Example Microgrid. Synchronous machines are the preferred generators in an electrical grid, since the voltage and frequency can be regulated directly through controlling the field excitation and shaft speed.

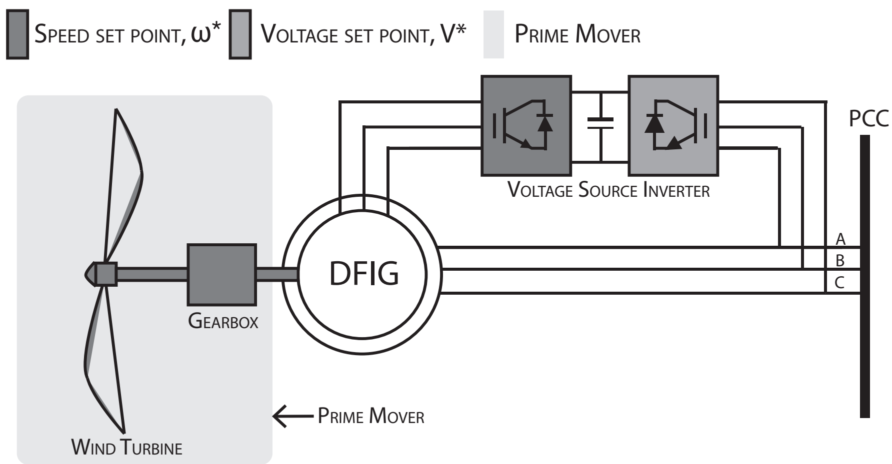


**Figure 4.2** The set-up of a DFIG in a wind turbine application, adapted From *Fletcher and Yang* [4].

A conventional application of a DFIG requires a back-to-back VSI to interface with the grid, as seen in Figure 4.2. The rotor of a DFIG is excited with an AC voltage through the slip rings and the stator feeds the three-phase power into the grid [36].

In the Example Microgrid, the rotors of the DFIGs are excited with a DC voltage, allowing the machines to operate at synchronous speed as ordinary synchronous generators, as seen in Figure 4.3. This allows the DFIGs to fundamentally behave as synchronous generators: having direct control of the terminal voltage through field excitation, as well as operating at zero slip (synchronous speed) regardless of torque.

There are physical differences between a synchronous generator and a DFIG; however, these differences do not influence the fundamental properties that are being investigated. For example, the 22 kW SG has a large airgap, resulting in the voltage waveform distorting at high excitations. However, since the Example Microgrid operates at 120 $V_L$, the voltage is not distorted at this excitation level.

The equivalent circuit parameters are estimated with four experimental tests: the stator and rotor resistances through the DC test, the leakage inductances and the magnetising inductance through the no-load and the locked-rotor test and the moment of inertia through the run-down test.

The synchronous generators discussed in this research are DFIGs in construction. However, since they are operating as synchronous generators, they are referred to as the synchronous generators for this dissertation when used within the context of the Example Microgrid. The estimated parameters are summarised in Table 5.1, while the testing procedure is detailed in Appendix C.

### 4.2.2 Prime Movers

Two motors are used to emulate the prime movers. The purpose of these two motors is to import power from the campus grid, thus providing mechanical power for the electricity generation. This research aims to investigate the power flow at the PCC, therefore, the motors emulate a generic prime mover without focusing on any specific type of generation. This substitution allows the power flow around the PCC to be analysed independent of the prime mover power available. When assuming sufficient generation power at all times as discussed in Chapter 2, this substitution does not affect the operation of the Example Microgrid.

The 75 kW SG is coupled with an induction motor powered by a VSD, as illustrated in Figure 4.3 (a). The drive uses an open-loop speed control for the induction motor. The VSD imports power from the campus grid, converting the electrical energy to mechanical energy through the induction motor. This allows the output active power of the SG to be controlled through the frequency set-point ($\omega_1^*$) of the VSD.

The 22 kW SG is coupled with a DC motor, where the armature and field windings of the DC motor are excited separately, as shown in Figure 4.3 (b). The armature voltage of a DC motor is directly proportional to its shaft speed and is varied manually via a variac. This allows the output active power of the SG to be controlled via the armature voltage of the DC motor.

Since the prime mover dynamics are not the main focus of this study, the induction motor and the DC motor are not parametrised. The ratings for the motors and the VSD are included in Table B.1, Appendix B.

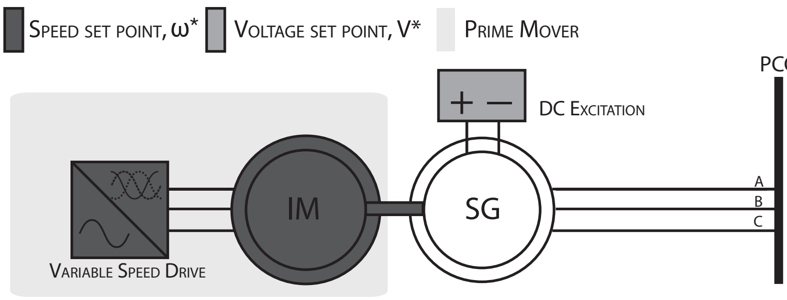


**a.** 75 kW SG experimental set-up.

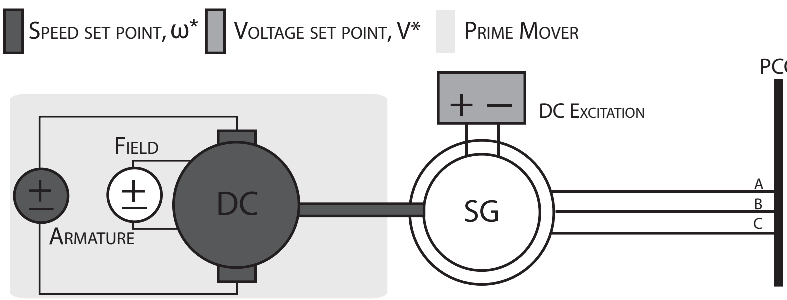


**b.** 22 kW SG experimental set-up.

**Figure 4.3** The experimental set-up of the SGs.

### 4.2.3 Loads

A resistive and an inductive load are used in the Example Microgrid to investigate both the active and reactive power sharing. The resistive load is a three-phase reconfigurable wound resistor bank located on the far north wall of the laboratory and it is connected to the microgrid PCC via a patchboard, as shown in Figure 4.4. It must also be noted that since the resistor bank is physically further away from the PCC, there exists a small series impedance between the resistor bank and the PCC.

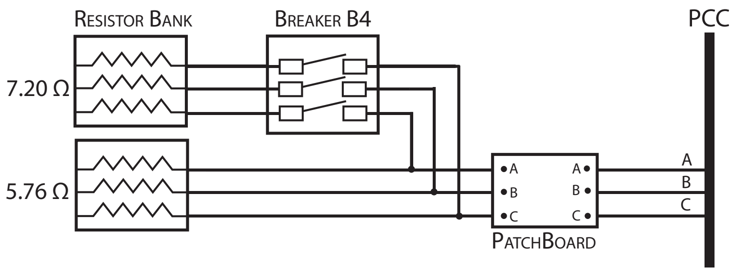


**Figure 4.4** Parallel resistance required to achieve a step load.

Each phase of the resistor bank consists of ten identical resistors, which can be connected in various combinations in series or parallel to achieve different resistances.

For experiments that focus on steady-state load sharing, the resistor bank is configured to 6.35 Ω (2.27 kW) for convenience.

For experiments that aim to demonstrate the transient behaviour of the Example Microgrid, the resistor bank is connected to a three-phase breaker (B4) to create a step load, as shown in Figure 4.4. The resistor is configured to ≈ 4.81 Ω (3.0 kW) when the breaker is opened. When the breaker is closed, the combined resistance is ≈ 3.07 Ω (4.7 kW).

A 400 V, 5 kW squirrel cage induction motor running at no-load is used as an inductive load. An induction motor operates at a poor power factor under no-load condition and draws a large reactive power to magnetise the core with little active power lost through the stator windings. At steady-state, the induction motor load draws 500 VAR at 120 $V_L$, 25 Hz.

### 4.2.4 Line Impedance

In the laboratory, the generators and loads are installed physically close to one another. The low voltage cables extend less than 20 m, which, according to Table 2.4, has an impedance of $12.9\angle 7.37^o\ m\Omega$. This does not create a substantial voltage drop between the two generators and therefore has a minimum effect on the load sharing.

In power network analysis, transmission lines are represented by equivalent $\pi$ circuits with lumped parameters, including the series impedance ($Z = R + j\omega L$) and shunt admittance ($y = G + j\omega C$) [8]. Transmission lines under 80 km are classified as short lines, which have a negligible shunt admittance [8, 55]. It is assumed that the power lines for islanded microgrids do not exceed 80 km; therefore, in this study, the power line is represented as a series impedance. Chapter 7 illustrates the effects of low voltage line impedance on an islanded microgrid, where a 1.5 km LV power line is observed to obtain a marginal stability with a 0.4 p.u. load under unity power factor. Therefore, a 1.5 km power line is chosen to ensure that the Example Microgrid is stable.

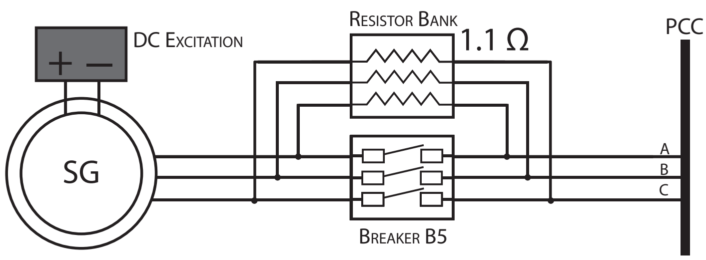


**Figure 4.5** 75 kW SG connected via a series 1.1 Ω resistance.

Since low voltage cables are resistance dominant, a balanced three-phase wound resistor bank is used to emulate the line impedance in the experimental set-up. A $R_{TL} = 1.1\,\Omega$ wound resistor bank is connected between the output of the generator and the PCC. The series resistor bank emulates a 1.55 km power line when the breaker B5 is opened and is shorted out when B5 is closed, as seen in Figure 4.5.

### 4.2.5 Auxiliary Devices

**Variac-and-Rectifier Set**

DC voltages are required for field excitation in order to control the output voltage amplitude; however, the variac-and-rectifier sets produce a pulsating DC voltage. Since the rotor inductance is not sufficient to filter out the harmonics, a 50 Hz component is introduced in the generated output voltage. A digital filter is therefore introduced with the cut-off frequency at 50 Hz to.

Two variac/rectifier sets are connected in parallel to excite the SGs since the current from a single variac is insufficient in reaching the terminal voltage of 120 $V_L$. One rotor terminal of the SG is connected to the positive DC terminal, while the other two are connected together to the negative DC terminal. The rotor of the 75 kW SG is Y-connected and the rotor of the 22 kW SG is Δ-connected as shown in Fig.4.6 (a) and Fig.4.6 (b) respectively.

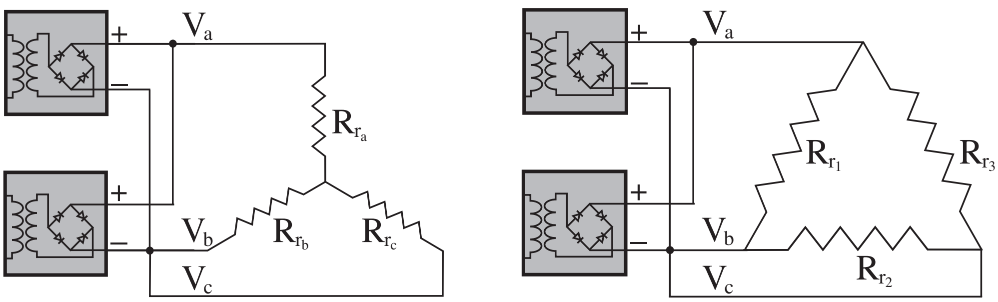


**a.** 75 kW Y-connected rotor. **b.** 22 kW Δ-connected rotor.

**Figure 4.6** SGs excited via a variac/rectifier.

A total of six variacs are used for the experiment: two 380 V, 50 A variacs are used to excite the 75 kW SG, two 380 V, 30 A variacs are used to excite the 22 kW SG and two 380 V, 30 A variacs are used to energise the armature and field windings of the DC motor.

A variac-and-recitifier set produces a pulsating DC voltage. This results in the output voltage of the synchronous generator to be

**Variable Speed Drive**

A 45 kW three-phase VSD is used to drive the induction motor at synchronous speed (25 Hz/750 rpm) with an open-loop control. This implies that loading the generator, hence the motor, reduces the speed. Therefore, due to the slip of the induction motor, its coupled SG operates at slightly, but negligibly less than the synchronous speed. Since the motor is only lightly loaded, the 75 kW SG is measured to operate at approximately 749.5 rpm.

## 4.3 Instrumentation Set-up

The experimental results presented in Chapter 6 are recorded with two Yokogawa power meters and a three-phase power meter for steady-state response and an oscilloscope for both the transient and the steady-state response. Additional instrumentation devices were used to record the input parameters to the Example Microgrid, i.e. the torque, speed, and field excitations of the SGs. The connection for each measurement device is shown in Figure 4.7 and the list of instrumentation is included in Table B.2, Appendix B.

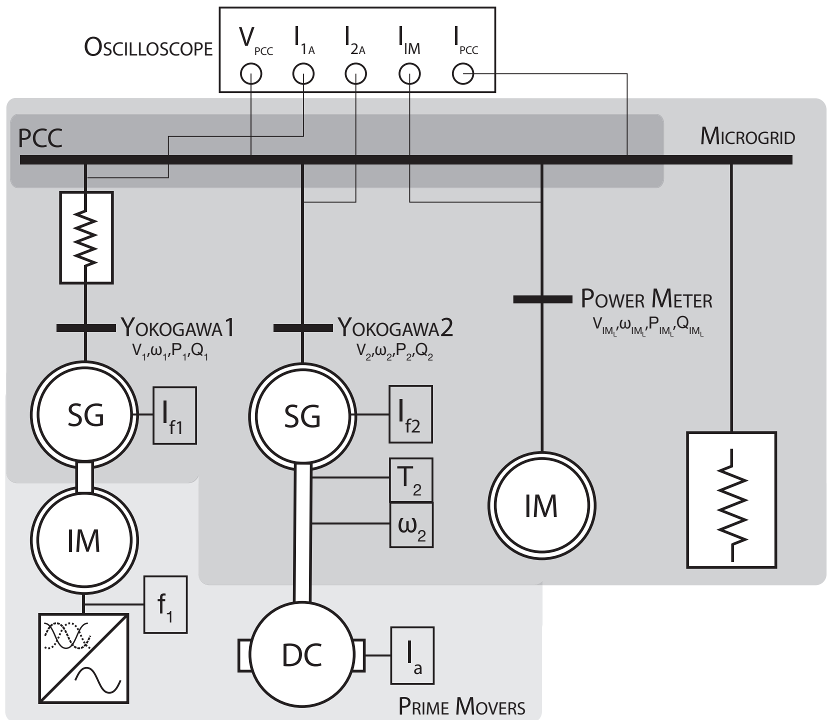


**Figure 4.7** Instrumentation set-up.

*Yokogawa Three-Phase Power Meter*

The resistor bank is accessed via a patch-board from the two SGs and the induction motor. The neutral is not accessible through the patch-board, therefore the Yokogawa meters are configured in a three-phase three-wire setting, instead of three-phase four-wire for Y-connected SGs.

The Yokogawa is designed to measure a fundamental frequency at 45 Hz - 65 Hz. The Example Microgrid operates at 25 Hz, which is below the recommended bandwidth of the Yokogawa. An oscilloscope is therefore used to verify the steady-state readings. The readings from the Yokogawa, which are verified by the oscilloscope, are recorded as the steady-state results.

#### *Four-Channel Rigol Oscilloscope*

A four-channel oscilloscope is used to measure Phase A voltage and current of the 22 kW SG, Phase A current of the 75 kW SG and the Phase A current of the induction motor load. For steady-state results, a digital filter at 50 Hz is applied to all signals. However, due to the limitation of the oscilloscope, the filter cannot be applied to a time frame longer than 20 ms. The detailed oscilloscope setting is discussed with each measurement result in Chapter 6.

#### *Three-Phase Power Meter*

A power meter is used to measure the steady-state active and reactive power of the induction motor load. The power meter calculates the three-phase power from the Phase A measurement since the motor is balanced.

#### *DC Current, Torque and Speed Measurement*

The excitation current from the two paralleled variacs are measured with a digital clamp meter for the 22KW SG. For the 75 kW SG, the sum of two analogue ammeters is recorded.

A torque transducer and a digital multimeter are used to measure the mechanical torque at the coupled shaft for the 22 kW SG. The conversion is 25 mV/N:

$$\frac{V_{measured}}{25} \frac{[mV]}{[mV]} = T_m \ [Nm] \tag{4.1}$$

A stroboscope is used to measure the 22 kW SG shaft-speed under steady-state conditions. Since the speed is identical everywhere in the microgrid, this value is recorded as the operating frequency of the Example Microgrid.

## 4.4 Running the Experiments

Two sets of experiments are conducted and reported in Chapter 6: the steady-state load sharing experiment and the transient step load experiment. The black starting of the Example Microgrid is identical for all the experiments. The operation are slightly different between the experiments. This section discusses the black starting and running of the experiments.

### 4.4.1 Black Starting

To synchronise a generator to an infinite bus, the incoming generator and the grid are required to have the same voltage amplitude, frequency, phase sequence and phase angle [5]. As specified in Table 5, IEEE1547-2003 [7], the voltage synchronisation difference must be less than 10% of the base voltage, frequency difference must be less than 0.3 Hz and phase angle less than $20^o$ difference.

Although the 75 kW SG is not an infinite bus and the grid formed by the two generators in the Example Microgrid is weak, it is still possible to employ the aforementioned method. This traditional method was used initially, where the circuit breaker connecting to two generators were closed when the two voltage waveforms of the generators are aligned. However, this caused a large starting transient that re-opens the circuit breaker. Therefore, an alternative synchronisation method is employed as follows.

At the start of the experiment, the two generators are connected in parallel with the resistor load bank. The line impedance and the induction motor load are disconnected from the grid to reduce the number of variables. Four steps are taken to connect the generators in parallel:

1. **Magnetising the rotor**: The 22 kW and 75 kW SGs are excited with 23 A and 35 A DC field current respectively, allowing the terminal voltages to be approximately 120 $V_L$ at rated speed. Magnetising both rotors allow the two SGs to be locked at synchronous speed once they are started.

2. **Synchronising the two SGs**: The 75 kW motor-generator set is started by ramping up the VSD to 25 Hz. This allows the 75 kW SG to operate as a generator, driving the 22 kW SG as a synchronous motor.

3. **Balancing the active power**: The 22 kW SG is switched from motoring to generating mode by increasing the input torque of the 22 kW SG. The 22 kW is left idling when the torque measurement ($T_2$) reaches 0 N·m. To increase $T_2$, the shaft speed set-point ($\omega_2^*$) is raised by increasing the armature voltage of the DC driving machine.

4. **Balancing the reactive power**: The field excitations are adjusted until the PCC voltage and the circulating reactive power reaches 120 $V_L$ and 0 VAR respectively. This is achieved by aligning the current waveforms $(I_1, I_2)$ with the PCC voltage. Since there is no reactive load, aligning the current waveforms with the PCC voltage ensures that both machines are operating at unity power factor.

Once the two SGs are synchronised, the series line resistance ($R_{TL}$) and the induction load is then switched in. The 75 kW SG supports both the active and reactive power load at this point. If necessary, the field excitation is readjusted to alleviate the circulating reactive power.

Black starting the Example Microgrid is a tedious process, where there are several variables that are dependent on one another: the magnitude and phase of the two generators' voltages, as well as their output currents.

### 4.4.2 Operating Conditions

The generator has a critical speed just below the synchronous speed (50 Hz) due to the long coupling shaft. In order to prevent mechanical vibrations, the generators run at half of their rated speed, i.e. 25 Hz.

The nameplate rated excitation currents cannot be provided to either of the generators due to the current limitations of the excitation variacs. In addition, to simplify the analysis, the grid voltage is chosen to be below the saturation point of the SGs obtained from their open-circuit terminal voltage curve. The generators are therefore operating at a reduced voltage of 120 $V_L$.

The Example Microgrid operates at 120 $V_L$, 25 Hz and the operating condition of the grid is summarised in Table 4.1. The maximum operating power is estimated by allowing for a minimum power factor of 0.8.

**Table 4.1** Operating conditions of the Example Microgrid.

| | **SG 1** | **SG 2** | $\mathbf{R_L}$ | $\mathbf{IM_L}$ | $\mathbf{R_{TL}}$ |
|---|---|---|---|---|---|
| Nameplate Rating | 75 kW | 22 kW | 6.75 Ω | 5.50 kW | 1.20 Ω |
| Operating $S_{max}$ (kVA) | 18.75 | 5.50 | 2.18 | 0.54 | - |
| Operating $P_{max}$ (kW) | $0.8\,(S_{max})$ | $0.8\,(S_{max})$ | 2.18 | 0.20 | - |
| Operating $Q_{max}$ (kVAR) | $0.2\,(S_{max})$ | $0.2\,(S_{max})$ | 0.00 | 0.50 | - |

Appendix C determines the operating voltage by investigating the relationship between (a) terminal voltage and core saturation (b) reactive power, magnetising inductance and saturation. In addition, Appendix D provides the reasoning for operating the Example Microgrid at 120 $V_L$ by analysing the results obtained for operating the grid at 180 $V_L$.

### 4.4.3 Steady-State Load Sharing Configuration

The conventional PF-droop controller allows the two generators to share the active power load proportionally, according to the droop equation (Eq.(2.3)). The controller adjusts the frequency set-point according to the active power load measured at the local bus. Similarly, the reactive power load is shared proportionally as prescribed by Eq.(2.6), where the controller adjusts the voltage set-point according to the reactive power load measured.

The manual adjustment of the set-point according to the droop equations is difficult. Even though droop controllers typically have a relatively low bandwidth (under 1 kHz [29]) compared to other control strategies, it is still too fast for the response time of an operator to adjust the set-points of two SGs. An alternative method is therefore employed to examine the PF- and QV-relationship.

The active load sharing between the generators is controlled by adjusting the speed hence the torque of the 22 kW SG. The DC motor armature current (DC $I_a$ in Figure 4.7) is increased to allow the 22 kW SG to pick up more load, and vice versa. However, with the increasing output current, the terminal voltage of the generator drops due to the lack of a voltage regulator. Therefore, the 22 kW SG field current ($I_{f2}$) is increased to maintain a constant PCC voltage. The independent and dependent variables are summarised in Table 4.2.

**Table 4.2** Summary of variables used in the Load Sharing Tests.

| Variables | **PF-Droop** | **QV-Droop** |
|---|---|---|
| Independent | DC $I_a$ | $I_{f1}$, $I_{f2}$ |
| Dependent | P, Q | P, Q |
| Constants | $V_{pcc}$ | f |

The reactive power load sharing between the generators is controlled by adjusting the voltage of both SGs. To increase the 22 kW SG share of reactive load, its field current ($I_{f2}$) is increased while the field current of 75 kW SG ($I_{f1}$) is decreased. However, the generator slows down with the increase of output current. Therefore, in order to keep the frequency of the grid constant, the torque is adjusted until it is identical to the value prior to the adjustment of the field currents. This is more evident in the 22 kW SG, as it is smaller and the change in load has a larger influence on its output current.

In summary, the conventional droop controllers allow the generators to share the load autonomously through drooping the generators' frequency and voltage to a lower value. Therefore, without a secondary controller to restore the deviations, the microgrid operates at below the rated frequency and voltage depending on the load demand.

In the load sharing experiment conducted, the load sharing between the generators is also adjusted through the frequency and the voltage of both generators. However, the frequency and voltage does not deviate from the rated values since it is always adjusted back manually.

## 4.5 Summary

An Example Microgrid is proposed for this research to allow the study of steady-state load sharing for weak sources in islanded microgrids. A three-phase, three-wire balanced AC system is set-up with two separately-excited SGs, a resistive load and an inductive load in the laboratory.

The rotors are excited with DC currents, allowing them to exhibit the fundamental behaviour of a separately-excited synchronous generator. The terminal voltage of the SG is controlled through the DC excitation, while the speed is controlled with the prime mover output torque.

Instead of running the Example Microgrid at the standard 400 V, 50 Hz, it is operating at 120 V, 25 Hz. Although the generators' ratings are quartered by halving the operating voltage, the characteristics (such as the drooping of speed due to loading) of the generator are not compromised.

The low voltage, resistive-dominant 1.55 km power line is represented with a 1.1 $\Omega$ resistor bank connected in series with the generators. Although compromises are made by substituting SGs with DFIGs and power cables with resistor banks, the aspects that are pertinent to the study of load sharing are pertained.

The primary aim of this research is to set up a simulation environment that accurately represents the physical system in the laboratory. This chapter discusses the experimental set-up of the Example Microgrid, and the next chapter presents simulation set-up based on this chapter.

# CHAPTER 5

## Microgrid Example Case: Modelling and Simulation

This chapter presents the simulation model of the laboratory set-up of the Example Microgrid described in Chapter 4. The components that are directly connected to the PCC are modelled in detail, including the SGs, the loads and the line impedance. The other components are reduced to their simplest form without compromising the pertinent aspects of the system. The SG models are validated by loading the machines and comparing the experimental and simulation results.

### 5.1 Simulation Set-Up

A simulation model is devised to represent the experimental set-up, allowing for the behaviours of the physical system to be observed and predicted. By performing tests on a realistic model, the response of a real system can be inferred. The simulation model developed in this chapter is based on the experimental set-up described in Chapter 4. The model presented here is used as the base model for Chapter 7 and Chapter 8.

The simulation of the Example Microgrid is performed using MATLAB® R2013b with Simulink®. Simulink, an extension of MATLAB, is an application-specific program that is used for simulating systems in both dynamic- and steady-state in a block diagram environment [56]. This research makes use of the *SimPowerSystems*™ Toolbox for simulating electric power systems [57], as well as *Simscape*™ [58] and basic Simulink [59] for the control systems.

A Simulink model is developed for the Example Microgrid presented in Appendix B.1. Figure 5.1 is the overview of the Simulink model, which can be compared to the experimental set-up shown in Figure 4.1.

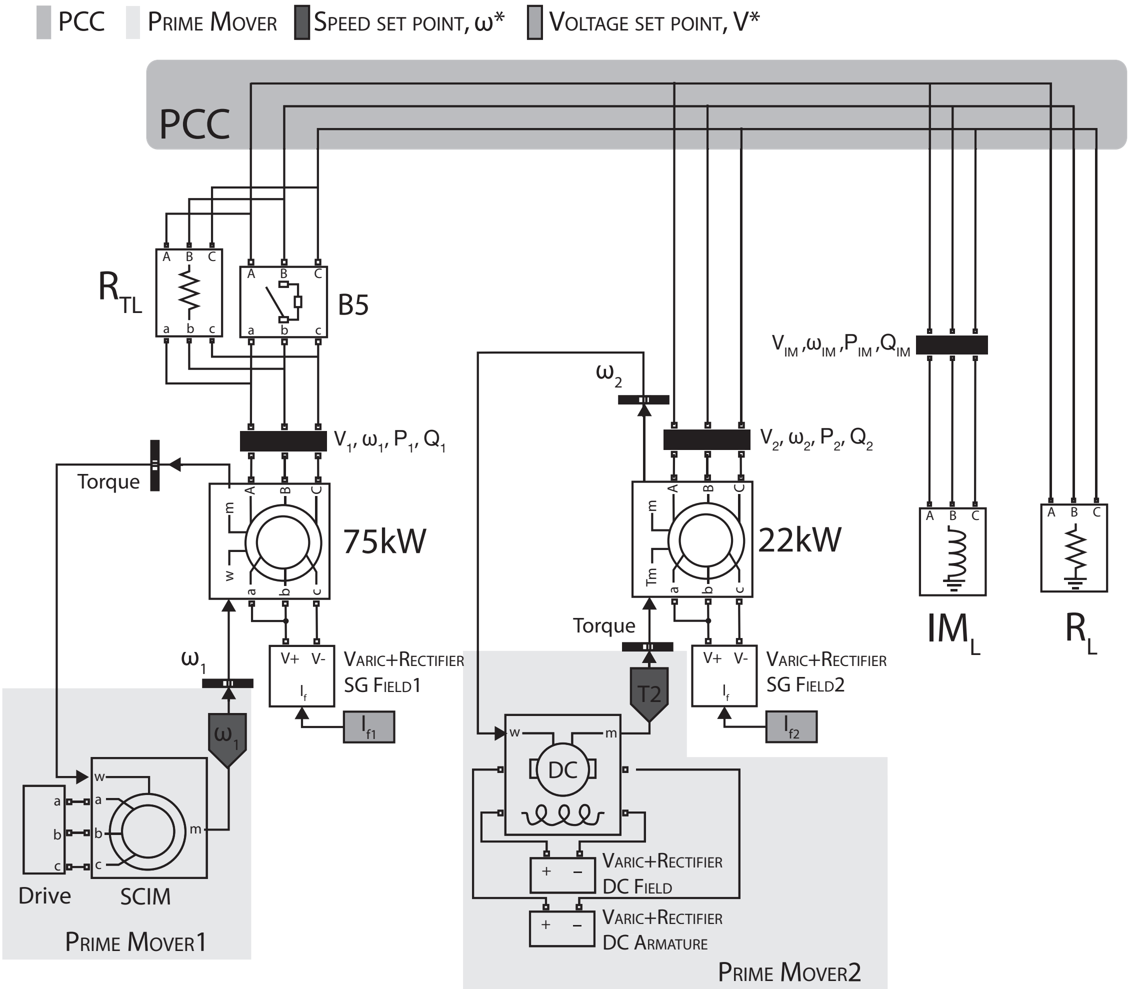


**Figure 5.1** Simulink model of the Example Microgrid.

This study focuses on the load sharing of the microgrid at the PCC during steady-state. Therefore, only the components that are directly connected to the PCC are modelled in detail. This includes the two SGs, the resistive and inductive load ($R_L, IM_L$), as well as the line impedance ($R_{TL}$). All the other components that are not directly connected to the PCC are reduced to their simplest representable forms and are not examined. The prime movers, VSD and the variac/rectifier sets are therefore replaced with a speed, torque, or field current set-point in the model.

The operating conditions of the Simulink model are identical to the experimental Example Microgrid, with a voltage of 120 $V_L$ at 25 Hz. A complete simulation environment, including the chosen solver, initial conditions, variables, tolerance and integration methods, etc is included in Appendix B.

## 5.2 Component Modelling

The developed model is required to be as simple as possible while still being able to realistically represent the physical system [60]. A couple of factors are taken into account when deciding on the modelling complexity for each component: time constants, the degree of influence to the overall model and the detail of study.

### 5.2.1 Synchronous Generators

The Simulink machine blocks are comprehensive, widely adopted in control systems, machine and power system studies. Therefore, the standard Simulink machine block is used in this study instead of modelling the machine from first principles. This allows for the study to be focused on the interactions between the generators rather than the machine itself.

The only disadvantage is that this research uses DFIGs as SGs, therefore modelling and simulation of the machine requires additional customisation. For example, the rotor of the SG is excited with DC currents; however, the stator voltage saturation is specified as a function of the stator current only. The effects of rotor current on the saturation cannot be included in the standard Simulink block, therefore two different models are investigated to model the SGs.

Firstly, a *synchronous machine* model is used. The equivalent circuit of the DFIG is often reduced to a synchronous machine by omitting the magnetising inductance and the rotor impedance to simplify the analysis [61]. Since the DFIGs operate as synchronous generators in this research, this model is looked at initially. Secondly, an *asynchronous machine* model is investigated because a DFIG is essentially an induction machine with a wound rotor.

Appendix C compares the *synchronous machine* and the *asynchronous machine* Simulink blocks by comparing their simulation results to the experimental measurements. The terminal voltage vs. core saturation, as well as the relationship between reactive power, magnetising inductance and saturation are investigated. It is realised that the simplification to a synchronous machine introduces significant errors in the model when the flux densities are high. This effect is also found by *McMahon et al.* [61].

It is concluded in Appendix C that the use of *asynchronous machine* and *synchronous machine* blocks create a trade-off, where the former includes the magnetising inductance in the model and the latter allows the specification on the stator voltage saturation based on the field current excitation.

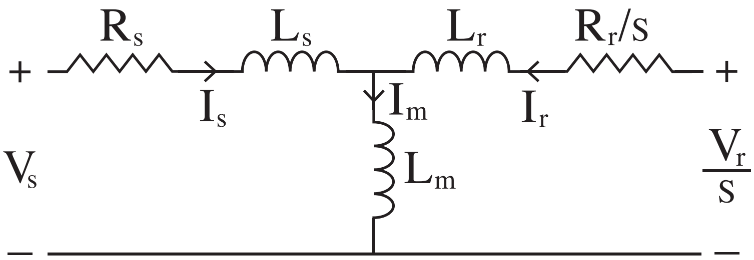


**Figure 5.2** Equivalent circuit for a DFIG, adapted from *Sen* [5].

By operating the generators with the stator voltage below the saturation point, the modelling of saturation is not required, therefore the *asynchronous machine* block is chosen to represent the SG. The operating voltage is chosen to be 120 $V_L$ to prevent core saturation from compromising the validity of the model as described in Section 4.4.2.

The *asynchronous machine* Simulink block adopts the fourth order state space model and a second order system is used to describe the mechanical aspects of the machine. The model is capable of simulating both steady-state and dynamic responses of the SGs [56]. Although the stator and rotor quantities are in the dq-frame [57], the parameters required are extracted from the steady-state electrical equivalent circuit.

For a balanced three-phase system, the electrical per phase equivalent circuit of an asynchronous generator is shown in Figure 5.2, where the following notations are used:

| | | | |
|---|---|---|---|
| $V_s$ : | Stator Voltage | $I_s$ | Stator Current |
| $V_r$ : | Rotor Voltage | $I_r$ | Rotor Current |
| $s$ : | slip | $I_m$ : | Magnetising Current |

The equivalent circuit parameters of both 22 kW and 75 kW SGs are approximated through stator and rotor resistance estimation, leakage inductance estimation and magnetising inductance estimation. The retardation test is used to determine the moment of inertia. The estimated parameters are summarised in Table 5.1, where the testing procedures are included in Appendix C.

**Table 5.1** Estimated parameters of the SGs.

| Parameters | | **22 kW SG** | **75 kW SG** |
|---|---|---|---|
| $R_s(m\Omega)$ : | Stator Resistance | 215 | 31 |
| $L_s(mH)$ : | Stator Leakage Inductance | 1.4 | 0.636 |
| $R_r(m\Omega)$ : | Rotor Resistance | 300 | 80 |
| $L_r(mH)$ : | Rotor Leakage Inductance | 1.4 | 0.636 |
| $L_m(mH)$ : | Magnetising Inductance | 39.2 | 101.3 |
| | Moment of Inertia | 0.252 | 1.19 |

This section provides the background in adopting the SG model through investigating the trade-offs between the synchronous and asynchronous machine blocks. The SG model validation is assessed in Section 5.3 through experimental testing.

### 5.2.2 Load

It is suggested by *Glover et al.* [55] that in the studying of a power system where the time frame being investigated is over 10 s after the disturbance, the static load model should be used. As the steady-state load sharing is the primary focus of this study, both the resistive and inductive loads adopt a static load model. The static load model is sufficient when the change in voltage and frequency is fast and the steady-state is reached quickly [8].

The resistor bank is insensitive to the variation of voltage and frequency, therefore the effective active and reactive power can be represented with a simple algebraic equation. Therefore, the three-phase resistor bank is modelled as a constant resistive load in this study.

The inductive load, which is an induction motor, is connected under no load conditions to investigate the reactive power sharing between the two generators. An accurate model of the inductive load is essential in performing stability studies [8], however, assuming that the AVR is able to control the voltage back to 120 $V_L$ and the inductive load does not change during the experiment, it has no effect on the system stability. Therefore, it is sufficient to model the induction motor as a constant inductive load under steady-state conditions.

The inductive load is still voltage dependent at steady-state, which has a magnetising current proportional to the PCC voltage. This means that to ensure the validity of the simulation, the magnetising inductance must be measured for each operating condition. Two methods were compared in Simulink: modelling the induction motor as an inductor, and modelling the induction motor as an reactive power load.

The magnetising inductance is measured with the procedure described in Appendix C.1.1. The reactive power drawn is measured with a power meter at run-time. To compare the two modelling method, the experiment and simulation detailed in Chapter 6 were performed, where the only variable between between the simulations was the induction motor model. The outputs of the simulations were identical, therefore it is concluded that both models are interchangeable within the simulation.

Although it is possible to measure the magnetising inductance as described in Appendix C.1.1, it is a laborious and time-consuming process. Since the reactive power drawn by the motor can be easily measured with a power meter at run-time, the induction motor is modelled as a reactive power load. Therefore, the reactive power drawn by the motor is recorded during the experiment and used as an auxiliary input to the simulation.

### 5.2.3 Line Impedance

Due to the limitation of the physical space in the laboratory, the power line is replaced with a three-phase wound resistor bank connected in series with the SG. A three-phase resistor is used to represent the resistor bank, where the inductance and capacitance of the wound resistor bank are minimal and therefore ignored. The validity of reducing a transmission line model to a series impedance is discussed in Section 4.2.4.

The resistive load for the Example Microgrid is physically further from the PCC and is connected to the rest of the microgrid components via a patchboard. It is assumed that this separation is not far enough to create a substantial voltage drop, therefore the contactors of the patchboard as well as the cables are not included in the Simulink model.

### 5.2.4 Simplified Components

The DC motor, inductive load, VSD and the variac/rectifier sets are not modelled in detail. By measuring the output of these components (such as torque, speed, and current) and using it as the input variable to the model, these components can be treated as a black box. This section discuss the trade-off of simplifying the aforementioned components.

#### *Prime Movers*

The Example Microgrid set-up in the laboratory uses a DC motor and an induction motor with a VSD to emulate generic prime movers. This research aims to investigate the power flow around the PCC instead of the machine dynamics. Since these motors are only there to provide mechanical power to the SGs and are not directly connected to the PCC, they can be modelled as a constant source of mechanical power.

The motors are therefore replaced by a set-point value. The induction motor and VSD for the 75 kW SG has a speed set-points and the DC motor for the 22 kW SG has a torque set-point. This set-up is identical to the steady-state experimental configuration discussed in Section 4.4.3. The speed of the 75 kW SG is controlled by the VSD and the torque of the 22 kW SG by the DC armature current $I_a$. Therefore, $\omega_1$ and $T_2$ in Figure 5.1 are replaced by the constant values measured from each experimental test case.

This simplification decouples the motor dynamics from the transient response of the system. For example, the speed set-point is given to the motor instead of the SG itself, so there is a time delay based on the motor dynamic characteristics. This means that the transient response of the simulation system may be inaccurate. However, this level of detail concerns mainly the transient response of the system and has little effect on the steady-state load sharing response, this simplification is thus deemed viable for this study.

The DC motor, the induction motor and the VSD can be modelled with Simulink using a back-to-back configuration shown in Figure 5.1. This may be a necessary improvement to the simulation model for transient studies.

*Variac/Rectifier Set*

The variac-and-recitifier sets are represented as ideal DC voltage sources. The DC voltage is the product of the measured field current and the measured DC resistance of the SG rotor, as described in Equation 5.1. Since the 75 kW SG is star-connected, the Thevenin resistance is 1.5 times the rotor resistance.

$$\begin{aligned} 75\,\text{kW}:& V_{DC1} = I_{f1} \times 1.5 R_{r1} \\ 22\,\text{kW}:& V_{DC2} = I_{f2} \times 1 R_{r2} \end{aligned} \tag{5.1}$$

DC voltages are required for field excitation, which controls the voltage amplitude of the SGs. However, the variac-and-rectifier sets produce a pulsating DC voltage. This pulsating DC voltage may compromise the integrity of the output if the rotor inductance is insufficient to smoothen the waveform.

This is observed in the experimental result, where a 50 Hz component is introduced in the output voltage. A digital filter is applied with the oscilloscope (see Section 4.3) to allow for a smooth voltage waveform to be recorded. Since the simulation is compared with the recorded experimental result, it is possible to model the variac-and-rectifier sets as ideal DC sources.

### 5.2.5 Measurement System

The simulation environment allows all parameters that are difficult to access or inaccessible in the physical system to be monitored. In addition, the measurement does not suffer from aliasing, time delay or inaccuracies. This must be noted when designing the control system, in order to prevent the controllers from accessing signals that cannot be obtained, such as the PCC voltage.

## 5.3 Model Validation

According to *Ong* [60], in assessing the simulation results, it is necessary to ensure that the model reflects the actual system for the conditions simulated. Before one can use the components in a larger system, it is important to identify the boundary conditions where the model is valid.

The SGs are the components with the highest degree of complexity and have the most impact on the system response in the experiments conducted in Chapter 6. This section aims to validate that the SG model described previously is able to represent the physical SGs and that the parameters estimated are accurate.

The SGs are loaded individually with various resistors under various field excitations. The simulated voltages and currents are corroborated with the experimental measurements. The experimental set-up for the SGs are shown in Figure 4.3, where the PCC is connected to the patchboard and then the resistor bank, as illustrated in Figure 4.4.

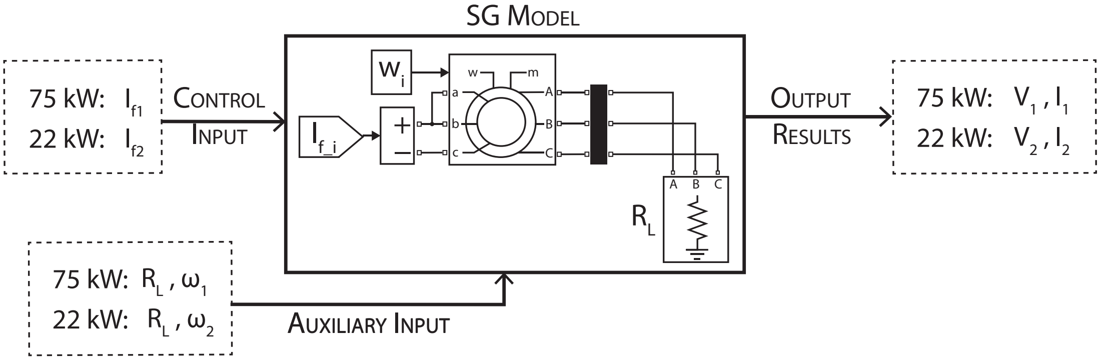


**Figure 5.3** The simulation set-up for model validation.

The simulation set-up for the SG model validation is depicted in Figure 5.3, where the prime movers are replaced by a speed set-point ($\omega_i, i = 1, 2$) as discussed previously. The response of the SG at various excitation levels are investigated. The system control inputs are the field currents ($I_{fi}$) and outputs are the stator voltages and currents ($V_i, I_i$). The load resistance and speed are the parameters of the system that are used as the auxiliary input to the simulation set-up and allow for a controlled simulation environment.

### 5.3.1 75 kW SG Load Test

Three different resistive loads are used for the 75 kW SG to produce various output currents at ≈ 110 $V_L$. The three-phase wound resistor bank is configured to 6.8 Ω, 3.7 Ω and 2.2 Ω. For the 6.8 Ω resistive load, three different field currents are used to achieve three different EMFs. The steady-state stator voltage and current are recorded according to the field current, as seen in Figure 5.4. The constant resistance case and the constant voltage case are investigated in this section.

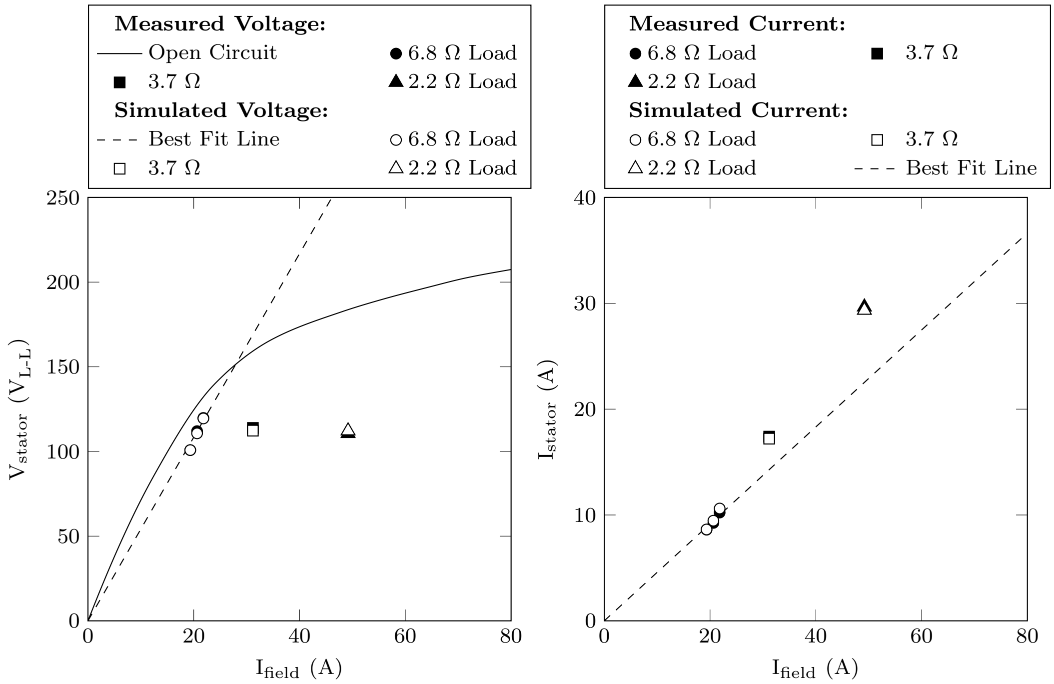


**a.** Stator Voltage vs. Field Current. **b.** Stator Current vs. Field Current.

**Figure 5.4** 75 kW Load Test.

*Constant Resistance at 6.8 Ω*

Figure C.3 (a) shows a linear relationship between the terminal voltage and the field excitation under constant resistance load (see the dashed best fit line). This is because at low excitation, the voltage is not affected by the magnetic saturation. It can also be seen that due to the loading, the measured voltages are below the open-circuit curve as expected. Figure C.3, Appendix C shows that the linearity is not preserved at higher operating voltages under loaded conditions. Figure 5.4 (a) shows a linear relationship between the terminal voltage and the field excitation under constant resistance load (see the dashed best fit line). This is because at low excitation, the voltage is not affected by the magnetic saturation. It can also be seen that due to the loading, the measured voltages are below the open-circuit curve as expected. Figure C.3, Appendix C shows that the linearity is not preserved at higher operating voltages under loaded conditions.

As mentioned earlier in Section 5.2.1, the model is able to accurately reflect the physical SG when the excitation is low. This is observed in Figure 5.4 (a), where the simulated results correlate very closely to the experimental measurements, with an average error of 0.6% between the five data points.

Since the SG is operating at a voltage that it is parametrised at 120 $V_L$, the model is able to represent the physical SG most accurately. For additional data points, Figure C.4, Appendix C shows that the simulated voltage undercuts the measured voltage below the parametrised voltage, and overestimates the ones above.

Figure 5.4 (b) also shows a linear relationship between the stator current and the field excitation. This is expected since the stator current is proportional to the stator voltage with the load $R = 6.8\ \Omega$. The simulated results are also very close to the measurements, where the average error for $I_{stator}$ is only 1.67%.

*Constant Voltage at* 110 $V_L$

To investigate the SG performance under constant voltage, the middle circle, the square and the triangle in Figure 5.4 (a) is compared. It is clear that the voltage remains constant at approximately 110 $V_L$ with the change in field current. Due to the loading effect, the voltage deviates further from the open-circuit measurement as the resistance decreases, i.e. load power increases.

By keeping the voltage constant as the load resistance decreases, the stator current increases with the field current. It can be seen from Figure 5.4 (b) that the gradient is steeper with an increasing load, indicating a higher output power from the SG.

### 5.3.2 22 kW SG Load Test

Three different field currents are used to excite the 22 kW SG to achieve different output voltages under a constant resistive load (6.8 Ω). The experimental and simulated steady-state voltages and currents are compared in Figure 5.5.

Like the 75 kW SG, the stator voltage also exhibit a linear relationship with the field current. The measured voltage is also below the open-circuit measurement due to the loading. The simulation results for the 22 kW machine closely resemble the measured results, with the average voltage error at 2.0% and the average current error at 2.3%.

## 5.4 Simulation Configuration

The steady-state results of the experiments are recorded and analysed. However, the simulation does not start in steady-state, instead the SGs are accelerated from standstill. Since only the steady-state result is of interest, the simulation results

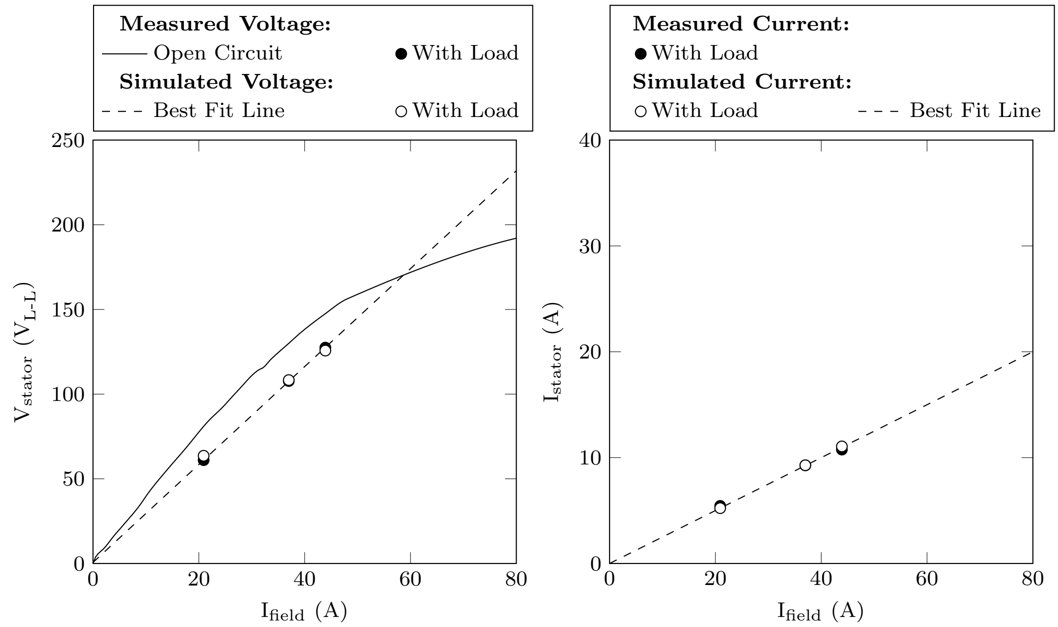


**a.** Stator Voltage vs. Field Current. **b.** Stator Current vs. Field Current.

**Figure 5.5** 22 kW Load Test.

are recorded once the system reaches steady-state, where the voltage and frequency oscillations have dampened to within 5% of their steady-state values.

## 5.5 Conclusion

The simulation system developed in Simulink represents the Example Microgrid set-up in the Genmin laboratory. This research aims to investigate the power flow between the sources at the PCC, therefore only the components directly connected to the PCC are modelled.

The SGs are modelled using the standard *asynchronous machine* block provided by Simulink, where the parameters of the physical machines are estimated through laboratory testing. The static load models are used, where the wound resistor bank and the induction motor are represented with constant impedance and constant reactive power load respectively. A constant impedance is also used to model the resistor bank that is used to emulate the line impedance.

The Simulink model is simplified by replacing the prime movers with a speed or torque set-point and the variac-rectifier set with the field current set-point. To validate the model and parameter estimation of the SGs, experimental tests are conducted. The SGs are loaded with various resistive loads under various excitations.

The steady-state results show that this simplification does not compromise the validity of the model as the errors are below 3%. Therefore, it can be concluded that the SGs models with the parameters estimated are able to accurately represent the physical machine as long as the machines do not saturate.

This chapter models and validates the SG models through component-wise testing. The results show that the models of the SGs are effective in isolation at 120 $V_L$, 25 Hz, and may be used in a larger system. The next chapter evaluates the Example Microgrid model as a whole with system-wise testing, where the interaction between the two SGs is investigated.

# CHAPTER 6

## Comparison of Experimental and Simulation Results

This chapter validates and concludes that the Example Microgrid modelled in Simulink is able to represent the physical Example Microgrid. Various experiments were performed on the Example Microgrid in the laboratory to demonstrate the effects of resistive line impedances on weak sources. As a proof-of-concept, both steady-state and transient experiments are conducted. Through corroborating the simulation and experimental results, the Simulink model developed can be used in confidence for further investigations and studies.

### 6.1 Overview

Chapter 5 warranted that the SG model can be used in isolation through component-wise testing. This chapter aims to validate the simulated model of the Example Microgrid as a whole through system-wise testing. The performance of the model is evaluated through corroborating the simulation and experimental results. The results are analysed both quantitatively and qualitatively for the steady-state study. The transient study is included to establish the limitations of the model, therefore the transient results are analysed qualitatively.

Table 6.1 summarises the test cases performed on the Example Microgrid. For the steady-state experiment, the load sharing tests without the line impedance (Case A) are carried out to validate that the model can be used in a larger system under steady-state. The load sharing tests with line impedance (Case B) are then conducted, demonstrating that the resistive line impedance affects the Pf- and QV-droop control. Transient experiments are conducted by introducing two different disturbances to the Example Microgrid. This allows the system response of the Example Microgrid Simulink model to be compared with the experimental Example Microgrid, validating the model under transient conditions.

**Table 6.1** Experimental and simulation test cases for the Example Microgrid.

| Steady State | | | | Transient | | |
|---|---|---|---|---|---|---|
| **(Case A)** without $R_{TL}$ | | **(Case B)** with $R_{TL}$ | | **(Case A)** without $R_{TL}$ | **(Case B)** with $R_{TL}$ | **(Case C)** Disturbance |
| **(A.1)** Pf | **(A.2)** QV | **(B.1)** Pf | **(B.2)** QV | **(A.3)** 5 kW | **(B.3)** 5 kW | Switched $R_{TL}$ |

There are seven sub-tests, each assigned with a test case number. Test Cases A are steady-state and transient tests without line impedances, whereas Test Cases B are with line impedances. Sub-cases A.1/B.1 investigate the Pf-relationship, sub-cases A.2/B.2 analyse the QV-relationship and sub-cases A.3/B.3 examine the step response of the system. In Case C, the line impedance is switched in and out to introduce a disturbance to the system.

The tests in this chapter are performed to achieve three objectives. Firstly, to validate that the simulation environment reflects the physical system accurately. Secondly, to demonstrate that the droop relationship is evident in the Example Microgrid set-up in the laboratory. Finally, to show how the resistive line impedance affects droop control in achieving a proportional load sharing. Based on the objectives, the following relationships are examined closely in the sections below:

- Comparison between the simulation and experimental results.
- The Pf- and the QV-droop control.
- The Q vs. f relationship under Pf-droop and the P vs. V relationship under QV-droop.
- Comparison between the droop response with and without line impedance for both the Pf- and QV-droop control.
- Comparison between the transient step response with and without the line impedance.
- An overall comparison between the steady-state and transient response.

## 6.2 Steady-State Load Sharing Results and Analysis

The steady-state tests are used to validate that the individual components modelled are able to be used in a larger system without compromising their characteristics. The droop response with and without low voltage line impedance is the main focus of this set of experiments. Both qualitative and quantitative analyses are used in comparing the results, where the trend of the results as well as the numerical values are assessed.

The load sharing test without line impedance (Case A) shows that the output active and reactive power of a generator can be controlled through adjusting the frequency and voltage set-point respectively. This experiment demonstrates the droop control theory presented in Section 2.4.3, as well as providing a benchmark for the analysis of Case B. The load sharing test with line impedance (Case B) aims to demonstrate the effect of resistive line impedances on the power and reactive power sharing of weak sources. The results obtained are compared and analysed in this section.

### 6.2.1 Collection and Normalisation of Results

*Results Collection*

Figure 6.1 (a) presents the set-up used to investigate the Pf-relationship, where the frequency is the theoretical control input. In the experiment, the DC armature current ($I_a$) is varied to adjust the output torque of the 22 kW SG. The measured torque is then used as the control input in the simulation. Figure 6.1 (b) investigates the QV-relationship, where the theoretical control inputs are the output voltages of the SGs. The field currents of both SGs are varied to adjust the output voltages, and the recorded field currents are used as the control input for the simulation. The output power and reactive power of the SGs are recorded for comparison.

Figure 6.1 illustrates the system input-output relationship of the Example Microgrid, including the control input, auxiliary input and the output results. The instruments used to measure the inputs and outputs are illustrated in Figure 4.7. Three sets of data are collected based on the three objectives of this experiment:

**To establish the model validity:** The same control variable applied to the Example Microgrid in the experiment is applied in the simulation. This creates a controlled environment to compare the simulation and the experimental load sharing results, i.e. $P_i, Q_i, Q_c$.

**To examine Pf- and QV-relationship:** For each load sharing test case, the control input is adjusted three times while $V_{pcc}$ or $\omega$ is kept constant. In order to keep $V_{pcc}$ and $\omega$ constant, auxiliary inputs are recorded in the experiment and included in the simulation model as a constant value.

For the Pf-relationship, the PCC voltage is kept constant, allowing the active power sharing to be examined under changing speed conditions. For the QV-relationship, the torque of 22 kW SG ($T_2$) is kept constant. This effectively allows the reactive power sharing to be analysed according to the change in voltage.

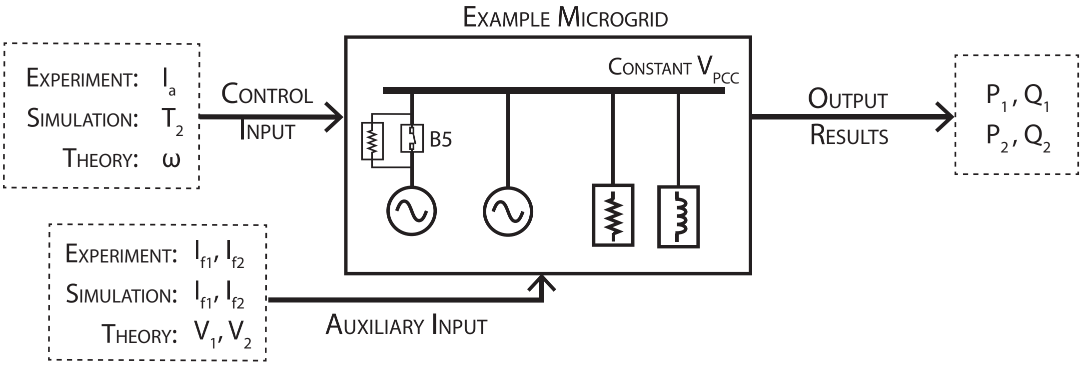


**a.** The set-up to examine the Pf-relationship.

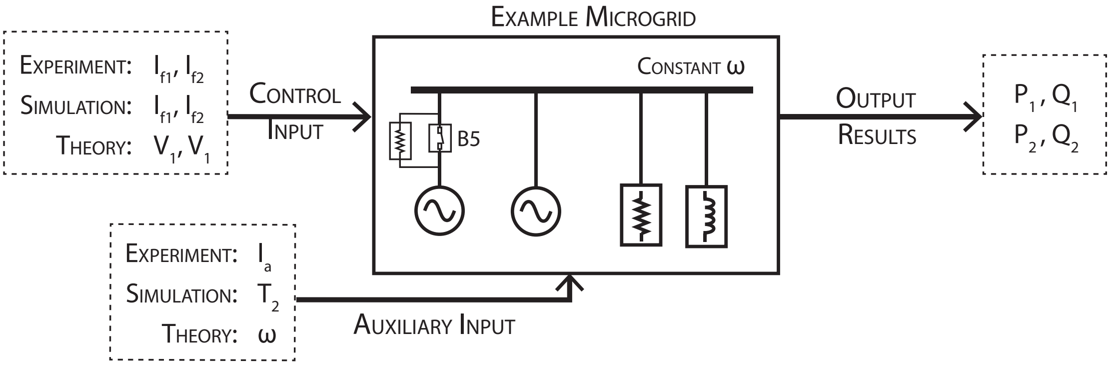


**b.** The set-up to examine the QV-relationship.

**Figure 6.1** The measurement and simulation set-up for the Load Sharing Tests.

**To investigate the effect of $\mathbf{R_{TL}}$:** The effect of a resistive-dominant line impedance on the Pf- and QV-relationship are investigated. The above two sets of data are collected with the line impedance connected to the generator by opening the breaker B5, as shown in Figure 6.1. This set of data is then compared with the above two sets (without the line impedance) to identify the similarities and differences.

*Results Normalisation*

Since the absolute value of the active and reactive power is of less importance than the load sharing percentage between the generators, the results are normalised to the total active power and the total reactive power. This allows the trend of Pf- and QV-relationship to be compared easily. Eq.(6.1) is applied to both the experimental and the simulation results.

$$
\begin{aligned}
P_1 &= \frac{P_1}{P_1 + P_2} & Q_1 &= \frac{Q_1}{Q_1 + Q_2} \\
P_2 &= \frac{P_2}{P_1 + P_2} & Q_2 &= \frac{Q_2}{Q_1 + Q_2}
\end{aligned} \tag{6.1}
$$

It must be noted that this normalisation is different from the commonly known *Per Unit* system, where the latter normalises the output power to the rating of each machine. Therefore, with this normalisation scheme, the sharing percentage for the 22 kW and the 75 kW SG adds up to 100%.

### 6.2.2 Case A: Steady-State Load Sharing without Line Impedance ($R_{TL}$)

Figure 6.2 presents the experimental and simulation results of Case A.1 and Case A.2 respectively. It is evident that the simulation results correspond well to the experimental measurements under all conditions. This confirms the validity of the simulation model, and satisfies the first objective of this experiment. This section analyses the results obtained in Case A, where the comparison between Case A and B are included in Section 6.2.3.

The x-axes in Figure 6.2 (a) represents the torque of the 22 kW SG. Although it is possible to plot $P_1$ against $T_1$, both $P_1$ and $P_2$ are shown against $T_2$. Since the total load demand ($P_1 + P_2$) is constant, increasing $P_2$ ($T_2$) implies decreasing $P_1$ ($T_1$), therefore only $T_2$ is shown on the graph to avoid clutter. Similarly, the x-axes in Figure 6.2 (b) represents the field current of the 22 kW SG even though the field current of the 75 kW SG is also varied.

#### *Droop Response*

Figure 6.2 (a) shows the Pf-relationship is evident, where the output active power sharing varies with the change of speed - increasing $T_2$ increases $P_2$ and decreases $P_1$ as expected. Figure 6.2 (b) presents the QV-relationship when the field currents ($I_{f1}, I_{f2}$) of the SGs change. It can be seen that increasing $I_{f2}$ increases $Q_2$ and decreases $Q_1$ as expected.

#### *Case A.1: Relationship between Q and f in Pf-Droop*

According to the Pf-droop theory, changing the speed should not change the reactive power. However, in the results shown in Figure 6.2 (a), the reactive power also appears to be dependent on the speed even without line impedance present. This is because the voltage is not identical everywhere in the microgrid and the causal effect is described below:

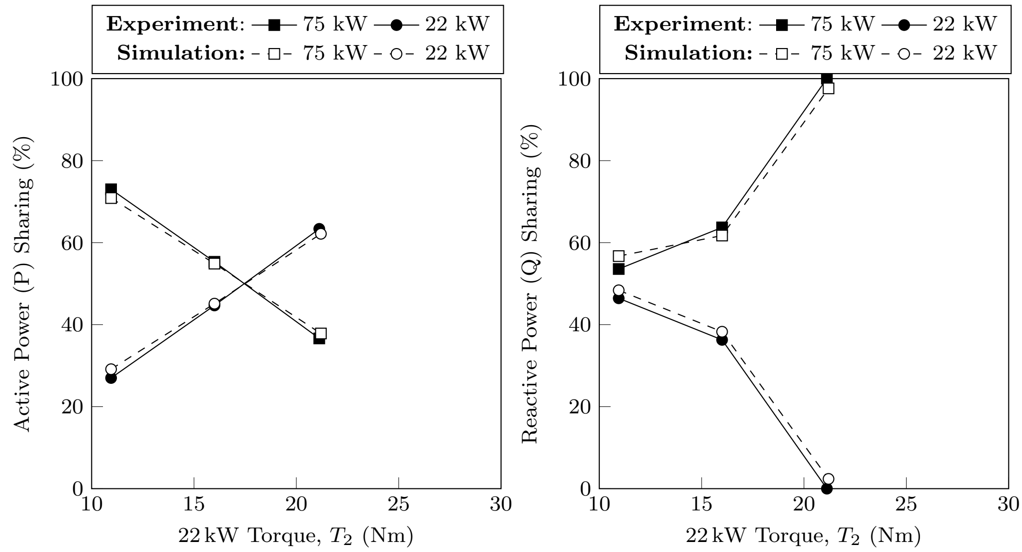


**a.** Case A.1: Pf-relationship.

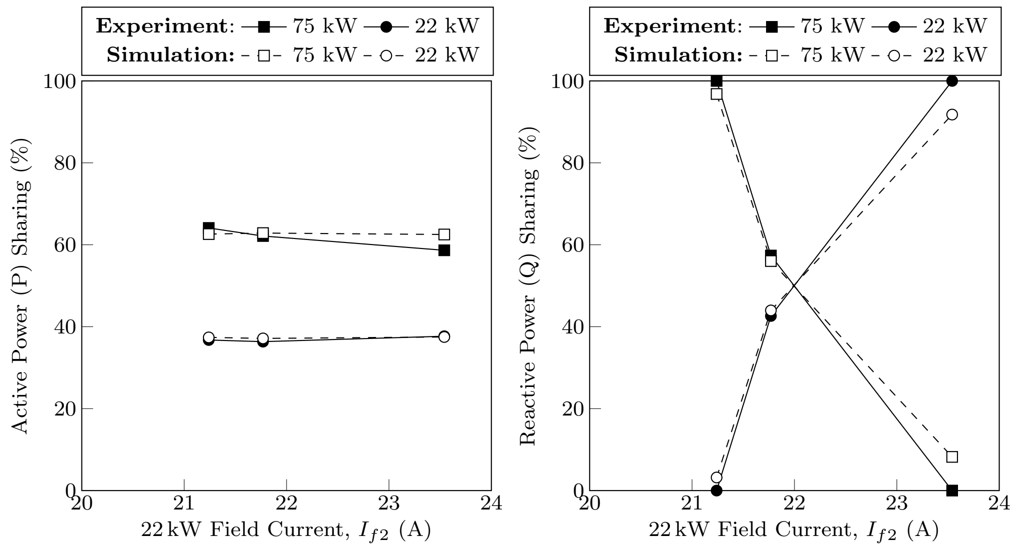


**b.** Case A.2: QV-relationship.

**Figure 6.2** Case A: Experimental and simulation results of Load Sharing Tests without line impedances.

1. As $T_2$ (and hence $P_2$) increases, the voltage drop across the internal impedance of the SG increases, causing the output voltage of the 22 kW SG to decrease.
2. Therefore, the voltages are manually controlled by adjusting the field currents to keep the $V_{pcc}$ magnitude constant.
3. However, the phase difference $\theta$ between the voltage and current, which defines the reactive power, is difficult to keep constant with manual control.
4. As a result, 75 kW SG picks up the majority of the reactive power load because it has a higher terminal voltage.

The simulation result in Figure 6.2 (a) uses the experimental result $(I_{f1}, I_{f2})$ as the auxiliary input, therefore the simulation has the same response as the experiment. Due to the lack of voltage regulators, increasing $T_2$ changes the reactive power sharing in the experiment.

*Case A.2: Relationship between $P$ and $V$ in QV-Droop*

Similarly, according to the QV-droop theory, active power output should be independent of the voltage. However, Figure 6.2 (b) shows that changing the field current affects the active power sharing. This is because as $Q_2$ increases, the SG slows down due to loading and $P_2$ decreases. Due to the lack of speed regulators to keep the speed constant, manual adjustment of $T_2$ is performed since the frequency is identical everywhere in the microgrid.

*Case A: Comparison between $Q, f$ and $P, V$*

It is also clear that the variation of the active power is smaller for the QV-relationship (as shown in Fig.6.2 (b)) compared to the variation of the reactive power for Pf-relationship (as shown in Fig.6.2 (a)). This may be because the reactive power load is 25% of the active power load, therefore comparatively it has less impact.

More importantly, the total active load is constant and the speed is identical everywhere in the microgrid. Therefore, only $T_2$ needs to be re-adjusted since $T_1$ is inversely proportional to $T_2$. However, the voltage is not the same at different points of the microgrid and changing $I_{f2}$ does not affect $I_{f1}$.

However, it is difficult to keep $T_2$ constant since the resolution of the variac that controls the speed $(I_a)$ of the 22 kW SG is not fine enough. In order to demonstrate this effect, $T_2$ is kept constant in the simulation instead of using the measured torque as the auxiliary input. The simulation results show that by keeping $T_2$ constant, the change in field current has negligible effect on the active power sharing, as seen in Figure 6.2 (b).

### 6.2.3 Case B: Steady-State Load Sharing with Line Impedance ($R_{TL}$)

Figure 6.3 compares the experimental and simulation results of Case B.1 and Case B.2, which shows that the simulation results correspond well to the measurements. This confirms that the simulation model developed is valid, even with the line impedance present, still satisfying the first objective of this experiment. This section analyses the results obtained in Case B as well as discusses the similarities and differences between Case A and B.

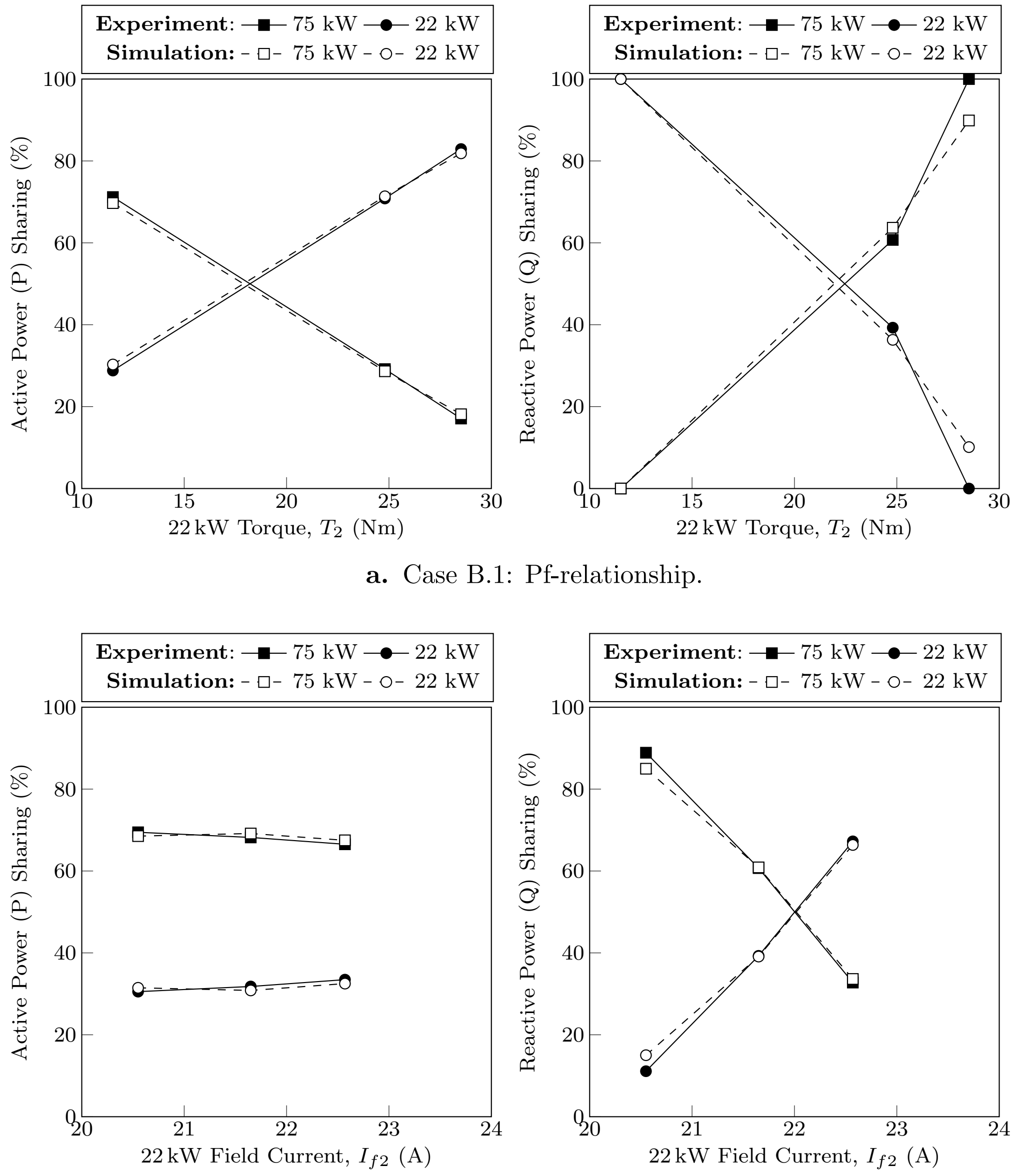


**a.** Case B.1: Pf-relationship.



**b.** Case B.2: QV-relationship.

**Figure 6.3** Case B: Experimental and simulation results of Load Sharing Tests with line impedances.

*Droop Response*

The Pf-relationship is presented in Figure 6.3 (a) and the QV-relationship is presented in Figure 6.3 (b). It is shown that the $P - vs - T_2$ and $Q - vs - I_{f2}$ trend of Case B follows closely to the trend of Case A. Through increasing $T_2$, $P_2$ increases while $P_1$ decreases, and increasing $I_{f2}$ increases $Q_2$ while decreases $Q_1$.

### *Case B.1: Relationship between $Q$ and $f$ in Pf-Droop*

It was discussed earlier that the resistive line impedance causes a coupling between the active and reactive power, where changing the speed has an impact on the reactive power sharing. This effect is demonstrated in Figure 6.3 (a).

The effect of change of speed on reactive power is more severe in Case B.1 compared to Case A.1. In Case A.1, a 1 Nm change in torque translates to 3.5% change in load sharing, whereas a 1 Nm change in torque in Case B.1 translates to a 6.0% change in load sharing. This is expected since the resistive line impedance in Case B.1 worsens the active and reactive power coupling effect.

### *Case B.2: Relationship between $P$ and $V$ in QV-Droop*

It is seen in Figure 6.3 (b) that changing the field currents affect the active power sharing. This may also be due to the active and reactive power coupling discussed previously. The effect of change of voltage on the active power sharing is also more severe in Case B.2 compared to Case A.2.

In addition, the simulation torque is kept constant in both Case A.2 and B.2, yet only in Case B.2 is the active power shown to be affected by the changing field current. Therefore, it may be concluded that including the resistive line impedance results in a coupling between the active and reactive power.

### *Voltage and Current Waveform*

In order to validate the authenticity of the results, the experimental and simulation voltage and current waveforms of the 22 kW in Phase A and the current of the 75 kW in Phase A were obtained. Figure 6.4 presents the waveforms obtained. The experimental results are recorded with the oscilloscope, where a 50 Hz digital low pass filter is applied to the signal to obtain the fundamental waveform at 25 Hz. Section 6.3.1 discusses the use of the low pass filter in more detail.

It can be seen that the voltage magnitude of the simulation result is slightly higher than the experimental measurement, which translates to a higher current magnitude for both SGs. The phase shift between the experimental and the simulation results is marginal. The 22 kW SG current is slightly non-linear in the experiment, which may be due to saturation in the generator. Since saturation is not modelled, the simulation shows a perfectly sinusoidal current waveform. In general, the experimental and simulation waveforms show very good correlation for both the magnitude and phase for all measurements.

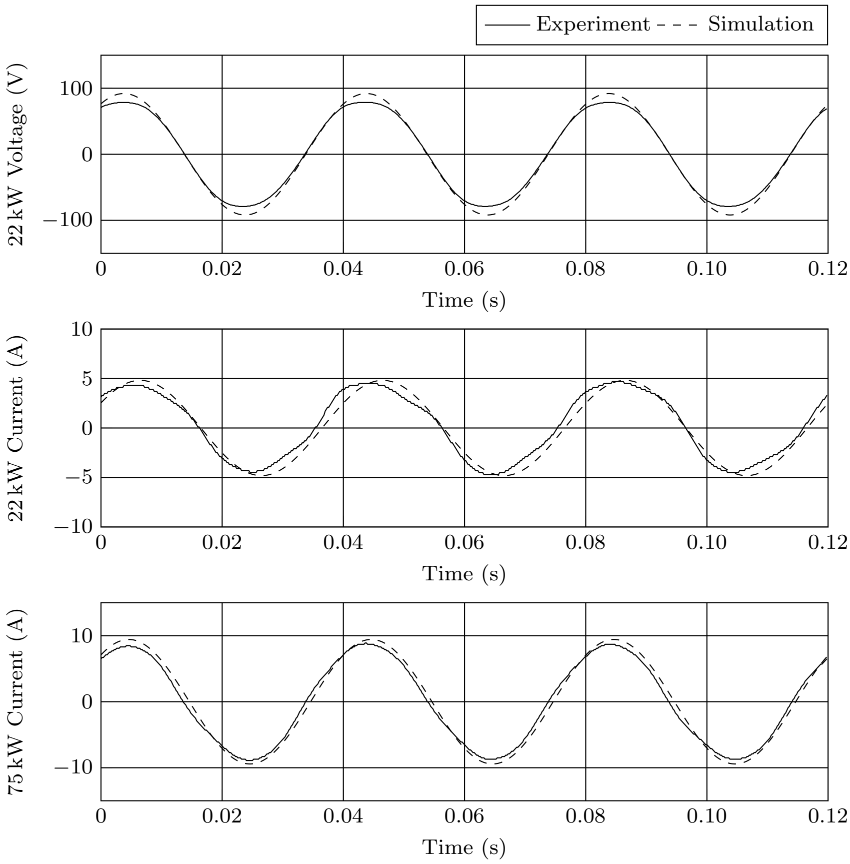


**Figure 6.4** Steady-state voltage and current waveforms.

## 6.3 Transient Test Results and Analyses

The transient experiments examine how the system responds to disturbances in the experimental and simulated Example Microgrid. This research aims to investigate the steady-state load sharing based on droop control; however, it is interesting to see how the system responds during transient changes. Further understanding into the limit of the model may be obtained.

Case A.3 and Case B.3 examine the effect of a resistive-dominant line impedance on the transient load sharing, where a 1.7 kW resistive step load is introduced to the system for both Cases. In Case C, the line impedance is switched in series to connect with the 75 kW SG. This experiment aims to provide more data about how the system responds to a disturbance. Although this is not a normal operating condition, it provides additional data for the comparison of experimental and simulation results.

### 6.3.1 Collection and Normalisation of Results

*Results Collection*

Figure 6.5 depicts the input-output relationship of Example Microgrid for the transient experiments. The purpose of this experiment is to examine the steady-state load sharing as well as the step response, therefore, the currents of the SGs are recorded over 5 seconds.

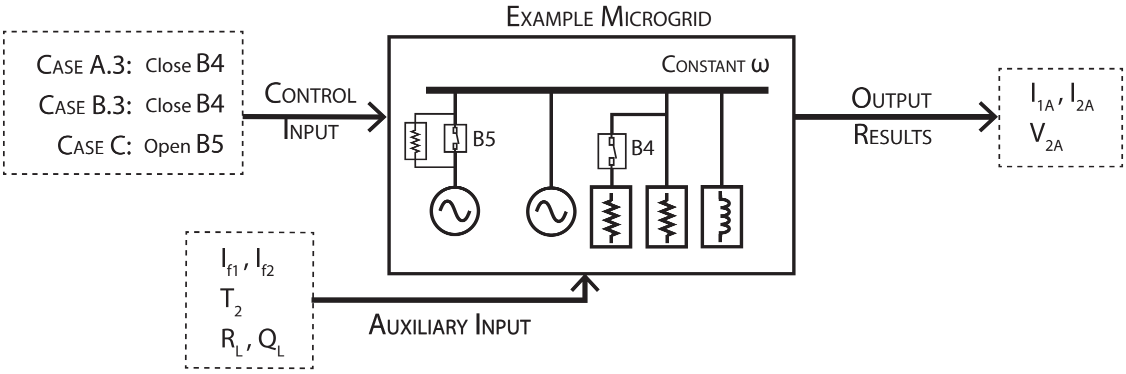


**Figure 6.5** Measurement set-up for transient experiments.

The control input for Case A/B.3 and Case C is the position of the breakers B4 and B5 respectively, as shown in Figure 6.5. The control input and output measurements are illustrated in Figure 4.7. For all cases in the transient study, the auxiliary input variables are recorded in the experiment at steady-state and used as parameters for the simulation model. This allows the output experimental and simulation results to be compared to each other, for identical system disturbances.

The auxiliary input variables are recorded with the instrumentation devices described in Section 4.3. The step change is triggered externally by measuring the PCC current for Case B and the current through breaker B5 for Case C.

*Results Post-processing*

The data obtained from the oscilloscope has 602 sampling points per channel due to a small internal memory; therefore, in order to record the transient and steady-state results, the experiment is repeated twice to obtain the output currents with different time periods. The 5 s waveforms show both the transient and steady-state response, whereas the 20 ms waveforms show only the first couple of cycles when the step change occurs.

In order to filter out the high frequency noises from the machine vibrations, a low pass filter is applied to the 20 ms waveform using the built-in digital filter of the oscilloscope. Figure 6.4 shows that the filter extracts the fundamental waveform at

25 Hz. The 50 Hz low pass filter is selected since it is the lowest cut-off frequency available.

The 5 s waveform cannot be filtered directly, due to the limitations of the oscilloscope. In addition, the 5 s signal suffers from significant aliasing, where each cycle only has five to six measured data points due to the low sampling rate. An RMS value is calculated for the 5 s waveforms to allow for an easier visual inspection of the load sharing, as well as reducing the measurement error due to aliasing.

The true RMS values are calculated based on the measured instantaneous results, as shown in Eq.(6.2). A running-average-window of one cycle ($T$) of the signal at the fundamental frequency of the current waveform is computed, where $T = \frac{1}{25 \text{ Hz}} = 0.04$ s.

$$RMS(I(t)) = \sqrt{\frac{1}{T}\int_{t-T}^{t} I(t)^2} \tag{6.2}$$

Additional details of the results processing are included in Appendix D. The unfiltered signal, the comparison between the 5 s signal and the 20 ms signal during sub-transient conditions, and the RMS calculations of the signals with aliasing are discussed.

### 6.3.2 Case A: Step Load without Line Impedance

Figure 6.6 compares the experimental and simulation results of Case A.3, where the 1.7 kW step resistive load is introduced at $t = 0$. It can be seen that before the step load occurs, the experimental and simulation results at steady-state have good correlation. The analysis of the step response can be separated into three parts: the sub-transient, transient and the steady-state.

From Figure 6.6 (a), it can be seen that the simulated currents correspond well to the sub-transient experimental results. Figure 6.6 (b) shows the sub-transient current waveforms, where the results show good correlation in both the magnitude and phase of the currents.

The largest error occurs during transients, where the overshoot of the experimental current is $\approx 2.5$A more than the simulated value. The difference between the simulated and experimental results during transient may be because the simulation assumes a constant input for the field current, whereas the variac that supplies the field currents to the generators may have dynamic characteristics which are not included in the model. In addition, the results are taken from Phase A measurements and simulation of the SG only, and no considerations is given to the other two phases.

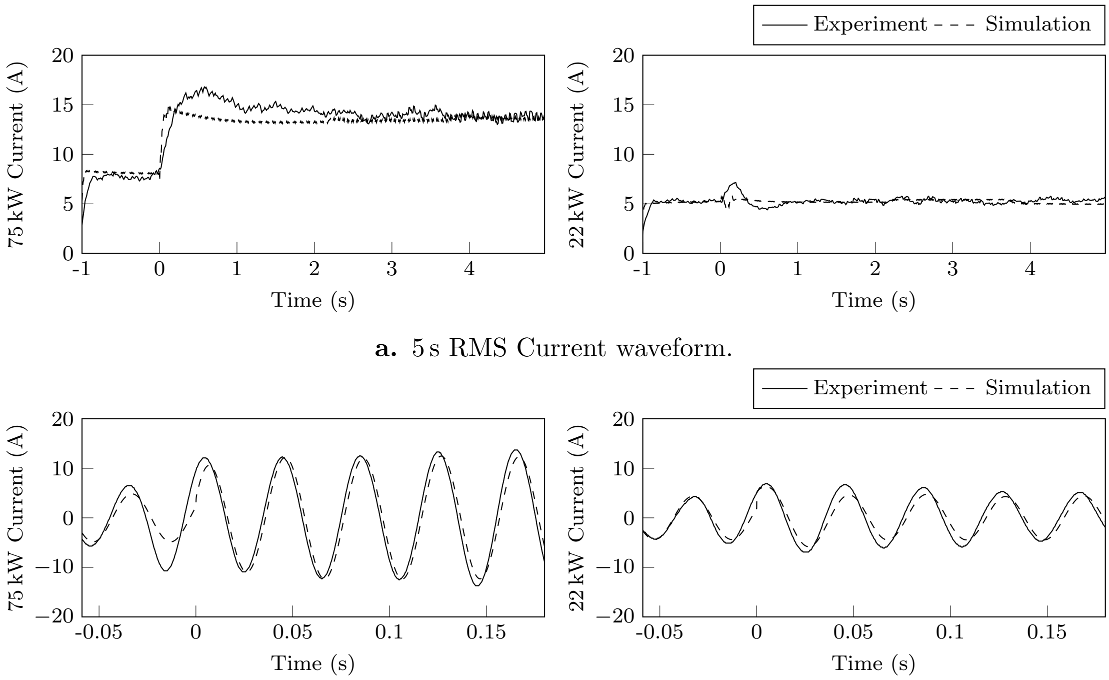


**a.** 5 s RMS Current waveform.

**b.** 20 ms Current waveform.

**Figure 6.6** 2 kW step load without line impedance.

At steady-state, the discrepancy between the simulated and experimental results is small and may be attributed to the lack of a 50 Hz filter, aliasing and measurement error (see Appendix D for detail).

### 6.3.3 Case B: Step Load with Line Impedance

Figure 6.7 compares the experimental and simulation results of Case B.3, where the 1.7 kW step resistive load is introduced at $t = 0$. The results of Case B.3 is similar to that of Case A.3, with the main difference being the overshoot current and the steady-state load sharing.

Table 6.2 compares several aspects between Case A.3 and Case B.3. It can be seen that there are several differences between the two cases in both transient and steady-state.

**Table 6.2** Comparison between Cases A.3 and B.3.

| | **Comparisons** | **No** $R_{TL}$ | **With** $R_{TL}$ |
|---|---|---|---|
| Transient | Trigger Current (A) | 16.7 | 15.7 |
| | Overshoot | More | Less |
| | Time to Steady-state | Longer | Shorter |
| Steady-State | Load Sharing Before (%) | 58:42 | 51:49 |
| | Load Sharing After (%) | 73:27 | 63:37 |
| | Theoretical Load Sharing After (%) | 73:27 | 68:32 |

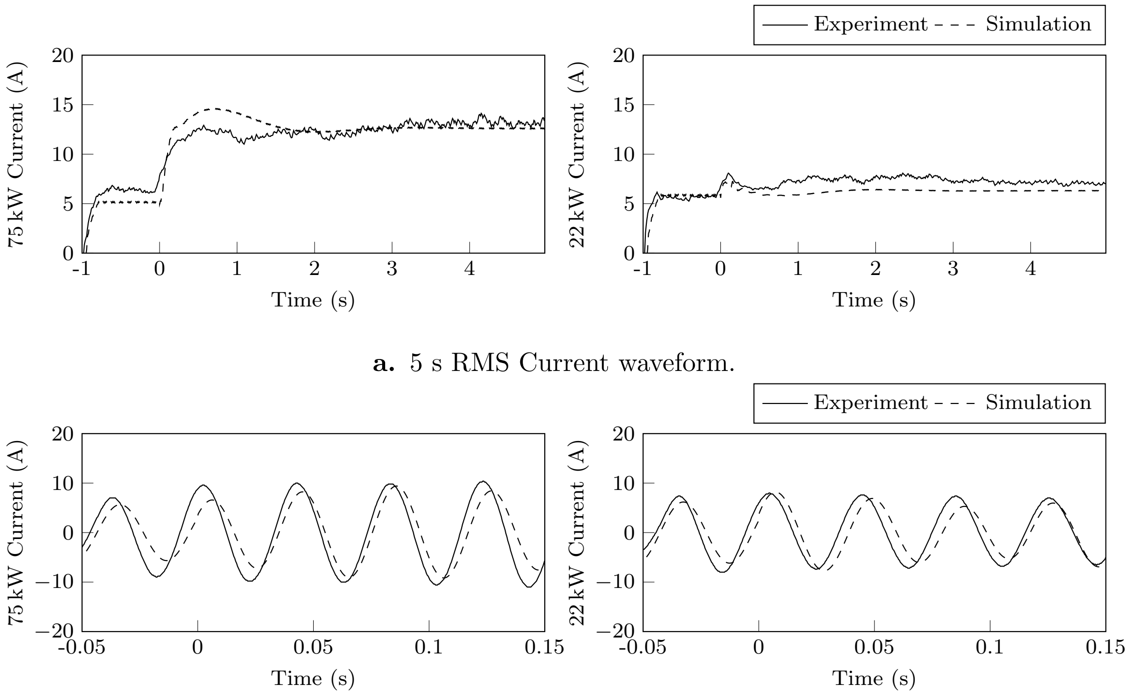


**a.** 5 s RMS Current waveform.

**b.** 20 ms Current waveform.

**Figure 6.7** 2 kW step load With line impedance.

The instantaneous voltage at the time where the breaker closes has a significant impact on the transient response. When the breaker is closed near the zero-crossing point, the corresponding instantaneous current is less. Therefore, the trigger current and overshoot will be lower and the time to steady-state will be shorter if the breaker closes at the time when the instantaneous voltage is low. However, the breaker is not controlled to be closed at a specific instantaneous voltage, but manually closed at random. As a result, the differences between the two cases cannot be directly correlated to the line impedance.

On the other hand, for the steady-state results, the differences can be attributed to the resistive line impedance, as it is the only changing variable between the two cases. Since the output torque of the 22 kW SG is not changed, the step change in load is only picked up by the 75 kW SG. Therefore, the theoretical load sharing is calculated as follows, where $S_1$ is the apparent power of the 75 kW SG:

$$\text{Load Sharing of } \mathrm{S_1}\ [\%] = \frac{\mathrm{S_{1_{before}}} + \mathrm{S_{step}}}{\mathrm{S_{1_{before}}} + \mathrm{S_{step}} + \mathrm{S_{2_{before}}}} \tag{6.3}$$

It is evident that without the line impedance, the load sharing after the step change is identical to the theoretical load sharing by keeping the torque constant. However, with the line impedance added, the active power sharing is changed even if the torque is kept constant. This result is discussed in Section 6.2.

### 6.3.4 Case C: A Minor Transient Disturbance

Figure 6.8 compares the experimental and simulation results of Case C. At time $t = 0$, the line impedance is switched in between the output of the 75 kW SG and the PCC. The graph shows that for both voltage and current, the simulated results resemble the experimental results.

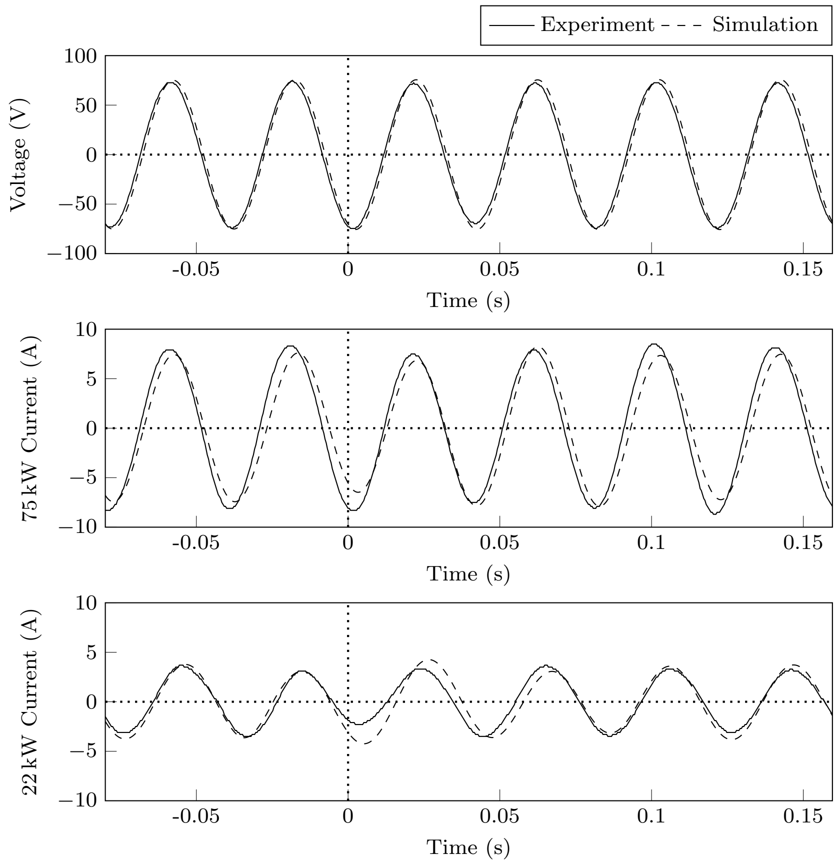


**Figure 6.8** Case C: Experimental and simulation results under a transient disturbance.

As seen from Figure 6.8, this disturbance is barely discernible in the experimental results, where only the 75 kW SG current dips for one cycle as the switch closes. The simulation results show slightly more dynamics, where the current for the 22 kW SG has an increase at the same time the 75 kW SG current experiences the dip.

The disturbance is small, and can only detected by the change in current through the breaker B4 rather than the change in PCC current for Case A/B.3. The experimental measurement shows a little change during the disturbance at time zero, since the dynamics may be filtered out by the 50 Hz low pass filter.

## 6.4 Discussion and Summary

Several experiments are performed on the Example Microgrid in the Genmin Laboratory. The three main objectives of these experiments are: (1) to validate the Simulink model, (2) to examine the Pf- and QV-relationship, and (3) to investigate the effect of line impedance on the load sharing.

To meet the first objective, the same control variables applied to the experiment are also applied to the simulation, where the system responses are compared and contrasted. The Pf-relationship is examined by looking at the change in active power when the speed is varied and the QV-relationship at the change in reactive power when the voltage is varied. A resistive line impedance is connected to the output of the 75 kW SG to investigate the effect of line impedance on load sharing. The step response with and without the line impedance is also analysed.

For the step response, the sub-transient and transient simulation results correlate less with the experiment and may need to be investigated further. The aim of the research is focused on the steady-state load sharing; the transient studies are performed to identify the boundaries of the model. Therefore, the transient errors are identified but not rectified.

The steady-state results for the load sharing experiments, as well as the transient experiments show very good correlation between simulation and measurement, where the discrepancies are within the limits of a 5% measurement error. Therefore, the Simulink model is deemed to be able to represent the physical system without compromising the pertinent aspects under steady-state operation.

The Pf- and QV-relationship can be observed clearly with the load sharing experiments. It is shown that by adjusting the $T_2$, the active power sharing is controlled and the reactive power is controlled by varying the field currents. Although the load sharing experiment conducted is slightly different from the operation of the droop controller, the underlying theory is the same. It is concluded that the simulated Example Microgrid is able to demonstrate the droop response.

From the steady-state experiment, it is seen that load sharing is affected by the line impedance. However, due to the lack of speed and voltage regulators, the correlation between the line impedance and the power and reactive power coupling is inferred instead of proven directly.

Due to the limitations of the experimental set-up, some arguments can only be inferred. However, according to the results obtained as a whole, the simulation model is able to represent the Example Microgrid under steady-state conditions. The Pf- and QV-relationship is observed, and the line impedance has an impact on the steady-state load sharing of the SGs.

In this chapter, the primary aim of this research is achieved. The simulated Example Microgrid is deemed to reflect the physical Example Microgrid under steady-state conditions. The next chapter builds on the simulation environment that is validated in this chapter to perform further investigation on the Example Microgrid.

# CHAPTER 7

## Simulation of Droop Controller in Example Microgrid

This chapter aims to fulfil the secondary aim of this research, which is to investigate the performance of conventional droop controllers in the Example Microgrid. The conventional Pf- and QV-droop controllers are first developed, then the effects of resistive-dominant line impedance on the generators' load sharing is demonstrated from the Simulink results. The parameters that reduce the efficacy of the controllers are subsequently investigated. The focus of this chapter is on the inaccurate steady-state reactive power sharing. It is proven that the simulation environment is capable of investigating the effects of different control strategies in a complex power system.

### 7.1 Introduction

In order to realise the "plug-and-play" feature that is advocated for microgrids, the frequency and voltage droop control are widely adopted to regulate the active and reactive power sharing amongst parallel-operated sources [3, 9, 15, 19, 21]. However, conventional droop control is developed based on the assumption of an inductive-dominant line impedance, whereas a low-voltage microgrid has a resistive-dominant line impedance, as seen Table 2.4.

Through corroborating the simulation results with the experimental results in Chapter 6, it is concluded that the Simulink model of the Example Microgrid is able to accurately represent the physical system. Therefore, in addition to the experimental test cases conducted in Chapter 6, this chapter further investigates the generators' load sharing with the presence of droop controllers.

The mathematical derivation of the droop controller is first presented. The controller block diagram are presented and the parameters selection are discussed . The effects of line impedances on the load sharing is then demonstrated with 10 Case studies. With the mathematical derivation in mind, the parameters that influence the load sharing, including the distance, power factor and total load are investigated. Concluding, the inherent limitations of the conventional droop controllers are presented.

### 7.1.1 Mathematical Derivation of Reactive Power Sharing Error

As stated in Chapter 2 that the non-negligible line resistances result in a steady-state reactive power sharing error and an undesired active and reactive power coupling. The presence of an unequal line impedance further reduces the efficacy of the droop controller. It is also observed in literature that the line impedance may result in a large circulating reactive current as well as affecting the transient stability of the system [33].

This section aims to identify the reactive power sharing error solely due to the line impedances. However, due to the complexity of the problem, the derivation of the reactive power sharing error is simplified by the following assumptions:

- Local loads are disregarded.
- Both generators are equally rated, hence have the same droop slopes $m_1 = m_2$.
- Assume the initial dispatched reactive power is zero ($Q_1^* = Q_2^* = 0$).
- Resistance is negligible since its effect is already discussed in Section 2.5.1.

These assumptions allow the reactive power sharing error to be described by Eq.(7.1), where the derivation of this equation is included in Section A.2.1, Appendix A.1:

$$Q_1 - Q_2 = \frac{V_{pcc}(X_2 - X_1)(V^* - V_{pcc})}{X_1 X_2 - X_1 V_{pcc} m_1 - X_2 V_{pcc} m_1 + V_{pcc}^2 m_1^2} \tag{7.1}$$

It is clear from Eq.(7.1) that the reactive power sharing is dependent on the droop slope ($m_i$), the PCC voltage ($V_{pcc}$) and the line impedances ($X_i$). The line impedance is a function of the physical distance between the SG and the PCC. The further the SG is from the PCC, the larger the line impedance.

The PCC voltage is an ill-defined parameter that cannot be directly controlled and the line impedances are unknown and uncontrollable variables. Although the droop slope is a tunable parameter, it cannot be selected arbitrarily to achieve desired performance. This result concurs with the findings of *He and Li* [48] as well as *Gu et al.* [47]. The selection of droop slope is further discussed in Section 7.2.2.

### 7.1.2 Overview of Simulation Test Cases

A total of 10 simulation test cases were performed on the Example Microgrid, which are independent of the experimental test cases conducted in Chapter 6. Figure 7.1 illustrates the Simulink set-up, which is almost identical to the model implemented in Chapter 6. Comparing Figure 5.1 with Figure 7.1, it is seen that the set-points $\omega_1, T_2, i_{f1}, i_{f2}$ in Figure 5.1 are replaced by autonomous droop controllers in Figure 7.1.

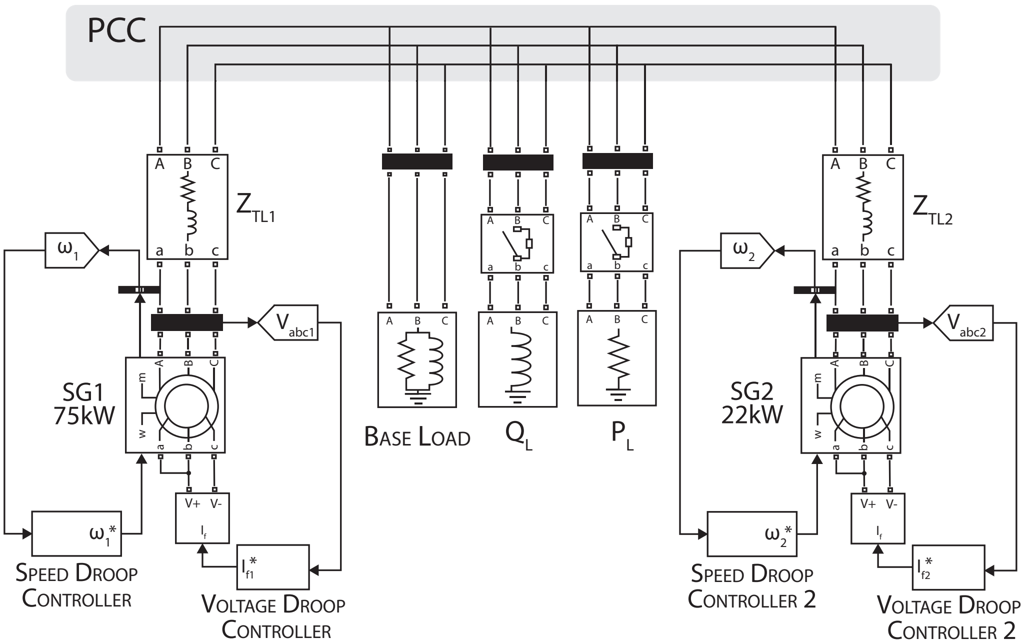


**Figure 7.1** Example Microgrid in different case scenarios.

Figure 7.1 shows the high-level Simulink block diagram of the model where there are two generators, a base load and two step loads. Both of the generators are connected to the PCC via a line impedance $Z_{TL}$. The speed and voltage droop controllers are implemented as depicted in Figure 7.2 and Figure 7.3 respectively. For all the parameters and variables associated with the 75 kW SG, the subscript 1 is used, whilst subscript 2 denotes the parameters associated with the 22 kW SG.

Table 7.1 summarises the test cases that are performed in Simulink. In Section 7.3.1, Case 1 - 3 examine the effect of a line impedance on the inaccurate reactive power sharing. In Section 7.3.2, Case 4 - 7 demonstrate the active and reactive power coupling. In Section 7.4, Case 8-10 investigates the parameters that influence the reactive power sharing accuracy. In the table, the variable under investigation is presented. The tick ($\surd$) shows what was implemented for each case, for example, the droop controller was implemented for all the cases and an equal line impedance is implemented for Case 2 and Case 4-11. In Appendix E, the impact of the controller gains $k_p, k_i$ on the transient response is presented.

**Table 7.1** Summary of all the test cases.

| Case | Droop | $Z_{TL1} = Z_{TL2}$ | $Z_{TL1} \neq Z_{TL2}$ | Change Only $P_L$ (kW) | Change Only $Q_L$ (kVAR) | Change $Z_{TL}$ | Change Gains |
|---|---|---|---|---|---|---|---|
| 1 | Drooped | | | | | | |
| 2 | √ | $\mathbf{0.25Z_{LV}}$ | | | | | |
| 3 | √ | | $\mathbf{0.1Z_{LV}}$, $\mathbf{0.4Z_{LV}}$ | | | | |
| 4 | √ | √ | | | **3.64** | | |
| 5 | √ | √ | | **4.85** | | | |
| 6 | √ | √ | | **5×0.97** | | | |
| 7 | √ | √ | | √ | | **MV, HV** | |
| 8 | √ | √ | | Change PF | | $\mathbf{0\text{–}1.2Z_{LV}}$ | |
| 9 | √ | √ | | **0 - 8 kW** | | | |
| 10 | √ | √ | | **0.7-1 PF** | | √ | |

## 7.2 Droop Controller Simulations

To evaluate the effectiveness of the conventional droop controllers described in Section 2.4.3, the design of the Pf- and QV-droop controllers are presented in this section. The comparison between the generators' response with and without the droop controller is subsequently analysed.

### 7.2.1 Droop Controller Set-Up

Conventionally, the machine shaft speed and voltage is regulated to 1 p.u. through a speed governor and a voltage regulator. The droop controller biases the set-points of the governor and regulator based on the active and reactive power demand respectively.

*Pf-Droop Controller*

Figure 7.2 shows the Simulink block diagram of the speed governor equipped with droop control. The negative feedback with the PID control tracks the reference $\omega$, which is set at 1 p.u. (i.e. 25 Hz for the Example Microgrid). The active power load reference $P_i$ biases the set-point negatively to achieve the droop response, where $m_p < 0$. A diesel engine is the envisaged prime-mover for this application. A transportation delay of $0.2s$ is selected to represent a generic engine action and the transfer function is implemented as $^1/_1$ for simplicity.

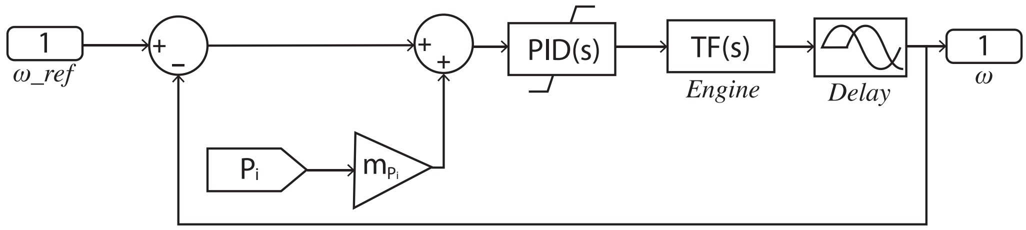


**Figure 7.2** Speed governor with droop control.

*QV-Droop Controller*

Figure 7.3 shows the Simulink block diagram of the voltage regulator with droop control. The voltage reference tracking is achieved through negative feedback of the positive-sequence voltage. The reference voltage is set at 1 p.u., which is 120 $V_L$ for the Example Microgrid. The reactive power load reference negatively biases the voltage to achieve the QV-droop response, where $m_q < 0$.

The symmetrical components[1] are used to analyse the system operation under unbalanced conditions [62]. The Example Microgrid is balanced and the generators are positive-sequence sources, the positive-sequence voltage is used as the feedback signal.

Phase-Locked Loops (PLLs) are the most popular method in synthesising the phase and frequency information in the system for PE sources [63]. It is not necessary for the Example Microgrid to include the PLL since the SGs are locked in synchronous speed as synchronous generators. In the simulation however, the PLLs are included in the controller to provide the phase angle for the Park's Transformation [2]. The Park's Transformation is used to measure the positive-sequence component as suggested by Mathworks [59].

[1]In a three-phase system, the symmetrical components $V_{012}$, namely the zero, positive and negative sequence components, are an alternative representation of the three-phase phasors $V_{abc}$. The use of symmetrical component is essential in the design of the protection systems and stability studies [8, 62].

[2]Park (or dq0) Transformation simplifies a three-phase balanced power system by eliminating time-varying inductances.

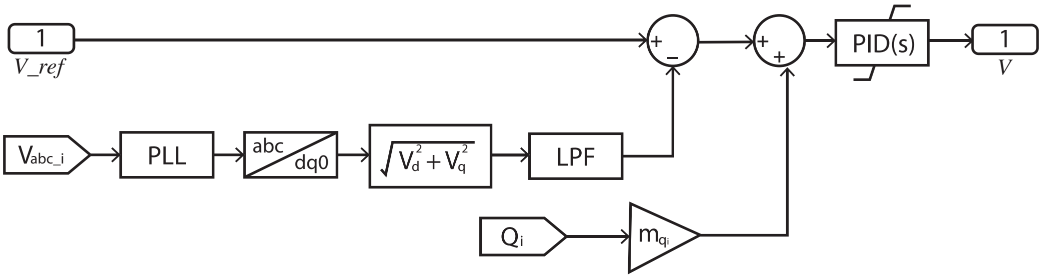


**Figure 7.3** Voltage regulator with droop control.

*Instantaneous Calculation of the Active and Reactive Power Demand*

The Example Microgrid is assumed to be balanced with pure linear loads, the calculation of the instantaneous power and reactive power demand is based on the fundamental voltage and current. The calculation of the power and reactive power $P_i, Q_i$ in Figure 7.2 and Figure 7.3 are shown in Eq.(7.2), where $|V|$ and $|I|$ are instantaneous voltage and current magnitude.

$$\begin{aligned} P &= 3\,\frac{|V|}{\sqrt{2}} \times \frac{|I|}{\sqrt{2}} \times \cos\theta \\ Q &= 3\,\frac{|V|}{\sqrt{2}} \times \frac{|I|}{\sqrt{2}} \times \sin\theta \\ \theta &= \angle V - \angle I \end{aligned} \tag{7.2}$$

### 7.2.2 Design of Controller Parameters

There are three sets of parameters that need to be chosen for the speed and voltage droop controllers: (1) the droop coefficientss $m_{P_i}, m_{Q_i}$, (2) the PI controller gains $k_p, k_i$ and (3) the design of the Low Pass Filter (LPF).

*Droop Coefficients*

It is suggested that a larger droop coefficient achieves a better transient load sharing [29] as well as reduces the reactive power sharing error [47]. However, given the minimum allowable system voltage and frequency, the droop coefficients cannot be arbitrarily large.

The droop slopes $m_{P_i}, m_{Q_i}$ are chosen based on the maximum allowable deviations of the frequency and voltage from the rated values respectively. By considering a

3% drop in system frequency and a 10% drop of system voltage at rated power, the droop slopes are designed as follows [3]:

$$m_{P_i} = \frac{0.03}{P_{i_{max}}} \tag{7.3a}$$

$$m_{Q_i} = \frac{0.10}{2\,Q_{i_{max}}} \tag{7.3b}$$

For simplicity, $P_{i_{max}}, Q_{i_{max}}$ are taken as a quarter of the nameplate ratings of the SGs as they are running at half speed. The droop coefficients of the SGs are recorded in Table 7.2.

*Controller Gains*

The performance of the PI controller is based on three criteria: (1) a small transient speed and voltage, (2) a fast restoration to nominal system operating conditions and (3) a satisfactory stability margin. Table 7.2 records the controller gains for both the speed and voltage controller.

**Table 7.2** Controller parameters for individual generators (unit-less).

| | **22 kW SG** | | **75 kW SG** | |
|---|---|---|---|---|
| **Droop Coefficients** | $\mathbf{m_P}$ | $\mathbf{m_Q}$ | $\mathbf{m_P}$ | $\mathbf{m_Q}$ |
| | $2.67 \times 10^{-6}$ | $9.09 \times 10^{-6}$ | $1.60 \times 10^{-6}$ | $5.45 \times 10^{-5}$ |
| | $\mathbf{k_p}$ | $\mathbf{k_i}$ | $\mathbf{k_p}$ | $\mathbf{k_i}$ |
| **Speed Governor** | 6 | 14 | 6 | 14 |
| **Voltage Regulator** | 250 | 60 | 300 | 150 |

The steady-state error and rise time are both inversely related to the proportional gain. The integral action removes the steady-state error, however, a large $k_i$ causes an overshoot. The droop controllers require a high value of feedback gain to ensure the desired load sharing and it is reported in [41] that this is especially important under weak grid conditions. Although a large integral feedback is necessary to achieve a smaller steady-state error, the stability margin is worsened, compromising the dynamic performance.

With this in mind, the PI controller gains are chosen heuristically based on the controller response [39]. In addition, the PI controller has a bounded integral term in order to prevent integral wind-up since it is assumed that large step loads occur frequently.

**Table 7.3** Operating conditions of Example Microgrid for all test cases.

| | Parameters | $t = 0 - 1$ | $t = 1 - 4$ | $t = 4 - 7$ |
|---|---|---|---|---|
| Load | $P_L$ (kW) | 9.94 | 15.28 | 9.94 |
| | $Q_L$ (kVAR) | 7.47 | 11.30 | 7.47 |
| | $S_L$ (kVA) | 12.43 | 19.00 | 12.43 |
| Generator | $P_i$ (p.u.) | 0.4 | 0.6 | 0.4 |
| | $Q_i$ (p.u.) | 0.3 | 0.45 | 0.3 |
| Droop | $f_i$ (p.u.) | 0.9880 | 0.9820 | 0.9880 |
| | $V_i$ (p.u.) | 0.9850 | 0.9775 | 0.9850 |

It is observed in Appendix E.1 that the gains, if not tuned correctly, may have a significant impact on the transient load sharing of the generators.

*Low Pass Filters*

Since the Example Microgrid contains linear loads only, it is assumed that the high frequency components present are due to vibration and measurement noise. Therefore, a first order LPF with the cut-off frequency $\omega_c = 2\pi 50$ is implemented as shown in Eq.(7.4). The upper-limit 50 Hz is selected to be consistent with the cut-off frequency used for the experimental set-up of the Example Microgrid.

$$H(s) = \frac{1}{1 + s/\omega_c} \tag{7.4}$$

The LPF is implemented in the voltage controller as shown in Figure 7.3. The simulation is performed in the continuous time domain, so that the transfer function is not discretised.

### 7.2.3 Droop Controller Simulation Results

Generators typically have the capability to provide rated power at 0.8 lagging power factor [7]. In order to examine both the active and reactive power sharing, the base load is designed to be $S = 0.4 + j\ 0.3$ per unit, and a step load of $S = 0.2 + j\ 0.15$ per unit. The two SGs are connected in parallel with the base load, and without line impedances separating them. The initially-open circuit breaker closes at $t = 1$ s, introducing a step load and re-opens at $t = 4$ s. Table 7.3 summarises the load at each time period; the system is rated at 120 $V_L$, 25 Hz, as before. Figure 7.4 (a) and Figure 7.4 (b) show the load sharing response of the generators without and with droop controllers respectively.

The droop controllers are developed to allow for proportional load sharing, which means that the per unit active and reactive power output of the SGs are designed

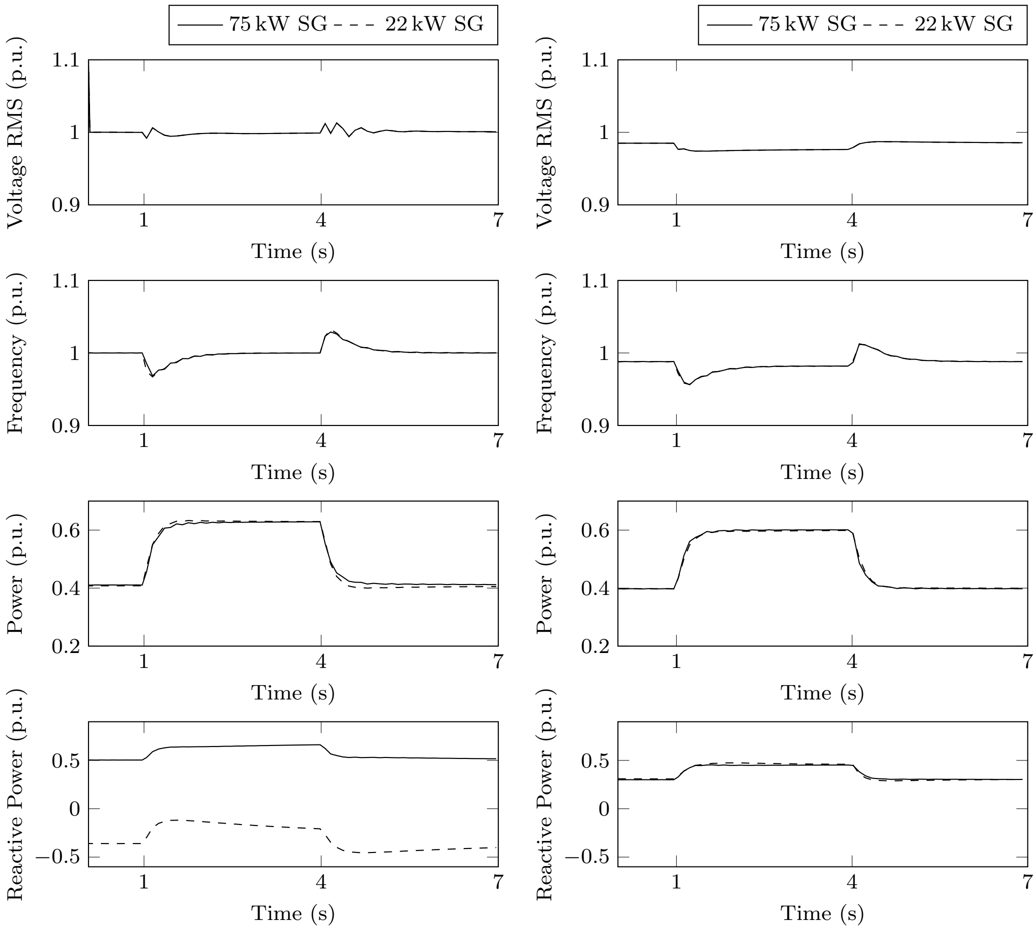


**a.** without droop control. **b.** with droop control.

**Figure 7.4** Load Sharing Tests in Example Microgrid.

to be identical. The output power of both SGs are also tabulated in Table 7.3 for each time period. It is evident that the generators each share 0.4 p.u. of the total load during the time 0 s - 1 s and 4 s - 7 s seconds, and 0.6 p.u. of the total load during the time 1-4 seconds. The steady-state voltage and frequency have deviated from the rated 1 p.u. according to the droop coefficients.

It can be seen in Figure 7.4 (a) that the active power sharing error is small with the absence of Pf-droop. However, the reactive power sharing is poor as there is a large circulating reactive power. The reliability of the system may be compromised with the lack of appropriate local voltage control.

Figure 7.4 (b) shows that with the droop controllers, both the active and reactive power of the SGs have the same per unit output and reach steady-state approximately 0.5 s after the disturbance, without any steady-state error. By implementing the QV-droop controller, the system voltage is regulated and the circulating reactive power is eliminated, ensuring the reliability of the system.

Since the SGs are equipped with only the speed and voltage controller in Figure 7.4 (a), the terminal voltage and frequency are regulated to 1 p.u. each. However, in Figure 7.4 (b), due to the droop characteristics, the voltage and frequency have deviated from the rated values. Based on a 3% speed droop and 5% voltage droop, the voltage and frequency are calculated for each time period and summarised in Table 7.3. This deviation is an inevitable trade-off of the droop controller and its rectification is further discussed in Section 7.5.2.

## 7.3 Effects of Line Impedance on Load Sharing

It was discussed extensively that the reactive power sharing is difficult to control in practice. The formulation of the reactive power sharing error is included in Appendix A, where it is derived mathematically. The analysis concludes with Eq.(7.1), which shows that the reactive power sharing is dependent on ill-defined parameters, such as the voltage at the PCC and the line impedances [47]. This section demonstrates the effect of the resistive line impedance on conventional droop controllers. Once the effect is known, subsequent investigation and possible rectification can be made depending on the severity.

### 7.3.1 Inaccurate Reactive Power Sharing

The set-up of the test cases are as follows: Case 1 includes only the droop controllers, Case 2 includes the droop controllers and an equal length of series line impedance, and Case 3 includes the droop controllers and an unequal length of series line impedance. The results of Case 1, 2, 3 are shown in Figure 7.5 (a), Figure 7.5 (b) and Figure 7.5 (c) respectively.

A 0.25 km LV cable is installed between both SGs and the PCC respectively, where $Z_{TL1} = Z_{TL2} = 0.25 \times (R_{LV} + jX_{LV})$. Comparing Case 1 and Case 2 in Figure 7.5 (a) and Figure 7.5 (b), it is evident that by introducing line impedances between the two generators, the reactive power sharing worsened significantly.

Even though the power cable is of equal length, the voltage drops across the line impedances are unequal due to the difference in currents, affecting the PCC voltage. Since this is not a parameter that is accounted for in the $QV$-droop control, the reactive power sharing is severely affected.

For Case 3, an unequal line impedance exist between each of the two SGs and the PCC. The 75 kW SG is 0.4 km away from the PCC, while the 22 kW SG is 0.1 km away. Therefore, $Z_{TL1} = 0.4 \times (R_{LV} + jX_{LV})$ and $Z_{TL2} = 0.1 \times (R_{LV} + jX_{LV})$

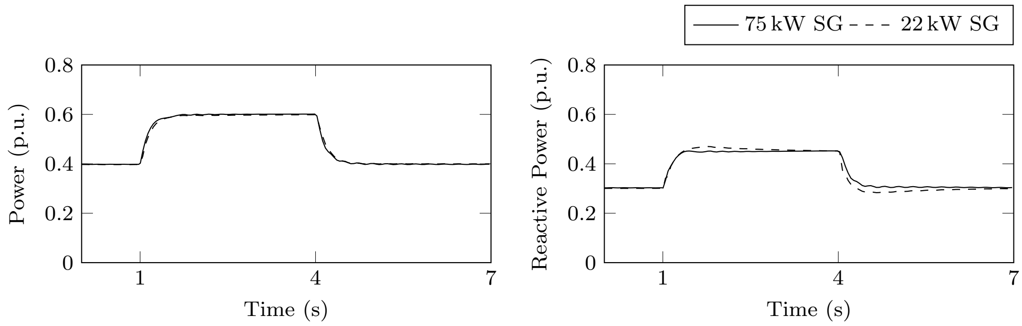


**a.** Case 1: No line impedance.

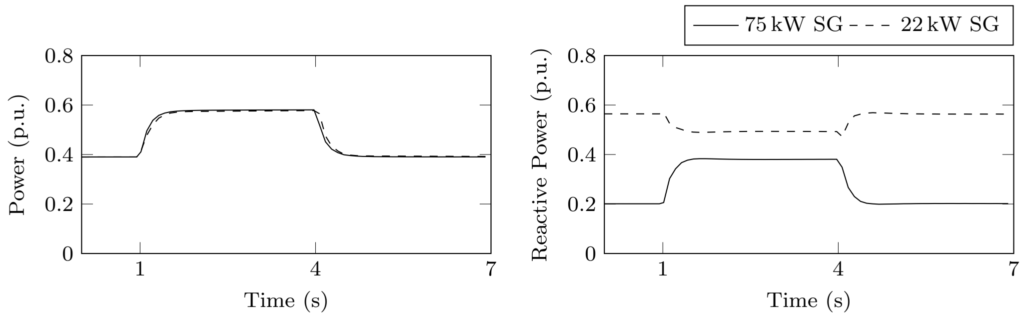


**b.** Case 2: Equal line impedance.

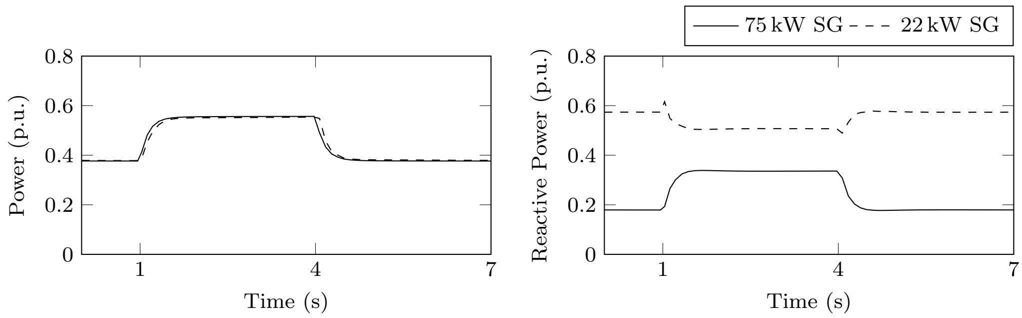


**c.** Case 3: Unequal line impedance.

**Figure 7.5** Comparisons between Cases 1, 2, 3.

Comparing Case 2 and Case 3, it can be seen that the reactive power sharing error worsens when the line impedances are unequal. This clearly shows that the reactive power sharing is severely affected by the resistive line impedance as expected.

### 7.3.2 Active Power and Reactive Power Coupling

According to the conventional droop controller theory as stated in Eq.(2.3) and Eq.(2.6), the active and reactive power are independent of one another. This section demonstrates that the resistive line impedance causes an undesired coupling between the active and reactive power. In order to simplify the analysis, $Z_{TL1}$ is set to be equal to $Z_{TL2}$ for all the cases. In Figure 7.6 (a), Case 4 shows that the active power sharing is not affected by the change in reactive power load, whilst Case 5 and Case 6 demonstrates that the reactive power sharing is affected by the change in active power load. Case 7 repeats Case 6 for medium and high voltage cables, which has a mixed and inductive-dominant line impedance respectively.

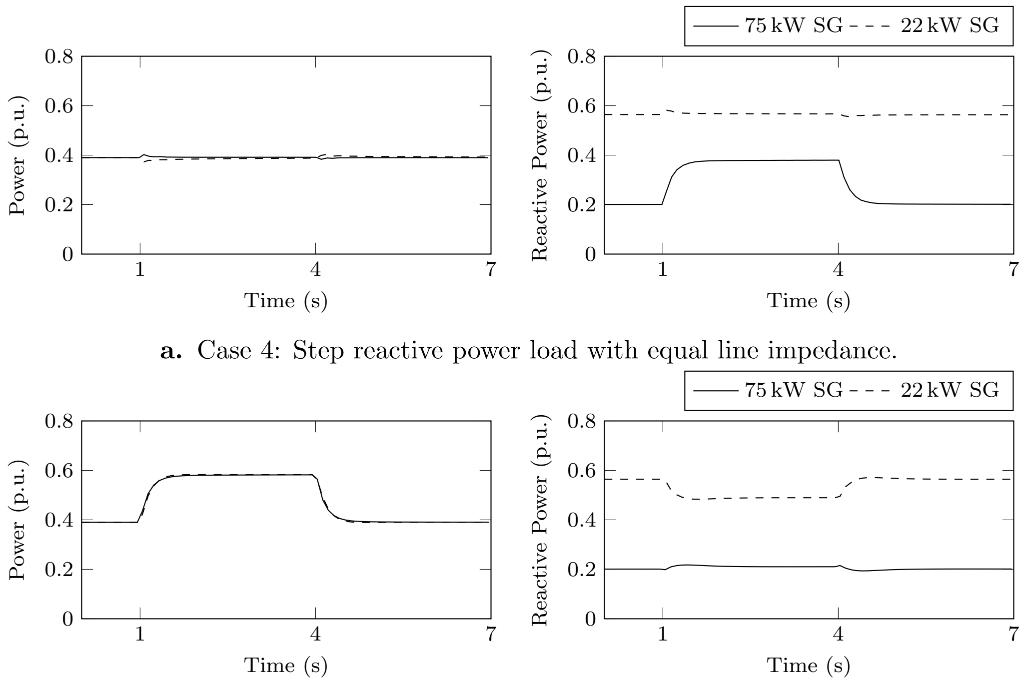


**a.** Case 4: Step reactive power load with equal line impedance.

**b.** Case 5: Step active power load with equal line impedance.

**Figure 7.6** Comparison between Cases 4 and 5.

*Case 4: Change in Reactive Power Step Load*

In Case 4, a 3.65 kVAR step load is introduced by closing the initially-open circuit breaker at $t = 1\,\text{s}$ and opening the circuit breaker again at $t = 4\,\text{s}$. This means that the voltage set-point decreases while the speed set-point remains constant, which, according to Eq.(2.6), results only in the increase of output reactive power of the SGs.

Figure 7.6 (a) shows that this is indeed the case, where the active power sharing is not affected by the change in the total reactive power, and remains constant throughout the simulation with a minor transient response. This is as expected since the active power sharing is only dependent on well-defined parameters, such as the droop coefficient, the power reference and the frequency reference [47]. Since the droop coefficient is a constant, the active power sharing will remain accurate, as long as the references are measured correctly.

The reactive power sharing is still not proportional to the rating of the SGs due to the presence of the line impedance. Figure 7.6 (a) shows that the reactive power is picked up almost entirely by the 75 kW SG.

*Case 5: Change in Active Power Step Load*

In Case 5, a 4.85 kW step load is introduced while the total reactive power load is kept constant. This means that the speed set-point decreases, whilst the voltage set-point remains constant, which according to Eq.(2.3), results in only the output active power of the SGs increasing.

Figure 7.6 (b) shows that even though the total reactive power stays constant throughout the simulation, the sharing is affected by the change in active power. This is because the reactive power sharing is affected by the PCC voltage and the PCC voltage varies with the change in active power [47].

*Case 6: Change in Active Power Load Incrementally*

The active power load is introduced incrementally to the microgrid as seen in Figure 7.7. For this case, a 0.97 kW active power load is introduced to the Example Microgrid at every odd second ($t = 1, 3, ...9s$), whilst the total reactive power load remains constant.

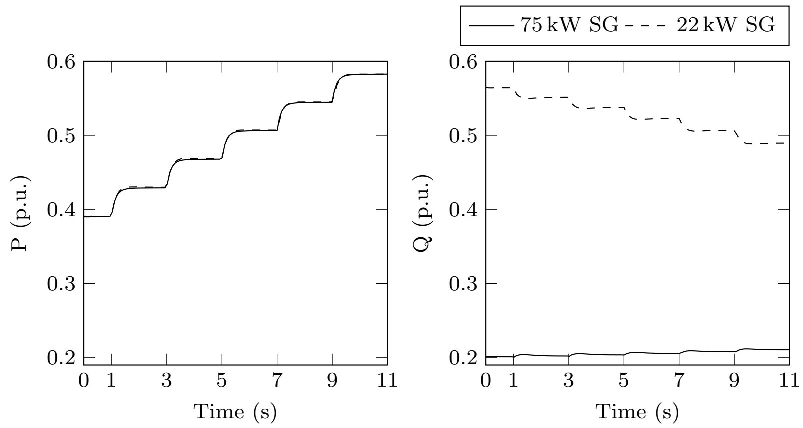


**Figure 7.7** Case 6: Active and reactive power coupling in LV microgrid.

It is observed in Figure 7.7 that the active power increases with a proportional sharing between the two SGs as expected. However, the reactive power sharing changes even though the total reactive power load remains constant. Case 6 demonstrate that this effect is not only present with a large step load, but a minor change in the active power is able to affect the reactive power sharing.

*Case 7: Power Cables at LV, MV, and HV*

Case 7 repeats Case 6 for both MV and HV cables where the active power load is changed incrementally whilst the reactive power load remains constant. This case aims to demonstrate that the undesired power and reactive power coupling does not occur with high voltage cables. The line impedance of the cables are extracted from Table 2.4 and all the cables are set to 2 km long.

Figure 7.8[3] shows the active and reactive power variations of the 75 kW SG with a change in speed, connected to LV, MV and HV transmission lines. Every node in Figure 7.8 represents the steady-state power and reactive power at the specified speeds. The speed, active power and reactive power are recorded just before the step load occurs, i.e. at $t = 1, 3, ... 9$ s as before.

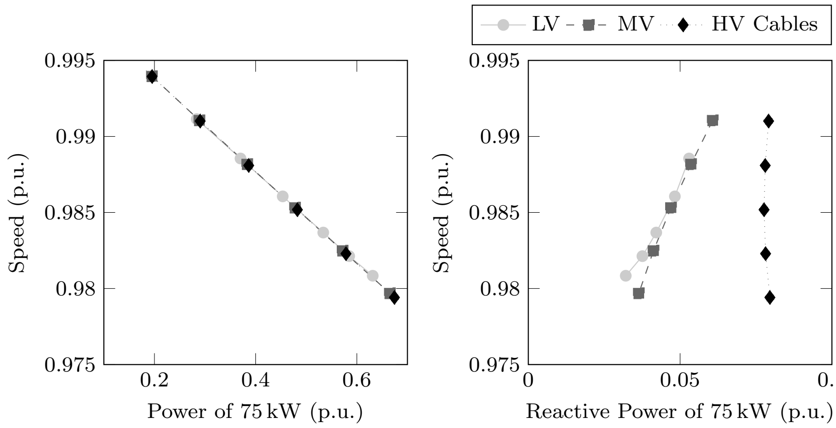


**Figure 7.8** Case 7: Active and reactive power variations under Pf-control with a 2 km LV, MV and HV transmission lines between the SGs.

The active power of all transmission lines adopt the same 3% droop slope as specified. The reactive power of the LV line has the largest variations, whereas the HV line varies the least. This result concurs with the theory discussed in Chapter 2, since the HV line mostly inductive whilst the LV line is mostly resistive.

## 7.4 Parameters that Influence Load Sharing

This work has proved thus far that the low voltage line impedances reduce the efficacy of conventional droop controllers in achieving proportional load sharing between generators. This section aims to identify and investigate the parameters that influence the reactive power sharing accuracy. The aim of this exercise is to determine whether it is possible to predict a maximum allowable distance between two SGs before the controller becomes ineffective. If the maximum allowable distance can be predicted, then it may be possible to only include measures to alleviate the undesirable effects when the DRs are separated by more than the predicted distance.

[3]Note that the reactive power of 75 kW SG connected to LV transmission line is negative, i.e. it is absorbing instead of providing reactive power due to the unequal load sharing. However, the absolute values of the results ($|Q_{75\,kW}|$) are taken for easier comparison.

It was discussed earlier that the reactive power sharing error is dependent on the physical distance between the SGs and the PCC. The PCC voltage is largely influenced by the output voltage at the SG, the voltage drop across the line impedances and the power factor of the load. The output voltage of the SG is a controllable parameter, however, the voltage drop and the power factor are variables that cannot be controlled.

Therefore, three parameters are investigated in this section:

1. The **line impedance** between the SGs represent the physical distance, and is calculated with Eq.(7.5).

$$Z_{TL} = Cable\ Impedance\ [\Omega/km] \times distance\ [km] \tag{7.5}$$

2. The **total load** power ($P_L$) is related to the volt drop across the line impedances, as described by Eq.(7.6) for a pure active power load. The volt drop is proportional to the output power of the SG ($P_i$), and is a constant factor $k$, i.e. the ratio of generator rating to system rating.

$$\begin{aligned} V_{drop} &= \frac{P_i}{3\ V_i} \times Z_{TL} \\ P_i &= kP_L \end{aligned} \tag{7.6}$$

3. The **power factor** is a nonlinear function of the total active and reactive power load as shown in Eq.(7.7).

$$\begin{aligned} PF &= \cos\theta \\ \theta &= \tan^{-1}(\frac{Q_L}{P_L}) \end{aligned} \tag{7.7}$$

Table 7.4 summarises the simulation cases involved to investigate the maximum allowable distance in the Example Microgrid. All the test cases have the speed and voltage regulator with droop control and an equal line impedance between the SGs and the PCC.

The circulating reactive power ($Q_c$) is used as the dependent variable for all the test cases. Due to the nature of the parameters being investigated, the reactive power sharing error is not a suitable metric to determine the performance of the droop controller. For example, Case 9 contains no reactive power load and the reactive power is not constant for Case 10. Therefore, the amount of circulating reactive power, which is simply a form of reactive power sharing error, is used as the indicating metric to quantify the performance of the droop controller.

**Table 7.4** Test cases for identifying the factors which most influence the load sharing between generators.

| Case | Variables | | |
|---|---|---|---|
| | **Dependent** | **Independent** | **Secondary** |
| 9 | $Q_c$ | Distance | Load PF |
| 10 | $Q_c$ | Total P Load | Distance |
| 11 | $Q_c$ | Load PF | Distance |

Due to the inter-dependent nature of the three parameters, a secondary variable is introduced to each case. Since the maximum allowable distance is the focus of the investigation, the simulation for Case 9 and Case 10 are repeated three times for different distances. For Case 8, the simulation is repeated three times with different power factors. The results are illustrated in Figure 7.9. The value of the secondary variable is denoted in the legend.

*Physical Distances on Circulating Reactive Power*

Figure 7.9 (a) shows that as the distances between the SGs increases, the circulating reactive power increases. By comparing the three lines in Figure 7.9 (b) and Figure 7.9 (c), it is also evident that the circulating reactive power is proportional to the separation distance.

*Load Characteristics on Circulating Reactive Power*

The circulating reactive power is also proportional to the active power load, as shown in Figure 7.9 (b). This is because as the active power increases, the voltage drop across the line impedance increases.

For approximately 7.5 kVA of total load, the circulating reactive power decreases with an increase in reactive power load, as illustrated in Figure 7.9 (c). This is observed in Figure 7.9 (a) and Figure 7.9 (b) where the circulating reactive power is worse at lower power factors.

This however, provides little insight into the load sharing performance of the droop controller because the reactive power sharing may still be inaccurate when there is no circulating reactive power. For instance, Case 2 shows inaccurate reactive power sharing without circulating reactive power.

From the analysis, it is clear that the variables are inter-dependent on one another. Although distance is the dominating factor, the maximum allowable distance cannot be predicted since the load is an unpredictable variable at any given time. It is observed in simulation that the system becomes unstable and the voltage collapses

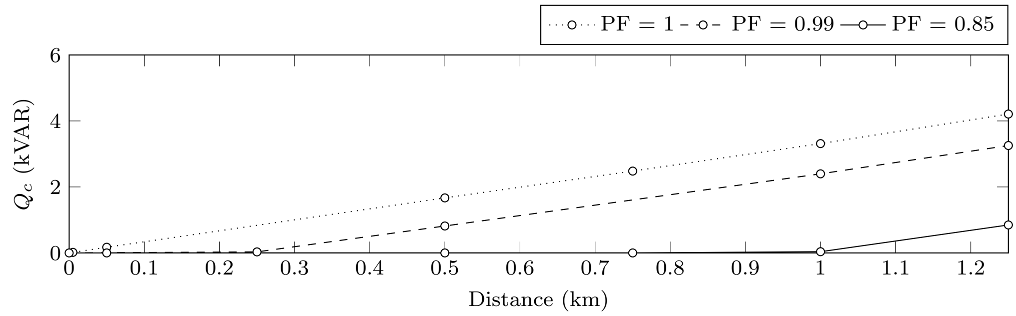


**a.** Case 8: $Q_c$ vs. Distance at different Power Factors.

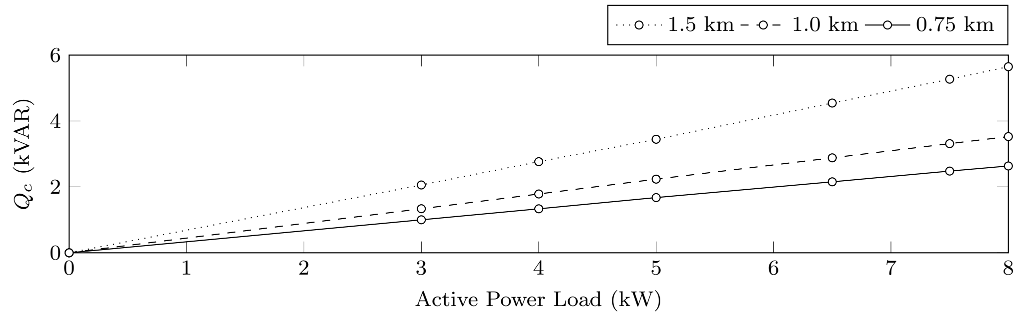


**b.** Case 9: $Q_c$ vs. Total Load at different Distances.

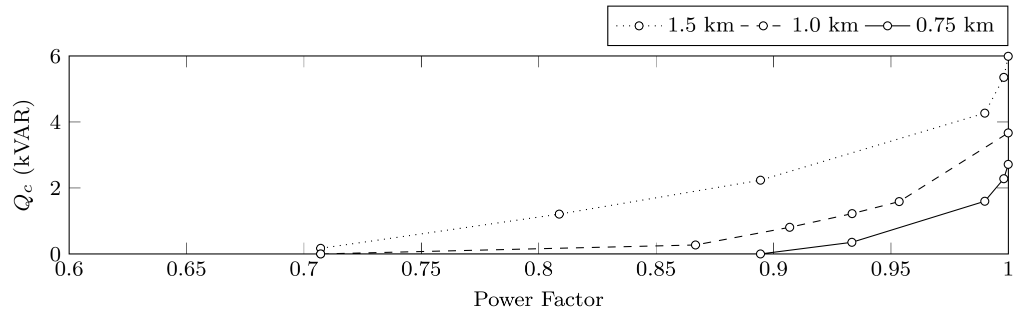


**c.** Case 10: $Q_c$ vs. Power Factor at different Distances.

**Figure 7.9** Investigation based on circulating reactive power.

when the circulating reactive power is approximately 6 kVAR (0.4 p.u. of system rating).

## 7.5 Discussion on System Performance

In an islanded microgrid, the power ratings of the sources are comparable to the loads, so step changes occur frequently and may be detrimental to the system without reliable control and protection. In addition, due to the inherent properties of the droop control, the voltage and frequency deviations are sacrificed to achieve proper load sharing.

### 7.5.1 Stability of the System

In an islanded microgrid, the stability of the power system is critical due to the lack of a swing bus to provide voltage and frequency support [16]. For all the test cases performed in this chapter, the Example Microgrid is deemed stable according to the definition from *Guerrero et al.* [40]:

> *"A steady state can be reached in which the fundamental components of all voltages in the microgrid have constant amplitudes and constant relative phase angle differences."*

The developed QV-droop controller is demonstrated to be effective in preserving the system reliability and stability when the line resistance is small. However, it can be seen from Cases 8 - 10 that the circulating reactive power increases and the efficacy of the QV-droop controller is reduced.

From the results, the system attains marginal stability when the SGs are 40% loaded at $PF = 1$ and 1.5 km apart with LV cables. When the circulating reactive power exceeds approximately 0.4 p.u., the voltage of the Example Microgrid collapses and the system becomes unstable.

It is also shown that high controller gains impact the overall system stability negatively. The controller gains affect the transient stability, while the droop coefficients affect the steady-state stability; however, a poorly tuned controller may cause the system to lose synchronism during a large step load [32]. In addition, a large droop coefficient promises a more proportional load sharing and the system becomes less damped [64].

From the simulation results, it is observed that several factors have a detrimental impact on the system stability. Therefore, in order to ensure the reliability of the system, a stability study should be carried out. The power-flow study is not performed since the Example Microgrid is a simple two-source network. However, the transient and dynamic stability study is required, such as one suggested by *Guerrero et al.* [40].

### 7.5.2 Voltage and Frequency Deviations

It can be seen in Figure 7.4 (b) that there is an inherent trade-off between the voltage and frequency deviations to the reactive power and active power sharing respectively. This deviation cannot be corrected without secondary control, where typically a low bandwidth communication is required to restore the voltage and frequency to its nominal values [18, 20, 23].

Intelligent switches can be installed at the PCC to measure the system voltage and frequency and send set-points to the generators via non-critical low bandwidth communications [18]. This research is focused on primary control, therefore the exploration of secondary control is not carried out. The deviation of voltage and frequency is presented as an observation.

## 7.6 Summary

This chapter reviews the performance of conventional droop controllers within 10 simulation case studies. The Simulink model is similar to the Example Microgrid developed in earlier chapters but the SGs are equipped with conventional Pf- and QV-droop controllers.

It is observed that the resistive-dominant line impedance results in inaccurate reactive power sharing, as well as active and reactive power coupling. Parameters that result in these effects include the physical separation distance between the SGs and the PCC, the total load and the power factor of the load.

The reactive power sharing error is dependent on several uncontrollable parameters, therefore the operating conditions in attaining marginal stability is not unique. This means that the maximum distance allowed between the SGs cannot be predicted based on the study conducted.

The stability of the system depends on several factors. This study focuses on the system stability based on the circulating reactive power; however, other factors such as the controller gains and droop coefficients (discussed in Appendix E) may also have detrimental impacts on the system. A comprehensive stability study is beyond the scope of this research but in order to ensure the reliability of the system, it is recommended as future work.

Up until this point, the secondary aim of the research is achieved by conducting an investigation into the load sharing between DRs in the Example Microgrid. The effects of resistive line impedance on droop controllers is demonstrated, while the parameters that may influence the controller actions are identified. As a possible application of this research, the next chapter uses the knowledge obtained in this chapter to implement and subsequently analyse the performance of three adaptations of droop controllers.

# CHAPTER 8

## Proposed Application: Variations of Droop Controller Designs

This chapter demonstrates a possible application of the work presented thus far. Using the simulation environment developed, different controller designs and strategies are discussed. Three droop control variations are implemented in the Simulink Example Microgrid model, including voltage drop compensation, line impedance compensation and implementing phase shifting transformers. This chapter shows that the simulation environment developed can be used to investigate the system interactions in a complex power system.

### 8.1 Introduction

The challenges faced by conventional droop controllers in a low-voltage islanded microgrid are investigated in Chapter 7. It is demonstrated with several simulation cases that the conventional droop controller is insufficient in achieving proportional load sharing between the generation sources. Adapted and improved droop controller designs in the literature have various degrees of success. This chapter implements and briefly compares three control strategies that aim to improve the accuracy in proportional reactive power sharing.

The majority of the adapted droop controllers in the literature are developed for inverters. These controllers may not be applicable to SGs due to their inherent limitations as rotating machines. For example, the virtual output impedance approach cannot be implemented in a controller for machines without adding extra power electronics. This chapter aims to present possible applications of this research rather than proposing a fully developed control solution. The three control strategies are therefore selected based on their compatibility with rotating machines as well as the simplicity in their derivations.

The control methods are implemented in the simulation environment described in Chapter 7. The three strategies include: the voltage drop compensation method, the line impedance compensation method, and the implementation of a Phase-Shifting Transformer (PST). The specification and requirements of these controllers are first developed based on the IEEE standards for DRs (IEEE 1547 series). The simulation results and analysis are presented for all the methods, where the voltage and frequency regulation as well as the system stability study are subsequently introduced as future work.

## 8.2 Specifications and Requirements

The IEEE Application Guides provide substantial information on the deployment of DRs in an electric power system. This section summarises the standards on the specifications and requirements of the control system that is pertinent to this research, according to IEEE 1547 series. Specific attention is focused on IEEE Std 1547.4-2011, which provides details on the design, operation and integration of DRs in an islanded microgrid.

The DRs in an islanded microgrid are required to actively regulate voltage and frequency within the range specified. In addition, they are required to support the real and reactive load at an acceptable voltage level, such as ±10% of nominal voltage level in South Africa [65] or $0.88 \sim 1.05$ p.u. for the United States [66].

It is recognised in IEEE Std 1547.4-2011 [67] that, in order to maintain the desired voltage profile, the steady-state voltage and frequency for an islanded microgrid can operate outside of the requirements specified by the utility. The voltage and frequency specifications are summarised in Table 8.1 from the IEEE standards.

**Table 8.1** Steady-state IEEE specifications for voltage and frequency ranges.

| Mode | Voltage (p.u.) | Frequency (p.u.) |
|---|---|---|
| **Grid-Connected** | $0.88 \sim 1.1$ | $0.99 \sim 1.01$ |
| **Islanded** | Acceptable Level | Acceptable Level |
| **Standalone** | $0.88 \sim 1.1$ | $0.88 \sim 1.1$ |
| **Proposed** | $0.88 \sim 1.1$ | $0.97 \sim 1.03$ |

For a synchronous generator operating in the standalone mode, the voltage and frequency band is around (±0.1 p.u.). The frequency band for grid-connected mode is very tight (±0.05 Hz), however, for the islanded mode both the voltage and frequency band can be defined according to the type and characteristic of the connected load in the island [67].

The voltage band for the Example Microgrid is proposed to be 0.88 $\sim$ 1.1 p.u. as suggested.

The oscillation of the system voltage and frequency following a major disturbance are to be dampened within 6 s and 2 s respectively for the Example Microgrid. These values are obtained from the recommended guideline in IEEE 1547.4-2011 [67].

It is stated in IEEE Std 1547.4-2011 that a system is stable if the system response is bounded when the system is subjected to a bounded disturbance. In addition, according to the definition from *Guerrero et al.* [40], the stability of the microgrid is achieved when the fundamental components of all voltages have constant amplitudes and constant relative phase angle differences. The stability of the Example Microgrid is determined with the aforementioned definitions, where a visual inspection is performed (see Section 8.5 for details).

## 8.3 Variations of Droop Controller Design

The simulation set-up used to evaluate the controllers is identical to the set-up described in Chapter 7. The Example Microgrid includes two SGs of 22 kW and 75 kW each, a resistive base load and step load, an inductive base load and step load, as well as an equal length of transmission cable to connect the SGs to the PCC. The droop controller is almost identical to the one described earlier, where each subsection below describes a minor adaptation to the droop control to improve the reactive power sharing error.

### 8.3.1 Voltage Drop Compensation

It is discussed previously that the reactive power sharing error is largely due to the difference in volt drops between each DR and the voltage at the PCC. To improve the reactive power sharing error, the reactive power reference is positively biased with the voltage drop between the DR and the PCC voltage as shown in Eq.(8.1). Both $V_{pcc}$ and $V_i$ are the positive sequence component and $t_d$ is the time delay.

$$V_{drop,i}(t) = V_{pcc}(t - t_d) - V_i(t) \tag{8.1}$$

To obtain $V_{drop}$, several authors recommend that the PCC voltage is relayed to each DR through serial communication [44, 47]. Since the droop control is responsible for the steady-state load sharing, a low-bandwidth communication is sufficient. Given the standard network communication speed for RS232, a 100 ms delay is used as a lump sum of the measurement time and communication latency [44].

### 8.3.2 Line Impedance Compensation

With the knowledge of the line impedance, *Engler and Soultanis* [17] propose positively biasing the reactive power reference with an estimated voltage drop. The estimated voltage drop across the line impedance ($V_{line}$) is calculated with positive sequence current ($I_i$) and the line impedance ($R_{TL}+jZ_{TL}$) as shown in Eq.(8.2).

$$V_{line,i} = I_i \times 0.8\,(R_{TL} + jX_{TL}) \tag{8.2}$$

The information required for this method can be obtained locally, however, the accuracy of this method requires the knowledge of the physical line impedance, which is often difficult to obtain. Although the line impedance is rather straight forward to estimate for a two-source grid such as the Example Microgrid, it is difficult to estimate for a larger and more complex power gird. Therefore, in order to ensure stability and not over-compensate for the line impedance [17], a compensation of 80% of the line impedance is used.

### 8.3.3 Phase Shifting Transformer

The active and reactive power sharing is implemented with droop control that assumes an inductive-dominant line impedance. This is not the case for a low-voltage microgrid, which results in a coupling between the active and reactive power control. One way of decoupling the active and reactive power is to install a transformer to increase the line inductance. In addition, with a phase shifting transformer, the phase shift between the DRs can be controlled.

A PST is conventionally used to control the active power flow between two stiff grids by adjusting the phase angle between the voltages at the terminals. As a proof of concept, the PST is applied here to decouple the active and reactive power due to its inductive nature. A standard Simulink block of *zigzag phase shifting transformer* is connected between the 22 kW SG and the PCC. The secondary winding has the same voltage magnitude as the primary, but with a $+25^o$ phase shift from the primary.

## 8.4 Simulation Results and Discussion

Figure 8.1 is the reference case, where no compensation methods are used. It can be seen that the reactive power sharing is poor and the output voltages at the SGs are not compensated for. The voltage quality of the reference case is poor, where the steady-state voltage is 0.925 p.u. for the duration of the step load.

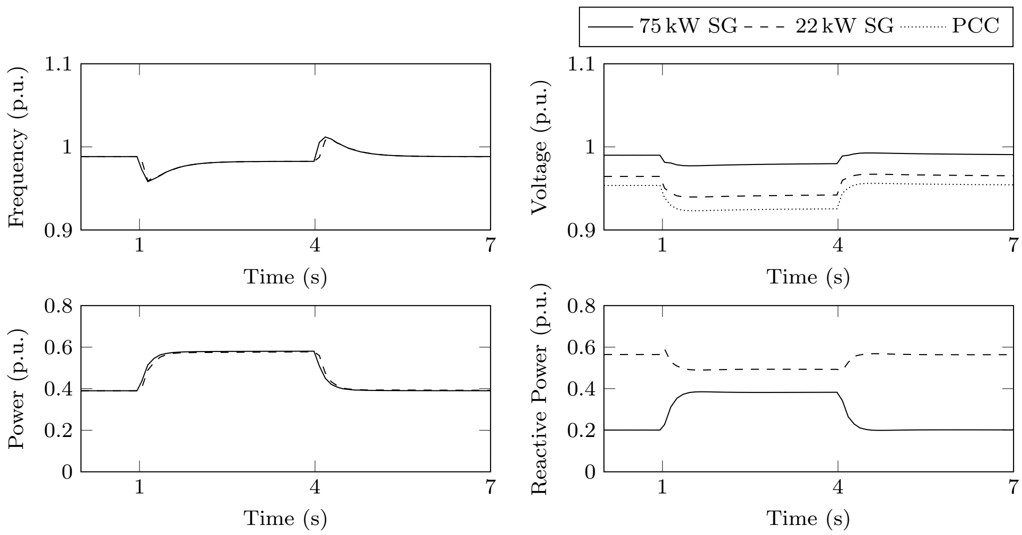


**Figure 8.1** Simulation reference case for Example Microgrid.

### 8.4.1 Voltage Drop Compensation

Figure 8.2 (a), Figure 8.2 (b) and Figure 8.2 (c) present the result of the voltage drop compensation method on the Example Microgrid, with a 20 ms, 100 ms and 150 ms communication delay. It can be seen that the steady-state reactive power sharing is insensitive to the delay. However, since the PCC voltage relayed to the DR is not the instantaneous value, the voltage and frequency oscillation takes longer to dampen with the increase in the communication delay.

For a short communication delay, the frequency and the active power sharing are not affected for both transient and steady-state conditions. Although the system frequency oscillates with the voltage when the delay increases, the accuracy of the active power sharing is preserved in steady-state.

In comparison with the reference case, the output voltages of the SGs are over-excited to above 1 p.u. in order to compensate for the line voltage drop. Table 8.2 records the PCC voltage for the different delay times, where the steady-state voltages are the same with the 20 ms and 100 ms delay. The voltage is slightly lower since it is still oscillating slightly with the 150 ms delay, but the difference is negligible. It can be concluded that with an accurate measurement, this method guarantees that the proportional reactive power sharing is achieved at steady-state.

**Table 8.2** PCC Voltage with different compensation methods

| Method | Period | Voltage (p.u.) | | | Figure |
|---|---|---|---|---|---|
| Conventional | 1 - 4 s | 0.9255 | | | Fig. 8.1 |
| | 4 - 7 s | 0.9543 | | | |
| Voltage Drop | Delay (ms) | 20 ms | 100 ms | 150 ms | Fig. 8.2 |
| | 1 - 4 s | 0.9763 | 0.9763 | 0.9757 | |
| | 4 - 7 s | 0.9857 | 0.9857 | 0.9848 | |
| Line Impedance | $R_s$ (%) | 100% | 80% | 50% | Fig. 8.3 |
| | 1 - 4 s | 0.9900 | 0.9758 | 0.9732 | |
| | 4 - 7 s | 0.9952 | 0.9856 | 0.9740 | |
| PST | Phase shift ($^o$) | $5^o$ | $15^o$ | $25^o$ | Fig. 8.4 |
| | 1 - 4 s | 0.9248 | 0.9226 | 0.9221 | |
| | 4 - 7 s | 0.9507 | 0.9501 | 0.9497 | |

### 8.4.2 Line Impedance Compensation

Figure 8.3 (a) to (c) illustrate the effect of over- (100% of $R_s$), critically (80% of $R_s$), and under-compensation (50% of $R_s$) for the line impedance. With a 50% compensation, it can be seen that although the reactive load sharing error is reduced for the base load, the smaller SG still picks up the majority of the load. For the 100% compensation, the larger SG provides more reactive power, but the error is still large. The most ideal case is with an 80% compensation, which allows for a negligible steady-state error.

The frequency and active power output for both transient and steady-state are insensitive to the line impedance compensation. In addition, similar to the voltage drop compensation method, the line impedance compensation also increases the output voltage of the SGs. However, there is less over- or under-shooting for the voltages compared to the voltage compensation method. Table 8.2 shows the PCC voltage with different $R_s$ compensations, with 80% $R_s$ being the closest to the voltage drop compensation method.

### 8.4.3 Phase Shifting Transformer

Figure 8.4 (a), Figure 8.4 (b), Figure 8.4 (c) show the simulation results of implementing a $0.5^o$, $25^o$ and $50^o$ PST in the Example Microgrid respectively. It can be seen that regardless of the phase shift, the reactive power sharing has all improved without compromising the frequency and the active power sharing.

The PCC voltage is lower than the reference case as shown in Table 8.2. This shows that although the PST is able to improve the reactive power sharing, the voltage quality may be compromised. The decrease in voltage implies that the maximum power that can be transmitted is decreased with the use of a PST.

## 8.5 Discussion and Future Work

The DRs are required to regulate the voltage and frequency in an islanded microgrid as specified in Section 8.2. This section discusses the voltage and frequency regulation as well as stability studies for future work.

### 8.5.1 Frequency and Voltage Regulation

Active frequency regulation is required from the DRs since an islanded microgrid lacks a strong source to act as an infinite bus. The speed droop controller developed allows the generators to respond to the frequency change due to loading and unloading. With all three methods implemented, the frequency is dampened to an acceptable level within the prescribed time ($< 2\,\mathrm{s}$).

The frequency inherently deviates from the nominal due to the droop characteristics. The maximum steady-state deviation is prescribed to be 3%; however, depending on the voltage quality requirement for the islanded microgrid, the system frequency may need to be restored to nominal.

Active voltage regulation is also required from the DRs in order to maintain the voltage quality while supporting both the active and reactive loads. Although the voltage droop control ensures good voltage regulation, the reactive power sharing is not guaranteed.

The voltage has a maximum of 5% deviation due to the droop characteristics. Depending on the voltage quality requirement for the islanded microgrid, this deviation may also need to be restored. In addition to the droop controller, other voltage regulation techniques, such as shunt capacitors, static/dynamic var compensators, static synchronous compensators and synchronous compensators may be required to improve the voltage quality [7].

### 8.5.2 Stability Study

In an islanded microgrid, the dynamic time constants vary greatly between different DRs [7]; therefore, a detailed transient model of the machines and their control are required. A traditional stability study is not performed since it is beyond the scope of this work. However, a visual inspection of the simulation results is performed to confirm the stability of the Example Microgrid. With the stability definition given in Section 8.2, all the cases examined in this chapter are stable since the responses are all bounded.

In order to ensure the reliability of the Example Microgrid, several studies should be performed as future work. The controllers must ensure the system voltage and frequency can be restored within the specified clearing time and remain within the bands for all system swing conditions. In addition, a small-signal stability study should be performed as the analysis takes into account the governor and regulator response.

### 8.5.3 Comparison between the Variations of Droop Control

The PST is a form of Flexible AC Transmission System (FACTS) with a long history in controlling power flow through transmission networks. The PST is reliable; however, the voltage quality is not guaranteed.

The line impedance compensation method is recommended if the voltage and frequency restoration is not required. However, the impedance may change if more DRs are connected to the islanded microgrid. Since the success of this method is heavily reliant on the line impedance parameters estimated, a dynamic line impedance estimation technique may be required. This adds significant complexity to the control strategy especially within a complex power grid.

The voltage drop compensation method is ideal if frequency restoration is required. Since the communication network is implemented to relay the PCC voltage, the frequency set-point can also be biased with the system frequency deviation. With this approach however, the equipment, interfaces and available communication protocols may present challenges and decrease the controllers' robustness.

## 8.6 Conclusion

This chapter demonstrates that the Example Microgrid model developed in Simulink can furthermore be used to analyse control strategies. The voltage drop compensation is the most accurate, but requires a communication network; the line impedance compensation requires the knowledge of the cable characteristics; the PST compromises the voltage quality for improved reactive power sharing. The other solutions discussed in Chapter 2 may be more elegant, however, the three control strategies implemented all allow the SGs to conform to the proposed specifications and requirements.

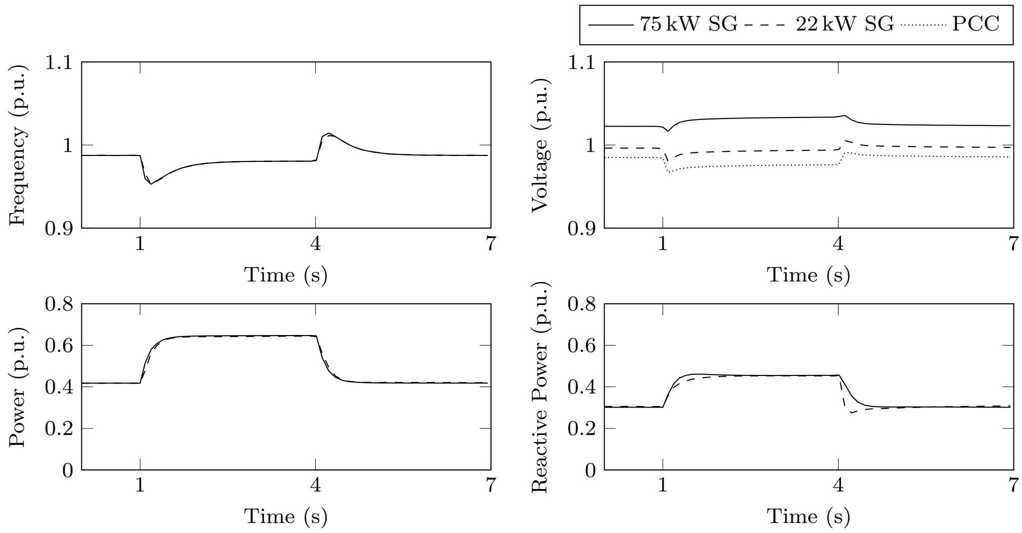


**a.** Communication delay of 20 ms.

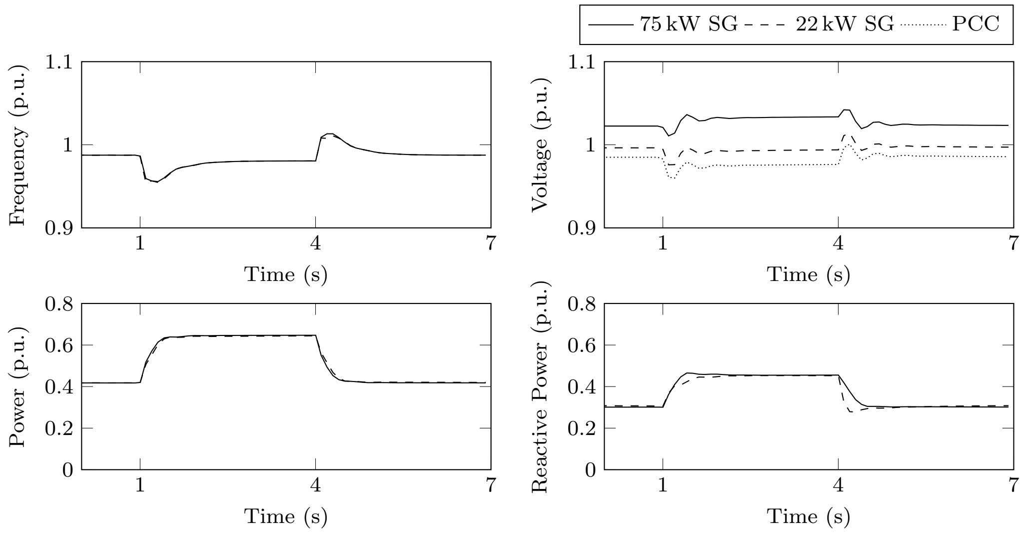


**b.** Communication delay of 100 ms

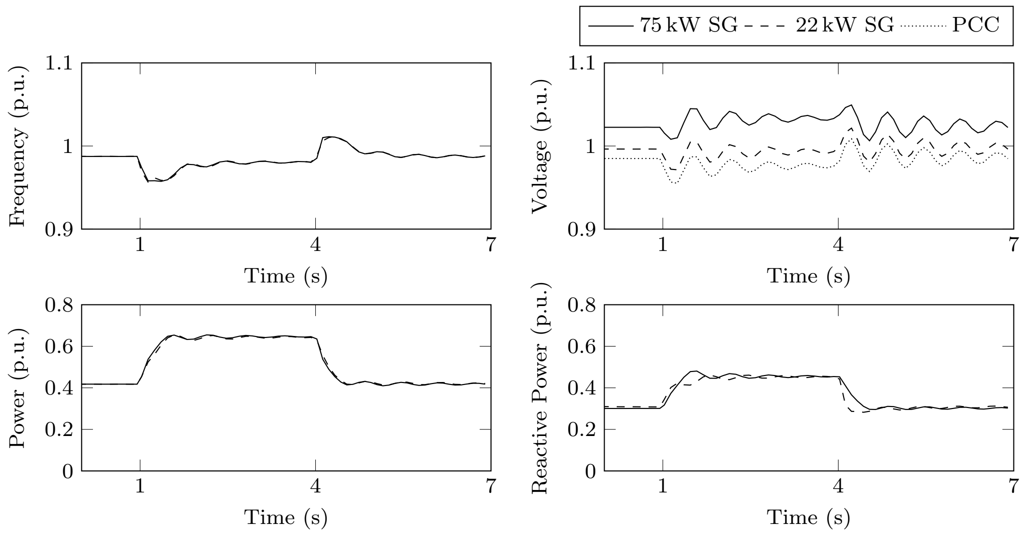


**c.** Communication delay of 150 ms

**Figure 8.2** Controller with Voltage Drop Compensation.

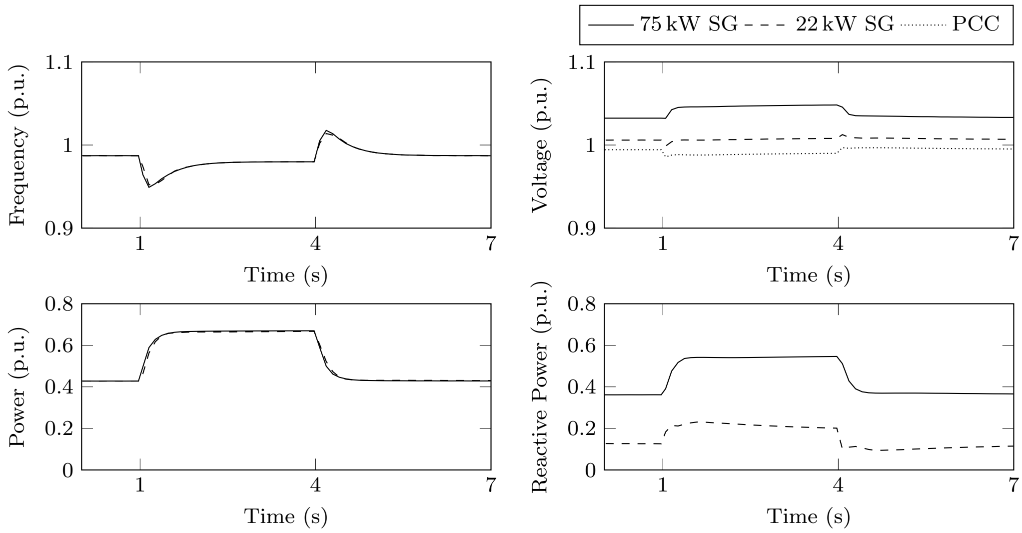


**a.** Over-compensation with 100% $R_s$.

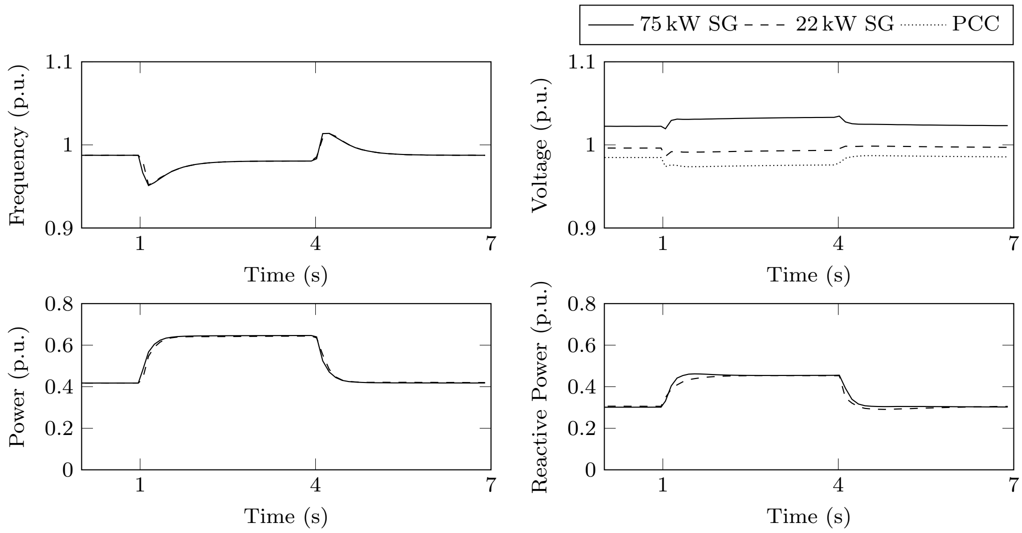


**b.** Critical-compensation With 80% $R_s$.

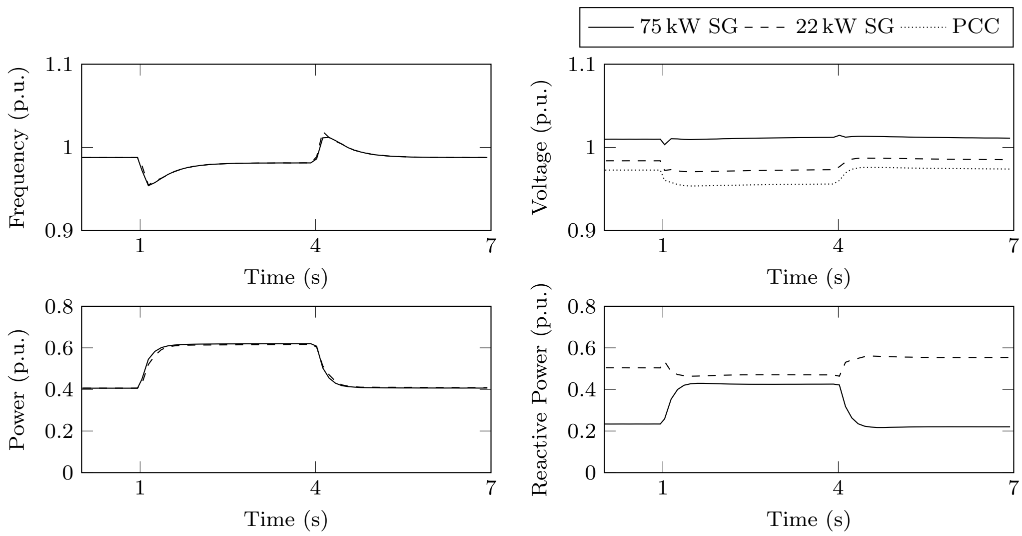


**c.** Under-compensation with 50% $R_s$.

**Figure 8.3** Controller with Line Impedance Compensation.

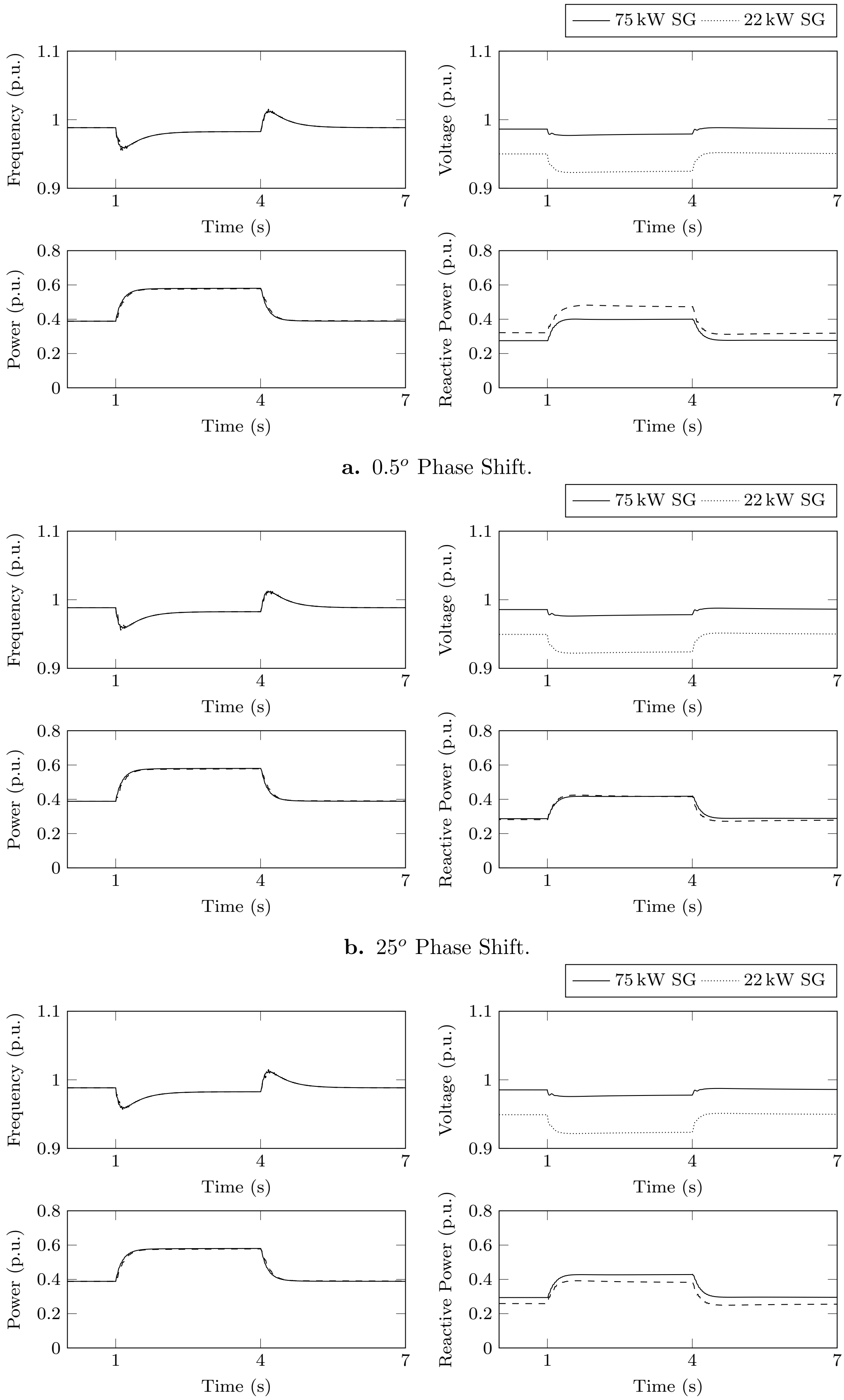


**a.** $0.5^o$ Phase Shift.

**b.** $25^o$ Phase Shift.

**c.** $50^o$ Phase Shift.

**Figure 8.4** Controller with Phase Shifting Transformer.

# CHAPTER 9

## Review and Conclusion

In this chapter, the two main research objectives of this work are evaluated. The simulation environment is validated through corroborating the simulation results with the experimental measurements. The effects of resistive line impedance on load sharing is demonstrated while the parameters that may influence the droop controller actions are identified. Future recommendations in the refinement of the project as well as the possible applications of this work are presented.

### 9.1 Review of Project

Droop control is the most common strategy to achieve a proportional load sharing in islanded microgrids since it only requires local information. Although droop control is robust and reliable in conventional power plants, it is widely recognised that the resistive-dominant line impedances reduce its efficacy in achieving proportional load sharing. Variations of droop control have been proposed with various degrees of success, however, the significance of the effects and the parameters that cause the error in load sharing are rarely discussed.

This aim of this research is twofold. Firstly, an accurate representation of the experimental Example Microgrid is reproduced in Simulink. Secondly, with the confidence gained in the Simulink model, an investigation on load sharing between generators is conducted. As a possible application of this research, control strategies are tested with the Simulink model and their performance evaluated.

The research started with reviewing the state-of-the-art primary control strategies in islanded micrgorids. Based on the common assumptions found in the literature, the problem statement is identified and a distinct set of research objectives are proposed. This section evaluates the deliverables in the context of the entire research.

### 9.1.1 Example Microgrid Model Validation

The Example Microgrid proposed is the simplest form of an islanded microgrid, with two sources, two loads and one power cable. The proposed Example Microgrid allows the investigation to focus on the effects of resistive-line impedance on the active and reactive power load sharing.

The experimental set-up is largely limited by the components available. Based on which, two compromises are made: (1) DFIGs are configured and operated as separately-excited synchronous generators with the rotor excited with DC voltages and (2) A 1.1 Ω resistor is used to represent the line impedance of the power cable. The substituted components maintain the fundamental characteristics that are important for this investigation, therefore it is concluded that the Example Microgrid is successfully implemented.

The simulation set-up is developed to represent the Example Microgrid in the experiment. The components that are directly connected to the PCC are modelled in detail and the auxiliary components such as the variac/rectifier set and the prime movers are treated as known constants.

Experimental tests are performed to estimate the parameters for the SG models. To ensure the validity of the SG models before implementing it in a larger system, the SGs are loaded individually with various resistors under different excitations. The experimental and simulation results are then compared. The results show close correlation with errors below 3% for both machines at different loads and excitations. It is recognised that since the magnetic saturation of the machines is neglected, the model is only valid below the parametrisation voltage, i.e. 120 $V_L$. Since the machines are parametrised at the operating voltage of the Example Microgrid, it is concluded that the SG models are able to represent the physical machines.

After validating the components with individual load tests, the droop and transient tests are conducted to validate the Example Microgrid system model. Although this research focuses on the steady-state load sharing,both transient and steady-state tests are performed to identify the boundaries of the model. Through comparison of the experimental and simulation results, it is concluded that the simplifications made do not degrade the model in steady-state. The Example Microgrid model is deemed to be able to represent the physical system under steady-state operation. However, the transient experimental and simulation results have a poor correlation because the components that are not connected to the PCC are not modelled. This is a permissible simplification since this research aims to investigate the steady-state load sharing only.

Up until this part of the work, it can be seen that the validity of the Simulink model is confirmed at steady-state, under the prescribed operating condition of 120 $V_L$ at 25 Hz. The primary aim of this research is achieved.

### 9.1.2 Load Sharing Investigation

With the confidence gained in the model thus far, the investigation of load sharing in a LV microgrid is conducted. The two effects of resistive line impedance on the droop controllers are demonstrated: the undesirable coupling between the active and reactive power and the increase in reactive power sharing error.

The parameters that influence the reactive power sharing include the line impedance and the PCC voltage. The line impedance is unknown locally and the PCC voltage is difficult to predict since it is a function of the instantaneous load conditions. With the inter-dependent nature of these parameters, the maximum distance allowable between the two generators cannot be predicted conclusively.

As a possible application of this research, three droop controller variants are simulated and briefly discussed. Based on the three controllers implemented, the additional communication-layer although increasing hardware complexity, is the most accurate and reliable in attaining proportional load sharing.

### 9.1.3 Generalisability of the Research

The set-up of the Example Microgrid is largely due to the availability of components, one example of such is the use of DFIGs instead of SGs. DFIGs are used to emulate the output behaviour of synchronous generators, which allows the power-flow at the PCC level to be the same as using conventional synchronous generators.

This research focuses on the power-flow between the generators, where only the active and reactive output of the generators are investigated. Implementing conventional SGs is helpful in removing undesired abnormality in the experiment and conform to the industry standard. However, with the two machines producing the same results at the power flow level during steady-state, the findings of this experiment can be exported to similar Microgrid studies that only concern power flow at the PCC level.

## 9.2 Conclusion

With the confidence of the simulation model developed, this research concludes that parameters that influence load sharing include the PCC voltage, the magnitude and the angle of the adjoining line impedance. The power flow equation cannot be simplified to allow for an independent relationship between the Pf- and QV-droop when the line impedance is resistive-dominant. Therefore, an adaptation to the conventional droop controller is required to allow for a proportional load sharing between the DRs.

With sustainability, robustness, minimal capital and maintenance cost in mind, an islanded microgrid is proposed as a solution to rural electrification. With these opportunities, the considerations for designing robust controllers for islanded microgrids are given as a future development to this research.

## 9.3 Future Work

The Example Microgrid is proposed as a proof-of-concept islanded microgrid. Despite the limitations, it was successful in serving as a two-source grid to fulfil the research aims and objectives. Considerations of improvements are proposed for the future implementation of islanded microgrids rather than to rectify the current Example Microgrid.

### 9.3.1 Improvements to this work

The set-up of the Example Microgrid is largely due to the availability of components, resulting in some arguments to be inferred rather than directly proven. In addition, to reduce computation time and simplify the analysis, components that are not coupled to the PCC are not modelled. This simplification proves to be valid for this research under steady-state, but at the risk of compromising the validity of the model during transient conditions.

Two improvements are proposed as possible extensions to this work:

1. Implementation of both the Pf- and QV-droop controllers in the experiment. Instead of drooping the SGs manually, repeat the tests performed with physical controllers. This allows both transient and steady-state response of the droop action to be examined.

2. Include all the active components in the Simulink model for transient analysis. The prime movers, exciters, and the induction machine load should be parametrised. The passive components such as cables, connectors and measurement devices can be ignored for the purpose of this study.

A Power-Hardware-In-the-Loop (PHIL) simulation is a real time digital simulation platform that allows the hardware under test to be physically connected to a real-life power system [68]. The University recently acquired the Real Time Digital Simulator

(RTDS®), which can be used to not only test the controllers, but allow the SGs to be investigated in a larger power network.

The conventional and different variations of droop control should be implemented and tested on the SG in the laboratory. To allow for rapid prototyping, real time hardware such as dSpace® or RTDS® are recommended.

Other design considerations that are beneficial to closing the gap between laboratory-scale testing and real operating microgrids include: use of actual LV cables to connect the SGs instead of series line impedances, inclusion of PE-based sources, non-linear and unbalanced loads and inclusion of an induction motor load with varying starting and loading conditions.

### 9.3.2 Future Extension of this work

An islanded microgrid is deemed the most feasible solution for rural electrification. Primary control is the foundation of such projects, since the voltage and frequency regulation of the grid depends on the success of primary control.

However, the dynamics of primary control may vary between different DRs. For example, rotating machines have a slow time constant, typically a couple of seconds [69]. Inverters have a very short response time due to the lack of rotating inertia [27]. The inverter-coupled induction generators include both the inverter dynamics and machine dynamics [36].

Due to all the different characteristics, it is observed in the literature that interactions between synchronous generators and inverters introduce many complications, such as poor transient load sharing, a conflict in control strategies as well as having an undesirable impact on system stability [32, 42, 69, 70]. Although this is not explored in this research it must be taken into considerations when designing a microgrid with different forms of generation sources.

This research considers only the parallel operation between voltage sources as it is the conventional and most common type of generation source. Since microgrids typically contain both voltage and current source inverters, it may be an interesting exercise to include current sources in future investigations.

# REFERENCES

[1] S. Krishnamurthy, "On the Modelling and Control of Wound Field Synchronous Machine based Gensets for operation in a Microgrid Environment," Ph.D. dissertation, Electrical and Computer Engineering, 2008.

[2] I. Boldea, *The Electric Generators Handbook*, ser. The electric power engineering series. CRC/Taylor & Francis, 2006.

[3] Y. W. Li and C.-N. Kao, "An Accurate Power Control Strategy for Power-Electronics-Interfaced Distributed Generation Units Operating in a Low-Voltage Multibus Microgrid," *Power Electronics, IEEE Transactions on*, vol. 24, no. 12, pp. 2977–2988, Dec 2009.

[4] J. Fletcher and J. Yang, "Introduction to the Doubly-Fed Induction Generator for Wind Power Applications," *Paths to Sustainable Energy, In Tech*, vol. ISBN: 978-953-307-401-6, pp. InTech, Available from: http://www.intechopen.com/books/paths–to–sustainable–energy/introduction–to–the–doubly–fed–induction–generator–for–wind–power–applications, 2010.

[5] P. Sen, *Principles of Electric Machines and Power Electronics.* Wiley, 1997.

[6] P. Krause, O. Wasynczuk, S. Sudhoff, and I. P. E. Society, *Analysis of Electric Machinery and Drive Systems*, ser. IEEE Press series on power engineering. IEEE Press, 2002. [Online]. Available: https://books.google.co.za/books?id=8m4vAQAAIAAJ

[7] "IEEE Standard for Interconnecting Distributed Resources with Electric Power Systems," *IEEE Std 1547-2003*, pp. 1–28, July 2003.

[8] P. Kundur, N. Balu, and M. Lauby, *Power System Stability and Control*, ser. EPRI power system engineering series. McGraw-Hill, 1994.

[9] R. H. Lasseter, J. H. Eto, B. Schenkman, J. Stevens, H. T. Volkommer, D. Klapp, E. Linton, H. Hurtado, and J. Roy, "CERTS Microgrid Laboratory Test Bed," *IEEE Transactions on Power Delivery*, vol. 26, 01/2011 2011.

[10] H. Farhangi, "The Path of the Smart Grid," *Power and Energy Magazine, IEEE*, vol. 8, no. 1, pp. 18–28, January 2010.

[11] N. Hatziargyriou, H. Asano, R. Iravani, and C. Marnay, "Microgrids," *Power and Energy Magazine, IEEE*, vol. 5, no. 4, pp. 78–94, July 2007.

[12] S. Amin and B. Wollenberg, "Toward a Smart Grid: Power Delivery for the 21st Century," *Power and Energy Magazine, IEEE*, vol. 3, no. 5, pp. 34–41, Sept 2005.

[13] A. Ipakchi and F. Albuyeh, "Grid of the Future," *Power and Energy Magazine, IEEE*, vol. 7, no. 2, pp. 52–62, March 2009.

[14] F. Katiraei, R. Iravani, N. Hatziargyriou, and A. Dimeas, "Microgrids Management," *Power and Energy Magazine, IEEE*, vol. 6, no. 3, pp. 54–65, May 2008.

[15] J. Peas Lopes, C. Moreira, and A. Madureira, "Defining Control Strategies for MicroGrids Islanded Operation," *Power Systems, IEEE Transactions on*, vol. 21, no. 2, pp. 916–924, May 2006.

[16] B. Kroposki, R. Lasseter, T. Ise, S. Morozumi, S. Papatlianassiou, and N. Hatziargyriou, "Making Microgrids Work," *Power and Energy Magazine, IEEE*, vol. 6, no. 3, pp. 40–53, May 2008.

[17] A. Engler and N. Soultanis, "Droop control in LV-grids," in *Future Power Systems, 2005 International Conference on*, Nov 2005, pp. 6 pp.–6.

[18] J. Guerrero, J. Vasquez, J. Matas, L. de Vicua, and M. Castilla, "Hierarchical Control of Droop-Controlled AC and DC MicrogridsA General Approach Toward Standardization," *Industrial Electronics, IEEE Transactions on*, no. 1, pp. 158–172, Jan 2011.

[19] J. Guerrero, J. Vasquez, J. Matas, M. Castilla, and L. de Vicuna, "Control Strategy for Flexible Microgrid Based on Parallel Line-Interactive UPS Systems," *Industrial Electronics, IEEE Transactions on*, vol. 56, no. 3, pp. 726–736, March 2009.

[20] J.-Y. Kim, J.-H. Jeon, S.-K. Kim, C. Cho, J.-H. Park, H.-M. Kim, and K.-Y. Nam, "Cooperative Control Strategy of Energy Storage System and Microsources for Stabilizing the Microgrid during Islanded Operation," *Power Electronics, IEEE Transactions on*, vol. 25, no. 12, pp. 3037–3048, Dec 2010.

[21] R. Majumder, A. Ghosh, G. Ledwich, and F. Zare, "Power Management and Power Flow Control With Back-to-Back Converters in a Utility Connected Microgrid," *Power Systems, IEEE Transactions on*, vol. 25, no. 2, pp. 821–834, May 2010.

[22] S.-J. Ahn, J. woo Park, I.-Y. Chung, S.-I. Moon, S. hee Kang, and S.-R. Nam, "Power-Sharing Method of Multiple Distributed Generators Considering Control Modes and Configurations of a Microgrid," *Power Delivery, IEEE Transactions on*, vol. 25, no. 3, pp. 2007–2016, July 2010.

[23] J. Kim, J. Guerrero, P. Rodriguez, R. Teodorescu, and K. Nam, "Mode Adaptive Droop Control With Virtual Output Impedances for an Inverter-Based Flexible AC Microgrid," *Power Electronics, IEEE Transactions on*, vol. 26, no. 3, pp. 689–701, March 2011.

[24] R. Majumder, A. Ghosh, G. Ledwich, and F. Zare, "Load Sharing and Power Quality Enhanced Operation of a Distributed Microgrid," *Renewable Power Generation, IET*, vol. 3, no. 2, pp. 109–119, June 2009.

[25] T. Vandoorn, B. Meersman, L. Degroote, B. Renders, and L. Vandevelde, "A Control Strategy for Islanded Microgrids With DC-Link Voltage Control," *Power Delivery, IEEE Transactions on*, vol. 26, no. 2, pp. 703–713, April 2011.

[26] H. Laaksonen, P. Saari, and R. Komulainen, "Voltage and Frequency Control of Inverter Based Weak LV Network Microgrid," in *Future Power Systems, 2005 International Conference on*, Nov 2005, pp. 6 pp.–6.

[27] B. Kroposki, C. Pink, R. DeBlasio, H. Thomas, M. Simes, and P. Sen, "Benefits of Power Electronic Interfaces for Distributed Energy Systems," *Energy Conversion, IEEE Transactions on*, vol. 25, no. 3, pp. 901–908, Sept 2010.

[28] C. Schauder, ""Advanced Inverter Technology for High Penetration Levels of PV Generation in Distribution Systems"," NREL, Boston, Massachusetts, Tech. Rep., 2014.

[29] A. Paquette, "Powr Quality and Inverter-Generator Interactions in Microgrids," Ph.D. dissertation, University of Wisconsin Madison, 2014.

[30] G. Delille, B. Francois, and G. Malarange, "Dynamic Frequency Control Support by Energy Storage to Reduce the Impact of Wind and Solar Generation on Isolated Power System's Inertia," *Sustainable Energy, IEEE Transactions on*, vol. 3, no. 4, pp. 931–939, Oct 2012.

[31] Q.-C. Zhong and G. Weiss, "Synchronverters: Inverters That Mimic Synchronous Generators," *Industrial Electronics, IEEE Transactions on*, vol. 58, no. 4, pp. 1259–1267, April 2011.

[32] A. Paquette, M. Reno, R. Harley, and D. Divan, "Transient load sharing between inverters and synchronous generators in islanded microgrids," in *Energy Conversion Congress and Exposition (ECCE), 2012 IEEE*, Sept 2012, pp. 2735–2742.

[33] ——, "Sharing Transient Loads : Causes of Unequal Transient Load Sharing in Islanded Microgrid Operation," *Industry Applications Magazine, IEEE*, vol. 20, no. 2, pp. 23–34, March 2014.

[34] M. Arani and Y.-R. Mohamed, "Analysis and Impacts of Implementing Droop Control in DFIG-Based Wind Turbines on Microgrid/Weak-Grid Stability," *Power Systems, IEEE Transactions on*, vol. PP, no. 99, pp. 1–12, 2014.

[35] M. Shahabi, M.-R. Haghifam, M. Mohamadian, and S. Nabavi-Niaki, "Dynamic Behavior Improvement in a Microgrid with Multiple DG Units using a Power Sharing Approach," in *PowerTech, 2009 IEEE Bucharest*, June 2009, pp. 1–8.

[36] F. Bhuiyan and A. Yazdani, "Multimode Control of a DFIG-Based Wind-Power Unit for Remote Applications," *Power Delivery, IEEE Transactions on*, vol. 24, no. 4, pp. 2079–2089, Oct 2009.

[37] U. Bakshi and V. Bakshi, *Synchronous Machines.* Technical Publications, 2009.

[38] R. Lasseter, "MicroGrids," in *Power Engineering Society Winter Meeting, 2002. IEEE*, vol. 1, 2002, pp. 305–308 vol.1.

[39] R. Burns, *Advanced Control Engineering.* Elsevier Science, 2001.

[40] J. Guerrero, M. Chandorkar, T. Lee, and P. Loh, "Advanced Control Architectures for Intelligent Microgrids; Part I: Decentralized and Hierarchical Control," *Industrial Electronics, IEEE Transactions on*, vol. 60, no. 4, pp. 1254–1262, April 2013.

[41] R. Majumder, G. Ledwich, A. Ghosh, S. Chakrabarti, and F. Zare, "Droop Control of Converter-Interfaced Microsources in Rural Distributed Generation," *Power Delivery, IEEE Transactions on*, vol. 25, no. 4, pp. 2768–2778, Oct 2010.

[42] T. Vandoorn, B. Meersman, J. De Kooning, and L. Vandevelde, "Directly-Coupled Synchronous Generators With Converter Behavior in Islanded Microgrids," *Power Systems, IEEE Transactions on*, vol. 27, no. 3, pp. 1395–1406, Aug 2012.

[43] W. Yao, M. Chen, J. Matas, J. Guerrero, and Z. ming Qian, "Design and Analysis of the Droop Control Method for Parallel Inverters Considering the Impact of the Complex Impedance on the Power Sharing," *Industrial Electronics, IEEE Transactions on*, vol. 58, no. 2, pp. 576–588, Feb 2011.

[44] H. Han, Y. Liu, Y. Sun, M. Su, and J. Guerrero, "An Improved Droop Control Strategy for Reactive Power Sharing in Islanded Microgrid," *Power Electronics, IEEE Transactions on*, vol. 30, no. 6, pp. 3133–3141, June 2015.

[45] M. Chandorkar, D. Divan, and R. Adapa, "Control of Parallel Connected Inverters in Standalone AC Supply Systems," *Industry Applications, IEEE Transactions on*, vol. 29, no. 1, pp. 136–143, Jan 1993.

[46] J. Guerrero, L. Garcia De Vicuna, J. Matas, M. Castilla, and J. Miret, "Output Impedance Design of Parallel-Connected UPS Inverters With Wireless Load-Sharing Control," *Industrial Electronics, IEEE Transactions on*, vol. 52, no. 4, pp. 1126–1135, Aug 2005.

[47] H. Gu, X. Guo, and W. Wu, "Accurate power sharing control for inverter-dominated autonomous microgrid," in *Power Electronics and Motion Control Conference (IPEMC), 2012 7th International*, vol. 1, June 2012, pp. 368–372.

[48] J. He and Y. W. Li, "An Enhanced Microgrid Load Demand Sharing Strategy," *Power Electronics, IEEE Transactions on*, vol. 27, no. 9, pp. 3984–3995, Sept 2012.

[49] Q.-C. Zhong, "Robust Droop Controller for Accurate Proportional Load Sharing Among Inverters Operated in Parallel," *Industrial Electronics, IEEE Transactions on*, vol. 60, no. 4, pp. 1281–1290, April 2013.

[50] K. De Brabandere, "Voltage and Frequency Droop Control in Low Voltage Grids by Distributed Generators with Inverter Front-End," Ph.D. dissertation, University of Leuven, 2006.

[51] A. Timbus, P. Rodriguez, R. Teodorescu, and M. Ciobotaru, "Line Impedance Estimation Using Active and Reactive Power Variations," in *Power Electronics Specialists Conference, 2007. PESC 2007. IEEE*, June 2007, pp. 1273–1279.

[52] K. De Brabandere, B. Bolsens, J. Van den Keybus, A. Woyte, J. Driesen, and R. Belmans, "A Voltage and Frequency Droop Control Method for Parallel Inverters," *Power Electronics, IEEE Transactions on*, vol. 22, no. 4, pp. 1107–1115, July 2007.

[53] A. Tuladhar, H. Jin, T. Unger, and K. Mauch, "Control of Parallel Inverters in Distributed AC Power Systems with Consideration of Line Impedance Effect," *Industry Applications, IEEE Transactions on*, vol. 36, no. 1, pp. 131–138, Jan 2000.

[54] W. A. Cronje, I. W. Hofsajer, M. Shuma-Iwisi, and J. I. Braid, "Design Considerations for Rural Modular Microgrids," in *Energy Conference and Exhibition (ENERGYCON), 2012 IEEE International*, Sept 2012, pp. 743–748.

[55] J. Glover, M. Sarma, and T. Overbye, *Power System Analysis and Design.* Cengage Learning, 2011.

[56] MATLAB, *version 8.2.0.701 (R2013b)*. Natick, Massachusetts: The MathWorks Inc., 2013.

[57] Mathworks, "SimPowerSystems Users Guide (Second Generation) (R2013b)," 2013.

[58] ——, "Simscape Users Guide (R2013b)," 2013.

[59] ——, "Simulink Users Guide (R2013b)," 2013.

[60] C. Ong, *Dynamic Simulation of Electric Machinery: Using MATLAB/SIMULINK*. Prentice Hall PTR, 1998.

[61] R. McMahon, P. Roberts, X. Wang, and P. Tavner, "Performance of BDFM as Generator and Motor," *Electric Power Applications, IEE Proceedings -*, vol. 153, no. 2, pp. 289–299, March 2006.

[62] J. Blackburn and T. Domin, *Protective Relaying: Principles and Applications, Third Edition*, ser. Power Engineering (Willis). CRC Press, 2006.

[63] S.-K. Chung, "A Phase Ttracking System for Three Phase Utility Interface Inverters," *Power Electronics, IEEE Transactions on*, vol. 15, no. 3, pp. 431–438, May 2000.

[64] Z. W. Wenhua Liu, Renjie Ding, "Integrated Optimal Control of Speed, Excitation and Load Sharing of Parallel Operating Diesel Generator Sets," in *Advances in Power System Control, Operation and Management, 1993. APSCOM-93., 2nd International Conference on*, Dec 1993, pp. 142–146 vol.1.

[65] "Electricity distribution Guidelines for the provision of electricity distribution networks in residential areas. Part 1: Planning and design of distribution networks," *SANS 507-1:2007*, pp. 1–95, July 2007.

[66] "American National Standard For Electric Power Systems and Equipment - Voltage Ratings (60 Hertz)," *ANSI C84.1-2011*, pp. 1–13, July 2011.

[67] "IEEE Guide for Design, Operation, and Integration of Distributed Resource Island Systems with Electric Power Systems," *IEEE Std 1547.4-2003*, pp. 1–54, July 2011.

[68] P. Kotsampopoulos, A. Kapetanaki, G. Messinis, V. Kleftakis, and N. Hatziargyriou, "A Power Hardware in the Loop Facility for Microgrids," *International Journal of Distributed Energy Resources, Technology & Science Publishers*, vol. 9, p. 89104, 2013.

[69] S. Krishnamurthy, T. Jahns, and R. Lasseter, "The Operation of Diesel Gensets in a CERTS Microgrids," in *Power and Energy Society General Meeting - Con-*

*version and Delivery of Electrical Energy in the 21st Century, 2008 IEEE*, July 2008, pp. 1–8.

[70] Z. Miao, A. Domijan, and L. Fan, “Investigation of Microgrids With Both Inverter Interfaced and Direct AC-Connected Distributed Energy Resources,” *Power Delivery, IEEE Transactions on*, vol. 26, no. 3, pp. 1634–1642, July 2011.

[71] C. Rowe, T. Summers, R. Betz, D. Cornforth, and T. Moore, “Arctan Power-Frequency Droop for Improved Microgrid Stability,” *Power Electronics, IEEE Transactions on*, no. 8, pp. 3747–3759, Aug.

[72] G. Abad, J. López, M. Rodríguez, L. Marroyo, and G. Iwanski, *Doubly Fed Induction Machine: Modeling and Control for Wind Energy Generation*, ser. IEEE Press Series on Power Engineering. Wiley, 2011. [Online]. Available: https://books.google.co.za/books?id=JzvjOp8pY8QC

[73] I. Ilina, “experimental determination of moment to inertia and me- chanical losses vs. speed, in electrical machines,” in *Advanced Topics in Electrical Engineering (ATEE), 7th International Symposium on*, 2011, p. pp.14.

[74] “IEEE Guide for Test Procedures for Synchronous Machines; Part I: Acceptance and Performance Testing Part IITest Procedures and Parameter Determination for Dynamic Analysis,” *IEEE Std 115-2009 (Revision of IEEE Std 115-1995)*, pp. 1–219, May 2010.

# APPENDIX A

## Additional Background

This appendix includes additional information related to this research to supplement the background provided in Chapter 2. A summary of the assumptions discussed in Section 2.2 are included. Two methods of analysing the reactive power sharing error are mathematically derived. The formulation of the transformation that decouples the active and reactive power in low-voltage microgrids is also included.

### A.1 Summary of Assumptions from the 10 Most cited IEEE Papers

Table A.1 summarises the relevant assumptions in the islanded microgrid field according to the ten most cited papers. The paper is denoted with a "v" if it adopts the assumption, "x" if it does not adopt the assumption and "?" if it is unclear. The topic numbers of Table A.1 are as follows:

| | | | |
|---|---|---|---|
| 1 | Seamless islanding | 11 | VSI-based |
| 2 | LV Microgrid | 12 | Unequal reactive power |
| 3 | Normally connected to MV grid | 13 | No communication for primary control, but communication for secondary control |
| 4 | Inverter-based | | |
| 5 | No controllable SG | 14 | PE has ride through capability |
| 6 | Droop control | 15 | Oversizing PE |
| 7 | Load shedding | 16 | Assumes balanced three-phase |
| 8 | Hierarchical control | 17 | Constant impedance and motor loads |
| 9 | Storage is present | 18 | Includes frequency restoration |
| 10 | Simplified inverter model | 19 | Unproportional load sharing due to $R_T L$ |

**Table A.1** Summary of most cited papers in the field of Islanded Microgrid.

| Topic No. | [15] | [19] | [20] | [21] | [22] | [23] | [24] | [25] | [26] | [3] | v | ? | x |
|---|---|---|---|---|---|---|---|---|---|---|---|---|---|
| 1 | v | v | v | v | v | v | v | v | v | v | 10 | - | - |
| 2 | v | v | v | v | x | ? | v | v | v | v | 8 | 1 | 1 |
| 3 | v | ? | ? | ? | v | ? | v | ? | ? | v | 4 | 6 | - |
| 4 | v | v | x | v | v | v | v | v | v | v | 9 | 0 | 1 |
| 5 | v | ? | x | v | v | v | v | v | v | v | 8 | 1 | 1 |
| 6 | v | v | v | v | v | v | v | v | v | v | 10 | - | - |
| 7 | v | ? | x | ? | ? | x | v | ? | ? | ? | 2 | 6 | 2 |
| 8 | v | v | v | ? | ? | v | ? | ? | ? | ? | 2 | 6 | 2 |
| 9 | v | v | v | v | v | ? | v | ? | v | ? | 7 | 3 | - |
| 10 | v | ? | ? | ? | ? | ? | v | ? | ? | v | 3 | 7 | - |
| 11 | v | v | v | v | v | v | v | v | v | v | 10 | - | - |
| 12 | v | x | ? | x | x | x | ? | ? | ? | v | 2 | 4 | 4 |
| 13 | v | v | x | x | x | x | v | v | v | x | 5 | - | 5 |
| 14 | v | ? | ? | ? | ? | ? | ? | ? | v | ? | 2 | 8 | - |
| 15 | v | ? | ? | ? | ? | ? | ? | ? | ? | ? | 1 | 9 | - |
| 16 | v | v | v | v | v | v | v | v | v | v | 10 | - | - |
| 17 | v | v | v | v | v | v | v | v | v | v | 10 | - | - |
| 18 | v | x | v | v | v | x | x | ? | ? | ? | 4 | 3 | 3 |
| 19 | v | x | ? | x | x | v | v | ? | x | v | 4 | 2 | 4 |

## A.2 Reactive Power Sharing Error Analysis

This section mathematically derives the reactive power sharing error. The first method is obtained from *Gu et al.* [47] and the second method is developed by the author based on the work of *Han et al.* [44].

### A.2.1 Reactive Power Sharing Error based on Transfer Function

Substituting the generator output active and reactive power described in Eq.2.1 into the droop equation Eq.(2.3) and Eq.(2.6). This allows the transfer function of the power and reactive power droop control to be obtained as Eq.(A.1) and Eq.(A.2) [47]:

$$P_i(s) = \frac{m_i X_i E_i V}{s(R_i^2 + X)i^2) + m_i X_i E_i V} \, P_i^*(s) + \frac{X_i E_i V}{s(R_i^2 + X_i^2) + m_i X_i E_i V} \, \omega_i^*(s) + \frac{(R_i E_i^2 - R_i E_i V)s}{s(R_i^2 + X_i^2) + m_i X_i E_i V} \tag{A.1}$$

$$
\begin{aligned}
Q_i(s) = & \frac{n_i X_i(E_i - V)}{R_i^2 + X_i^2 + n_i X_i(E_i - V)} \; Q_i^*(s) \\
& + \frac{XI - (E_i - V)}{R_i^2 + X_i^2 + n_i X_i(E_i - V)} \; E_i^*(s) + \frac{R_i E_i V \phi_i}{R_i^2 + X_i^2 + n_i X_i(E_i - V)}
\end{aligned} \tag{A.2}
$$

The steady-state power is constant in three-phase balanced systems and $s = j\omega = 0$, therefore Eq.A.1 can be reduced to Eq.(A.3) [47]:

$$
P_i(s) = P_i^*(s) + \frac{1}{m}\omega_i^*(s) \tag{A.3}
$$

It can be easily deduced that the active power of the $i^{th}$ generator is dependent only on well-defined parameters: its active power reference ($P_i^*$), angular frequency ($\omega_i^*$) and the droop coefficient ($m_i$). This means that by setting these three parameters appropriately, an active power load sharing can be achieved. However, the reactive power cannot be reduced to a simpler form as shown in Eq.(A.4) [47]:

$$
\begin{aligned}
Q_i(s) = & \frac{n_i}{\frac{R_i^2 + X_i^2}{X_i(E_i - V)} + n_i} \; Q_i^*(s) \\
& + \frac{1}{\frac{R_i^2 + X_i^2}{X_i(E_i - V)} + n_i} E_i^*(s) + \frac{R_i E_i V \phi_i}{R_i^2 + X_i^2 + n_i X_i(E_i - V)}
\end{aligned} \tag{A.4}
$$

The reactive power is dependent on not only its well-defined parameters, $Q_i^*, E_i, n_i$, but also on variables such as the voltage at the PCC ($V_{pcc}$) and the line impedance ($R + jX$) [44, 47].

### A.2.2 Reactive Power Sharing Error for a Two-Source Microgrid

The derivation in this section is performed by the author based on the work of *Han et al.* [44]. This derivation assumes a microgrid with only two sources, having unequal feeder impedances, $X_1 \neq X_2$. To minimise the number of variables for the analysis, the following simplifications are adopted:

1. $m_1 = m_2$: The two sources have equal power rating, hence equal droop coefficients.
2. $Q_1^* = Q_2^* = 0$: The dispatched initial reactive power is zero.

With this in mind, according to Eq.(2.6), the two reactive power and droop equations can be simplified into:

$$
\begin{aligned}
Q_1 &= \frac{V_{pcc}}{X_1}(V_1 - V_{pcc}) \\
Q_2 &= \frac{V_{pcc}}{X_2}(V_2 - V_{pcc})
\end{aligned} \tag{A.5}
$$

$$
\begin{aligned}
V_1 &= V^* + m_{Q_1} Q_1 \\
V_2 &= V^* + m_{Q_1} Q_2
\end{aligned} \tag{A.6}
$$

By combining the above equations, the reactive power output becomes:

$$
\begin{aligned}
Q_1 &= \frac{V_{pcc}(V^* - V_{pcc})}{X_1 - V_{pcc} m_1} \\
Q_2 &= \frac{V_{pcc}(V^* - V_{pcc})}{X_2 - V_{pcc} m_1}
\end{aligned} \tag{A.7}
$$

The reactive power sharing error is therefore:

$$
\begin{aligned}
& Q_1 - Q_2 \\
&= \frac{(V_{pcc}V^* - V_{pcc}^2)(X_2 - V_{pcc}m_1) - (V_{pcc}V^* - V_{pcc}^2)(X_1 - V_{pcc}m_1)}{(X_1 - V_{pcc}m_1)(X_2 - V_{pcc}m_1)} \\
&= \frac{V_{pcc}V^*X_2 - V_{pcc}^2V^*m_1 - V_{pcc}^2X_2 + V_{pcc}^3m_1}{X_1X_2 - X_1V_{pcc}m_1 - X_2V_{pcc}m_1 + V_{pcc}^2m_1^2} \\
&\qquad - \frac{[V_{pcc}V^*X_1 - V_{pcc}^2V^*m_1 - V_{pcc}^2X_1 + V_{pcc}^3m_1]}{X_1X_2 - X_1V_{pcc}m_1 - X_2V_{pcc}m_1 + V_{pcc}^2m_1^2} \\
&= \frac{V_{pcc}V^*(X_2 - X_1) - V_{pcc}^2(X_2 - X_1)}{X_1X_2 - X_1V_{pcc}m_1 - X_2V_{pcc}m_1 + V_{pcc}^2m_1^2}
\end{aligned} \tag{A.8}
$$

Finally, the reactive power sharing error is simplified to Eq.A.9 for a two-source microgrid with the assumptions stated previously.

$$
Q_1 - Q_2 = \frac{V_{pcc}(X_2 - X_1)(V^* - V_{pcc})}{X_1X_2 - X_1V_{pcc}m_1 - X_2V_{pcc}m_1 + V_{pcc}^2m_1^2} \tag{A.9}
$$

From Eq.(A.9) it is clear that the reactive power sharing error is related to the parameters below. However, the control of these parameters is difficult. Chapter 7 investigates these parameters through simulation.

1. $V_{pcc}$: The voltage at the PCC cannot be directly controlled with local DRs.
2. $X_1$, $X_2$ and $X_2 - X_1$: The feeder impedances and their differences are unknown locally and they are uncontrollable parameters.

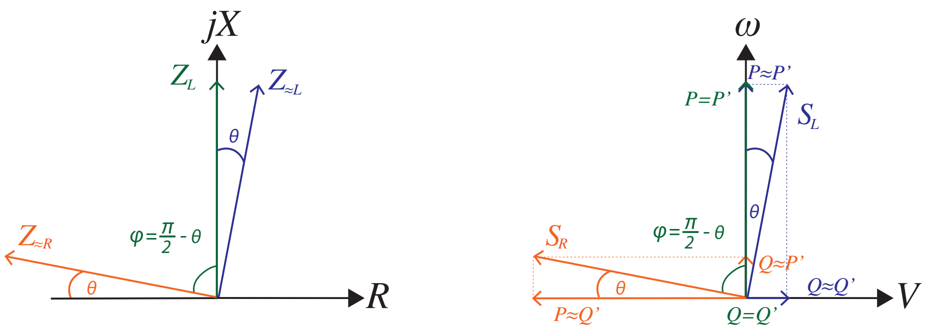


**a.** Resistive to Inductive line impedance. **b.** Relationship between $P, Q, V, \omega$.

**Figure A.1** Effect of the Orthogonal Rotational Linear Transformation.

3. $m_1$: Although an increase in the droop slope would be able to reduce the error, it cannot be chosen to be arbitrarily large without compromising the voltage quality and affecting the microgrid stability [44].

## A.3 Orthogonal Linear Rotational Transformation

One of the challenges a resistive-dominant line impedance imposes on a microgrid is the undesirable coupling between the active and reactive power. This jeopardises the ability of the droop controllers to control the active and reactive power independently through frequency and voltage. Dr. Brabandere proposed a transformation technique based on the line impedance $R/X$ ratio to decouple the active power and reactive power by using an orthogonal matrix $\mathbf{T}$ [50]:

$$\begin{bmatrix} P' \\ Q' \end{bmatrix} = \mathbf{T} \begin{bmatrix} P \\ Q \end{bmatrix} = \begin{bmatrix} \cos\phi & -\sin\phi \\ \sin\phi & \cos\phi \end{bmatrix} \begin{bmatrix} P \\ Q \end{bmatrix} = \begin{bmatrix} \frac{X}{Z} & -\frac{R}{Z} \\ \frac{R}{Z} & \frac{X}{Z} \end{bmatrix} \begin{bmatrix} P \\ Q \end{bmatrix} \tag{A.10}$$

where $\phi = \frac{\pi}{2} - \theta$, $\theta = \arctan X/R$ and $R, X$ are the resistive and inductive components of the line impedance respectively.

Figure A.1 (a) shows that an orthogonal rotation is able to convert a resistive-dominant line to an inductive-dominant line. By rotating the impedance by $\frac{\pi}{2}$, the resistive line impedance becomes inductive. This is means that for an line impedance of $-R+jX$, it becomes $X+jR$ after the transformation. Taking it one step further, by rotating the impedance by $\frac{\pi}{2}-\theta$, the impedance becomes purely inductive.

For a resistive-dominant line, $P \propto V$ and $Q \propto f$, as shown in Figure A.1 (b). The frame transformation implies that the projection of the apparent power onto the V axis becomes $Q'$, whereas the projection onto the $\omega$ axis becomes $P'$. This means that with a resistive-dominant line, there is a coupling between the active power and reactive power, i.e. $P \approx Q'$ and $Q \approx P'$.

However, by transforming the $P, Q$ matrix using the matrix $\mathbf{T}$, the orange vectors (resistance-dominant) become the green vectors (inductive) in Figure A.1 (b). This is effective since the orthogonal matrix preserves the magnitude and angle of the vector it is being multiplied to. This is observed in Figure A.1 (b), where the vector itself is not changed, but only its reference. In addition, since matrix multiplication is simply a linear transformation, the application of such is very intuitive.

Therefore, as before, by assuming a small $\delta$ and $X \ll R$, the application of the frame transformation results in:

$$\begin{aligned} P' &= \frac{E_1 E_2}{R}\,\delta \\ Q' &= \frac{E_1}{R}(E_1 - E_2) \end{aligned} \tag{A.11}$$

In other words, the active power $P'$ can be controlled by $\delta$, and reactive power $Q'$ can be controlled by the voltage, similar to the conventional droop control defined in Eq.(2.3) and Eq.(2.6). This can be easily extended for the droop equations; however, knowledge of the line impedance characteristic (the ratio of $R/X$) is necessary in controlling the active power and reactive power:

$$\begin{aligned} \omega - \omega_0 = -m_p \times (P' - P'_0) &= -k_p \frac{X}{Z}(P - P_0) + k_p \frac{R}{Z}(Q - Q_0) \\ V - V_0 = -m_q \times (Q' - Q'_0) &= -k_q \frac{R}{Z}(P - P_0) - k_q \frac{X}{Z}(Q - Q_0) \end{aligned} \tag{A.12}$$

It is important to note that since the lines cannot be purely resistive or inductive, there will still be a small link between the active and reactive power. The amount of coupling is dependent on the estimation of the line impedance angle $\theta$, where the smaller it is, the more decoupled $P, Q$ can become. However, since the frame transformation only decouples $P, Q$, the unequal line impedance is not compensated. Therefore, an unproportional load sharing may still occur.

It is noted by *Rowe et al.* [71] that this orthogonal matrix $\mathbf{T}$ cannot eliminate the cross-coupling between the active and reactive power when the impedances for $R$ and $X$ are comparative to one another. However, it is able to allow the frequency to control reactive power and voltage to control active power when $R$ becomes more dominant than $X$. For example, the transformation ensures that $P' \approx P$ and $Q' \approx Q$ and for resistive lines $P' \approx Q$ and $Q' \approx P$.

# APPENDIX B

## The Set-up of the Example Microgrid

This appendix includes additional information on the the Example Microgrid set-up in the the laboratory as well as in the simulation. The photographs, component ratings, three-phase wiring diagram and a complete list of instrumentation are included. The settings for the simulation environment in Simulink is also included.

### B.1 The Experimental Set-up

Figure B.1 shows the three-phase wiring diagram of the Example Microgrid in the Genmin Laboratory of University of the Witwatersrand. The prime movers are in the lightest shade, the islanded microgrid is the second lightest and the PCC is shaded with a middle grey that is on the left-hand side of the patchboard. The apparatus involved with the speed and voltage set-points have darker shades.

Figure B.2 is the photo of the set-up, where the apparatus have black labels and the measurements have white labels. The resistor load is the furtherest from the set-up, therefore its location is indicated with an arrow instead of physically shown in the photo. One side of the patchboard (the PCC) is shown, whereas the other side is located near the resistive load on the north side of the laboratory. The unlabelled equipment do not form part of the Example Microgrid experimental set-up.

Figure B.3 shows the SGs set-up, where the equipment also have black labels and measurements have white labels. The list of instruments and list of equipment are included in Table B.2 Table B.1 respectively.

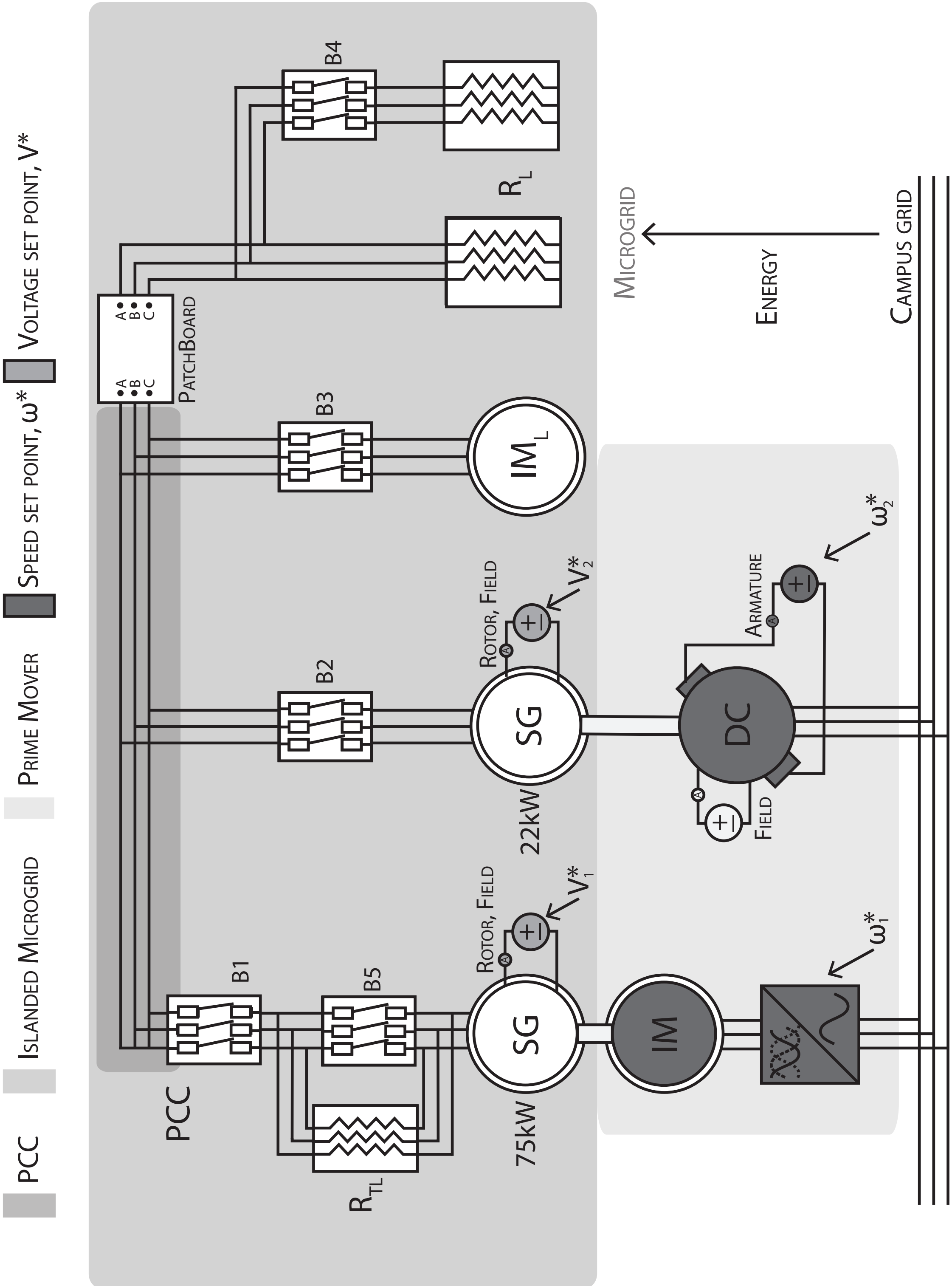


**Figure B.1** Complete wiring diagram of Example Microgrid.


**Figure B.2** Photo of the Example Microgrid laboratory set-up.

**Table B.1** Experimental set-up

| | | | |
|---|---|---|---|
| **75 kW SG Set-Up** | | | |
| Apparatus | | Type | Instrument no. |
| Inverter | : | 45 kW, 400 V, Model CIMR-P5C4045 | 184344 |
| Induction motor | : | 100 kW, 380 V | - |
| SG | : | 75 kW, 380 V, 138 A, 1500 rpm, Rotor at 422 V, 110 A | - |
| SG field | : | 220 V, 50 A variac | VAR 2-3 |
| SG field | : | 220 V, 50 A variac | VAR2-4 |
| Series Resistor Bank | : | 3 × 1.1 Ω, 128 V/resistor | - |
| Circuit breaker B1 | : | CBI F15D, 600 V, 15 kA | - |
| Circuit breaker B5 | : | Hy-Mag SF3-G3, 415 V, 50 A | - |
| **22 kW SG Set-Up** | | | |
| Apparatus | | Type | Instrument no. |
| DC Motor | : | 60 kW, 220 V, 300 A, 1500 rpm, Excitation 180 V, 40 A | - |
| Motor field | : | 380 V, 30 A variac | w054315 |
| Motor armature | : | 380 V, 30 A variac | w041869 |
| SG | : | 22 kW, 380 V, 1500 rpm | |
| SG field | : | 220 V, 30 A variac | VAR 1-3 |
| SG field | : | 220 V, 30 A variac | VAR 1-4 |
| Circuit breaker B2 | : | CBI F15D, 600 V, 15 kA | - |
| **Loads** | | | |
| Apparatus | | Type | Instrument no. |
| Resistive Load | : | Configurable Resistor Banks | - |
| Circuit Breaker B4 | : | 50 A | - |
| Patchboard | : | WD-1 | - |
| Inductive Load | : | SCIM, 5.5 kW, 400 V, 1500 rpm | - |
| Circuit Breaker B3 | : | 50 A | - |

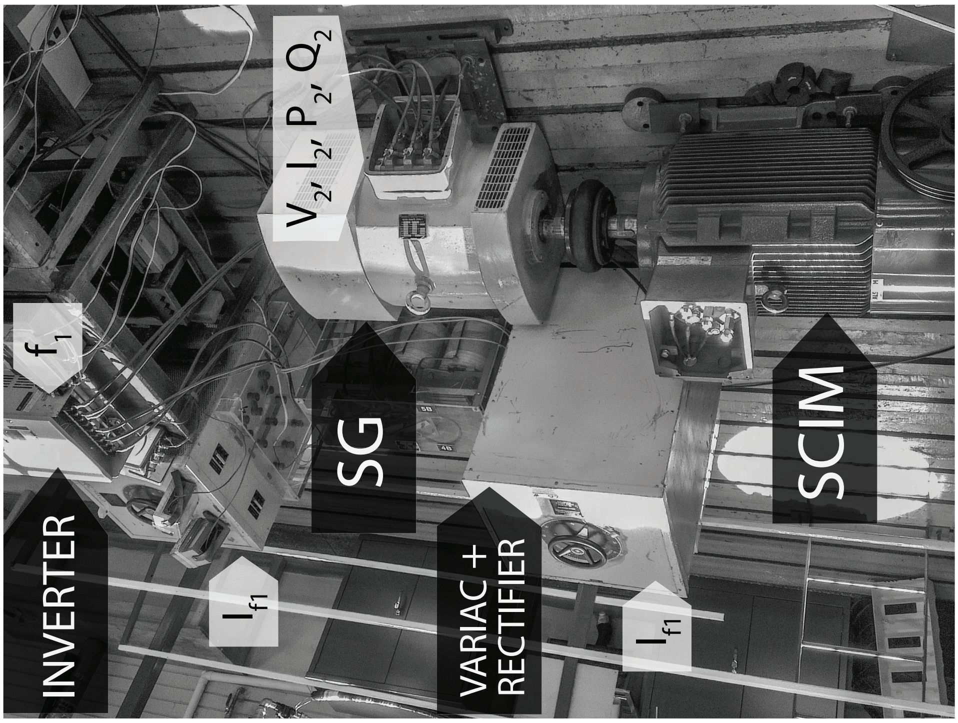


**a.** 75 kW SG laboratory set-up.

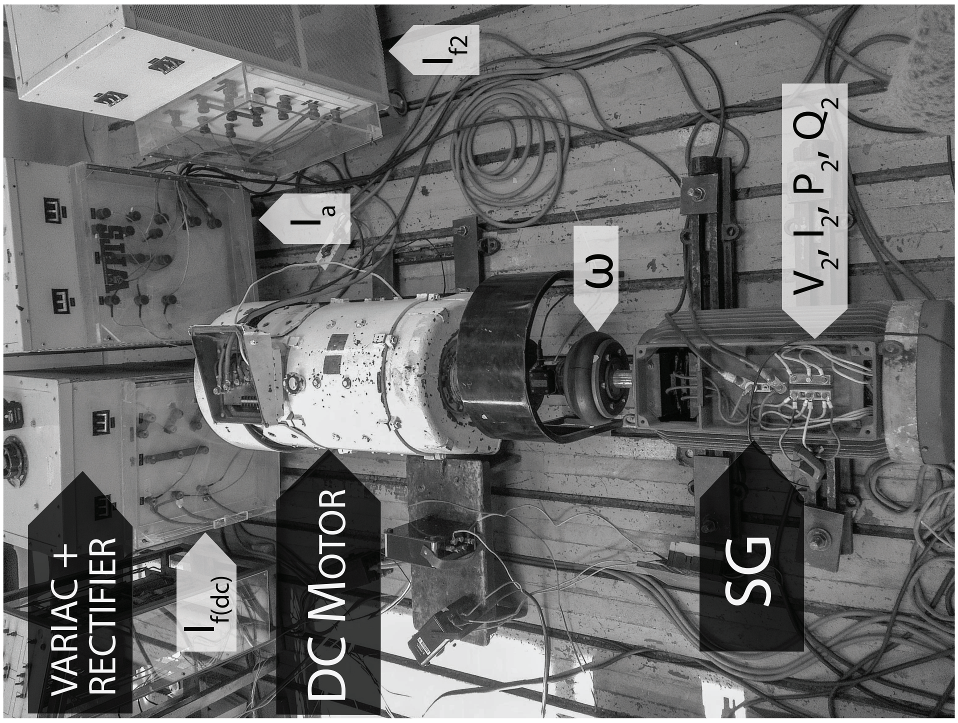


**b.** 22 kW SG laboratory set-up.

**Figure B.3** Photos of the SG Laboratory set-up.

**Table B.2** List of instruments.

| **75 kW SG Instrumentation** | | | | |
|---|---|---|---|---|
| Measurement | | Instrument | Type | Instrument no. |
| $f_1$ | : | Inverter | inverter set-point | 184344 |
| $I_{f1}$ | : | Ammeter | DC analogue, 50 A | 7-15 |
| $I_{f1}$ | : | Ammeter | DC analogue, 50 A | 7-24 |
| $V_1, I_1, P_1, Q_1$ | : | Power Analyzer | Yokogawa CW240 | MC-759 |
| $V_{pcc}, I_{1A}$ | : | Osc. scope | Rigol 1064B | MC-589 |
| **22 kW SG Instrumentation** | | | | |
| Measurement | | Instrument | Type | Instrument no. |
| $I_a$ | : | Voltmeter | 50 mV=100 A | 8-22 |
| $I_{f2}$ | : | True RMS Clamp | Fluke 336 | MC-611 |
| $T_2$ | : | Multimeter | MajorTech MT1881 | MC-726 |
| $V_2, I_2, P_2, Q_2$ | : | Power Analyzer | Yokogawa CW240 | MC-759 |
| $\omega$ | : | Stroboscope | Daelo 1009 | MC-325 |
| $V_{pcc}, I_{2A}$ | : | Osc. scope | Rigol 1064B | MC-589 |
| **Additional Instrumentation** | | | | |
| Measurement | | Instrument | Type | Instrument no. |
| DC motor $I_f$ | : | Voltmeter | DC analogue | 8-43 |
| $IM_L : V, I, P, Q$ | : | Power analyzer | Fluke 41B | MC-260 |
| $I_{IM_A}, I_{pcc}$ | : | Osc. scope | Rigol 1064B | MC-589 |

### Resistor Bank Configuration

The 3-phase resistor bank is located on the north wall of the laboratory, where 10 wound resistors can be connected in variations of series and parallel to achieve different resistances with the position of 11 knife switches. Each resistor is $\approx 6.35\,\Omega$ and the maximum voltage across each resistor is 128 V.

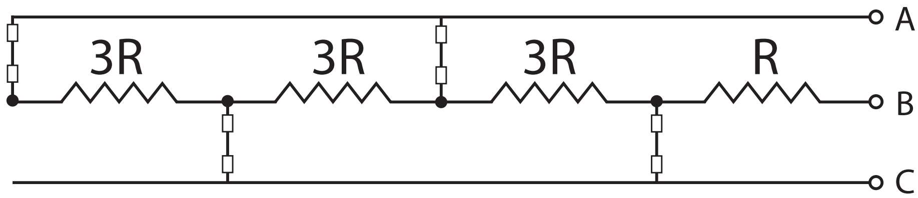


**a.** 6.75 Ω configuration.

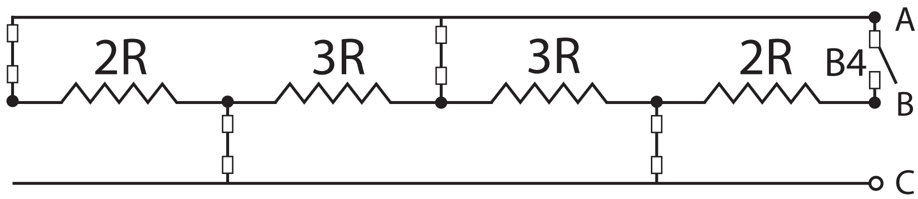


**b.** Step load configuration.

**Figure B.4** Resistor bank resistance configurations.

Figure B.4 (a) shows the resistor bank configuration for the steady-state tests, where three sets of series resistors (3R, 3R, 3R) are connected in parallel and the last resistor is not connected.

Figure B.4 (b) shows the resistor bank configuration for the transient tests. With breaker B4 open, the resistance is three sets of series resistors (2R, 3R, 3R, 2R) connected in parallel, while when breaker B4 is closed, the resistance is four sets of series resistors connected in parallel. Table B.3 tabulates the theoretical and measured resistances with the configurations shown in Figure B.4.

**Table B.3** Theoretical and measured resistances.

| | **Steady- State** | **Transient** | |
|---|---|---|---|
| | | Open B4 | Closed B4 |
| Theoretical (Ω) | 6.50 | 5.57 | 3.90 |
| Measured (Ω) | 6.35 | 4.81 | 3.07 |

## B.2 The Simulation Set-up

**Table B.4** Simulation configuration.

| | | |
|---|---|---|
| **Solver Options** | | |
| Type | : | Variable-step |
| Solver | : | ode23t |
| Max. step size | : | auto |
| Relative tolerance | : | 1e-4 |
| Min. step size | : | auto |
| Absolute tolerance | : | auto |
| Initial step size | : | auto |
| Shape preservation | : | Disable All |
| Solver reset method | : | fast |
| Numer of consequtive min steps | : | 1 |
| **Zero-crossing options** | | |
| Zero-crossing control | : | Use local settings |
| Algorithm | : | Non-adaptive |
| Time tolerance | : | 10*128*eps |
| Signal threshold | : | auto |
| No. consecutive zero crossings | : | 1000 |
| **Power GUI** | | |
| Method | : | Continuous |
| Solver Type | : | Tustin/Backward Euler |

# APPENDIX C

## The SG Model Set-up

This appendix includes additional information with regards to the SGs models used in this research. Firstly, the parameter estimation procedure of the SGs are presented. Then the results of the SG load test are included, where the parametrisation voltage is 180 $V_L$. Finally, the trade-offs between the *asynchronous machine* and *synchronous machine* Simulink block are discussed.

### C.1 Parameter Estimation the Generators

The SGs are the primary components that are being investigated in this research. Since the control system is a possible application of this research, the machine parameters are to be as close to reality as possible. Any mismatch between the estimated parameters used in designing the control strategies and actual parameter values in the SGs leads to an ineffective system. A standard simulink block is used to simulate the SG, where three tests are performed to obtain the electrical parameters and one test to obtain the mechanical parameters. This section describes the model, tests and results obtained for the 75 kW and the 22 kW SGs.

#### C.1.1 Simulation Model

A *wound-rotor asynchronous machine* block is used to simulate the SG in the synchronous reference frame. The electrical part is represented with a fourth-order dq-state space model, as shown in Equation C.1 [6]. The stator and rotor voltages are $v_{qs}, v_{ds}$ and $v_{qr}, v_{dr}$ respectively, while the stator and rotor currents are $i_{qs}, i_{ds}$ and $i_{qr}, i_{dr}$ respectively.

$$\begin{bmatrix} v_{qs} \\ v_{ds} \\ v_{qr} \\ v_{dr} \end{bmatrix} = \begin{bmatrix} \frac{d}{dt}(R_s + L_s) & 0 & \frac{d}{dt}L_m & 0 \\ 0 & \frac{d}{dt}(R_s + L_s) & 0 & \frac{d}{dt}L_m \\ \frac{d}{dt}L_m & -\omega_r L_m & \frac{d}{dt}(R_r + L_r) & -\omega_r L_r \\ \omega_r L_m & \frac{d}{dt}(L_m) & \omega_r L_r & \frac{d}{dt}(R_r + L_r) \end{bmatrix} \begin{bmatrix} i_{qs} \\ i_{ds} \\ i_{qr} \\ i_{dr} \end{bmatrix} \tag{C.1}$$

The mechanical part of the model is represented with a second-order system, as shown in Equation C.2 [57]:

$$T_m = J\ddot{\theta_m} + B\dot{\theta_m} + T_L \tag{C.2}$$

$T_m$ is the electromechanical torque developed by the motor, $T_L$ is the load torque, $\theta_m$ is the angular displacement. The variables include the moment of inertia and friction coefficient, denoted as $J, B$, respectively. The equivalent circuit model in the dq-frame is shown in Figure C.1.

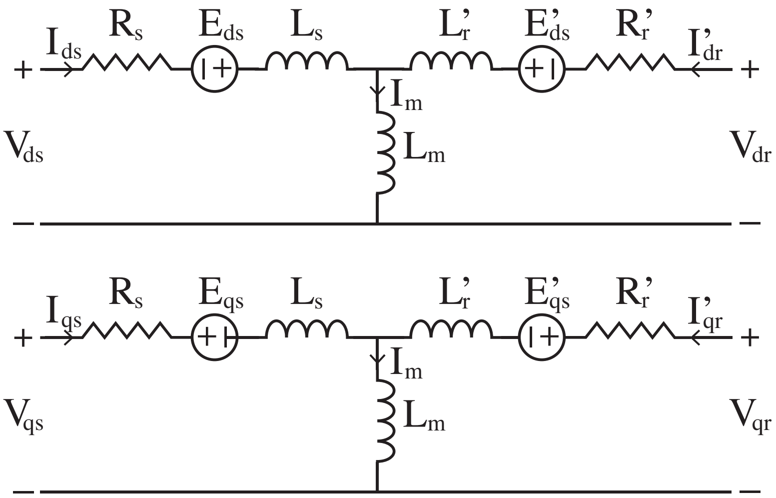


**Figure C.1** Equivalent circuit of an induction machine in the dq-frame, adapted from Figure 4.5-1 from *Krause et al.* [6].

### C.1.2 Electrical Parameters

Three tests are done to estimate the electrical parameters of a separately-excited SG: (1) stator and rotor resistance estimation, (2) leakage inductance estimation and (3) magnetising inductance estimation. This section describes the procedures of the aforementioned tests, while the results are tabulated in Table 5.1, Chapter 5.

### Stator and Rotor Resistance Estimation

A DC power supply is connected to any two terminals of the stator and the stator resistance is calculated by measuring the DC voltages and currents [72]:

$$R_s = \frac{1}{2}\frac{V_{DC}}{I_{DC}} \tag{C.3}$$

The average of three-sets of measurements are used as the stator resistance. The rotor resistance is obtained with the same procedure. The stator is open-circuited while obtaining the rotor resistances, whereas the rotor is open-circuited while measuring the stator resistances.

### Stator and Rotor Leakage Inductance

The stator and rotor leakage inductance is obtained by neglecting the magnetising path. Two phases of the SG is energised with an AC voltage at parametrised frequency and reduced voltage. The SGs are energised at 25 Hz and 60 V for this research. Since the magnetising branch is much larger, it is assumed that the majority of the current applied to the stator flows through the stator and rotor resistance and inductance. The leakage inductance is calculated as follows [72]:

$$L_s + L_r = \frac{Q_{AB}}{2\omega I_{AC}^2} \tag{C.4}$$

where $Q_{AB}$ is the reactive power at terminals A and B, $I_{AC}$ is the current that flows in terminal A and C and $L_s \approx L_r$. This test is also repeated three times for terminals AB, BC, and AC and the average is recorded as the leakage inductance value.

### Magnetising Inductance Estimation

The magnetising inductance is a function of the stator voltage [72], therefore this test should be performed under the Example Microgrid operating voltage. The magnetising inductance is obtained with the separately-excited SG operating as a squirrel-cage induction generator with the rotor short-circuited. Under no-load conditions, the magnetising inductance is assumed to be dominant since the majority of the current flows through the magnetising branch as the rotor impedance approaches infinity ($R_r/s \rightarrow \infty$).

The SG is running at no-load as a squirrel-cage induction machine, at 120 $V_L$ and 25 Hz ($s \approx 0$). The stator and rotor leakage inductance is calculated as follows [72]:

$$L_m = 3\frac{|V_{fe}|^2}{\omega_s Q_{L_m}} \quad \text{(C.5a)}$$

$$Q_{L_m} = Q_s - 3\omega_s L_s |I_s|^2 \quad \text{(C.5b)}$$

$$V_{fe} = V_s - (R_s + j\omega_s L_s) I_s \quad \text{(C.5c)}$$

where $V_s, I_s, Q_s$ are the stator voltage, current and apparent power respectively and $\omega_s$ is the angular speed of the motor. The reactive power and current are measured with the Yokogawa power meter described in Chapter 4. Since the magnetising inductance is a function of the stator voltage and frequency, it is only accurate around the parametrised conditions, i.e. at 120 $V_L$ and 25 Hz.

### C.1.3 Mechanical Parameters

A run-down test estimates the moment of inertia for the SGs. The run down test is performed by allowing the machine to run at synchronous speed under steady state, then the supply voltage is cut off, allowing the machine to slow down to stand still. This section discusses the procedure of the run-down test performed on both the 22 kW and 75 kW SG.

#### 22 kW SG Run-Down Test

The 22 kW SG run down test is conducted as follows: the DC motor's armature voltage is increased until the shaft speed reaches 750 rpm, and the field voltage of the SG is increased to 180 $V_L$. The DC armature voltage is disconnected, allowing the two machines to free wheel. Instead of the rotational speed, the SGs' terminal voltage is measured during the run down since it is directly proportional to the speed, as seen in Figure C.2 (a).

Since there is a DC machine coupled with the SG, only the no load power of the two machines combined can be measured and the no-load power of the SG can be inferred, but not directly measured. To bypass this problem, the 75 kW motor-generator set of SG is used to provide the mechanical power to the SG under experiment. The armature voltage of the DC machine is increased until the torque delivered from the DC machine to the SG is approximately zero. This means that the 75 kW motor is only loaded by the SG. The no load power is measured with the Yokogawa power meter of the 75 kW set as $P_{NL} = 670\,W$.

**75 kW SG Run-Down Test Set Up**

The 75 kW SG run down test is conducted as follows: the inverter drives the induction machine at 25 Hz, and the shaft speed is slightly less than 750 rpm due to slip. The SG field voltage is increased to 180 $V_L$. At steady-state, the inverter is switched off, allowing the two machines to free wheel. Similar to the 22 kW test set-up, the 75 kW SG's armature voltage is measured during the run down, as seen in Figure C.2 (b).

Due to the coupled-nature similar to the 22 kW SG explained previously, the 22 kW motor-generator set is required to provide the 75 kW with the mechanical power for the no-load test. The inverter drives the DC machine at 25Hz to decouple itself from the test. The no-load power is measured with the Yokogawa power meter of the 22 kW set at $P_{NL} = 720\,W$.

**Results**

When the machine is disconnected from the voltage excitation, the rotational motion can be described as [73]:

$$-T_f = J\frac{d_{\omega_m}}{dt} \tag{C.6}$$

where $T_f$ is the frictional torque and $\omega_m$ is the angular speed of the machine. Since $P = T\omega$ and at no-load $\omega_m = \omega_{NL}$, Eq.C.6 can be written as [73]:

$$P_m = J(\frac{\pi}{30})^2 N_{NL}(\frac{dN}{dt})|_{N=NL} \tag{C.7a}$$

$$P_m = P_{NL} - P_{cu} \tag{C.7b}$$

where $P_m$ is the mechanical losses, $N_{NL}$ is the no-load speed in rpm and $P_{cu}$ is the $I^2R$ losses of the windings. $\frac{dN}{dt}$ is the tangential at the no-load rated speed of the run-down curve, as shown in Figure C.2 (a) and Figure C.2 (b).

The field currents of both SGs are insufficient in achieving a terminal voltage of 180 $V_L$, therefore the measured data started from a lower value. The approximated exponential curve is represented with Eq.(C.8), where $y_1$ is the y-intercept and $\tau$ is the steepness factor. Since the SGs are parametrised at 180 $V_L$, $y_1 = 180$ and $\tau$ is obtained heuristically. The tangent curve has the y-intercept also at $y_1$ as shown in Eq.C.9, where $m$ is the gradient of the curve.

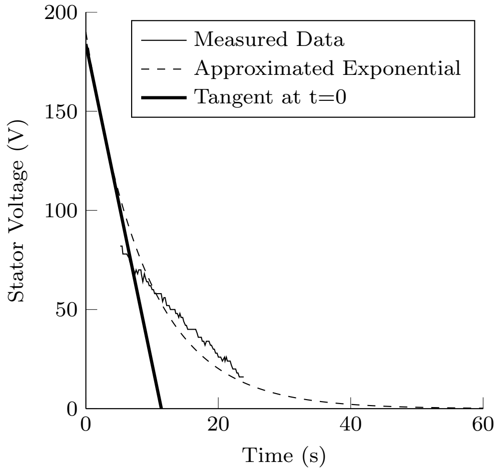


**a.** 22 kW SG run-down test.

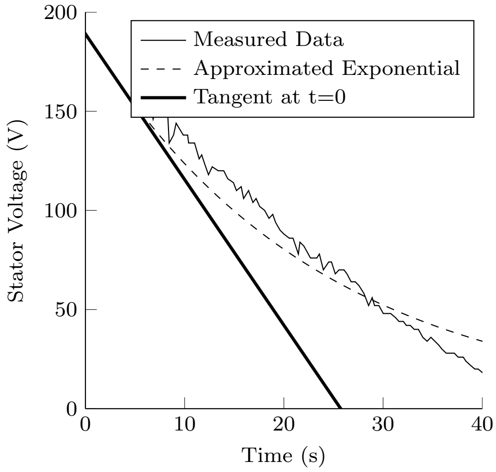


**b.** 75 kW SG run-down test.

**Figure C.2** SG run down tests.

$$\text{exponential curve} = y_1 \times e^{-\tau t} \tag{C.8}$$

$$\frac{dN}{dt} = mt + y_1 \tag{C.9}$$

The exponential curve assumes minimal friction and windage losses, therefore it has an exponential decay in speed. However, it can be seen in Figure C.2 that the measured curve has a strong braking torque with high friction and windage losses, hence it is almost linear. It is clear that this simplification is not ideal since the approximated curve has a large deviation from the measured results, where the estimation of the settling time is especially poor due to the high braking torque.

From the no-load tests, the no-load powers are 720 W and 670 W for 22 kW and 75 kW SG, respectively. The moment of inertia of the machines calculated using Eq.(C.7b) are $0.252\,kg.m^{-2}$ for the 22 kW SG coupled with DC motor and $1.190\,kg.m^{-2}$ for the 75 kW SG coupled with induction motor as tabulated in Table 5.1, Chapter 5.

It must be noted that this research examines the steady-state load sharing between the SGs, where the moment of inertia concerns mainly the transient response of the SGs. This section allows an approximation of the moment of inertia to allow the transient model to be similar to the physical machine. As an approximation for the steady-state testing the moment of inertia is deemed acceptable; however, for future studies stability and dynamic studies, the SGs have to be re-parametrised with appropriate apparatus and instrumentation.

## C.2 Generator Load Test with Parametrisation Voltage at 180 $V_L$

This section provides additional results of the loaded test described in Section 5.3, Chapter 5. The SGs are loaded with a 6.75Ω resistive load individually. Three different field currents are used to achieve three different back EMFs, where the terminal voltage and current are recorded as comparison as shown in Figure C.3. The testing procedures are identical to the one described in Section 5.3, but the SGs model used in this section is parametrised at 180 $V_L$.

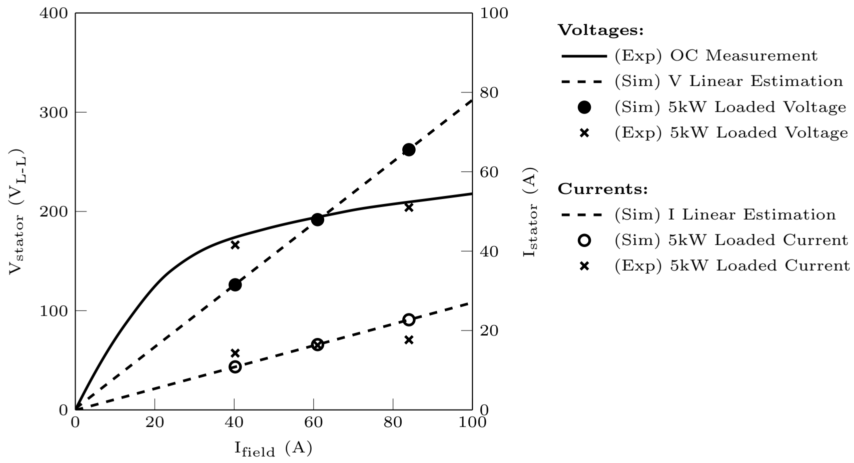


**a.** 75 kW SG characteristics.

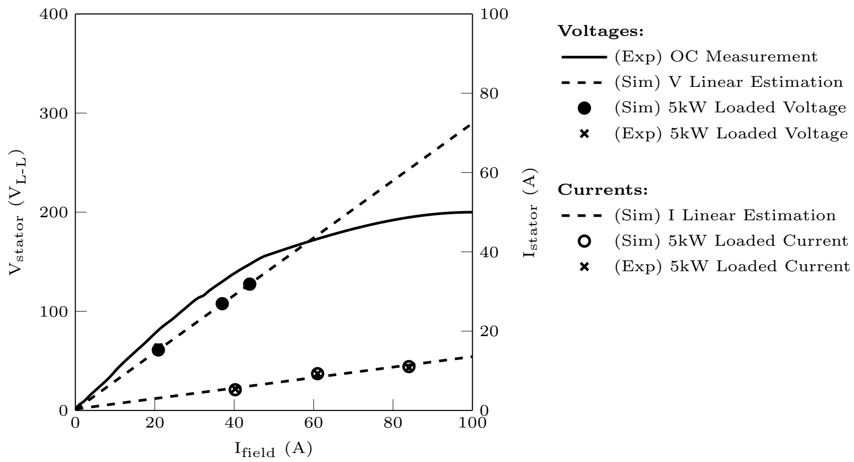


**b.** 22 kW SG characteristics.

**Figure C.3** Comparison of the simulation and experimental results for Load Tests at 180 $V_L$.

The simulation results for the 22 kW machine closely resembles the measured results. This is because even though the saturation is not modelled in the simulation, since the machine saturates at a higher voltage level, the machine has a linear $V_t$ $vs.$ $I_f$ curve at the points measured, as seen in Figure C.3 (b).

The saturation is not modelled in the 75 kW SG, therefore the simulation has a linear $V_t$ *vs.* $I_f$ curve compared to the experimental results that begins to saturate at around 140 $V_L$, as seen in Figure C.3. The simulation is the most accurate when the terminal voltage is sufficiently close to the parametrisation condition, because the magnetising inductance is a variable of the terminal voltage. Therefore, the simulation of the 75 kW machine is the most accurate when the field current is 60 A, and 188.7 $V_L$. Since the model is linear, it is seen that the simulation results undercuts the terminal voltage below and overestimates it above 188.7 $V_L$.

Since the saturation of the SG cannot be modelled (see the next section for detail), the Example Microgrid operating voltage is selected to be at 120 $V_L$, below the saturation voltage ($\approx$140 $V_L$) of the 75 kW SG.

## C.3 Comparison between *ASM* and *SM*

This section aims to compare the difference between the *asynchronous machine* and the *synchronous machine* block in Simulink. The wound rotor asynchronous machine model (ASM) is used to investigate the effect of magnetising inductance on circulating reactive power. The synchronous machine model (SM) is used to identify the relationship between core saturation and terminal voltage.

### C.3.1 Terminal Voltage and Core Saturation

The saturation of the separately-excited SG is not as straight-forward as an induction or a synchronous generator since the air-gap consists of both stator and rotor fields. The *asynchronous machine* model only allows the representation of stator voltage saturation based on stator current, therefore the $V_t$ *vs.* $I_f$ saturation cannot be modelled.

By omitting the magnetising inductance and the rotor impedance based on the model suggested in *McMahon et al.* [61], the equivalent circuit of the DFIG resembles a synchronous machine. Moreover, this research does not use the DFIG for its typical application, but configures it as a synchronous generator. It is therefore a valid simplification to use the synchronous generator model to analyse a DFIG, provided that the rotor/field current is sufficiently large to magnetise the core.

The *synchronous machine* block is used to monitor the saturation effect for the individual load test. The stator voltage saturation is specified according to the open circuit measurement shown in Figure C.4. The saturated *synchronous machine* result is compared with the unsaturated *asynchronous machine* result in Figure C.4.

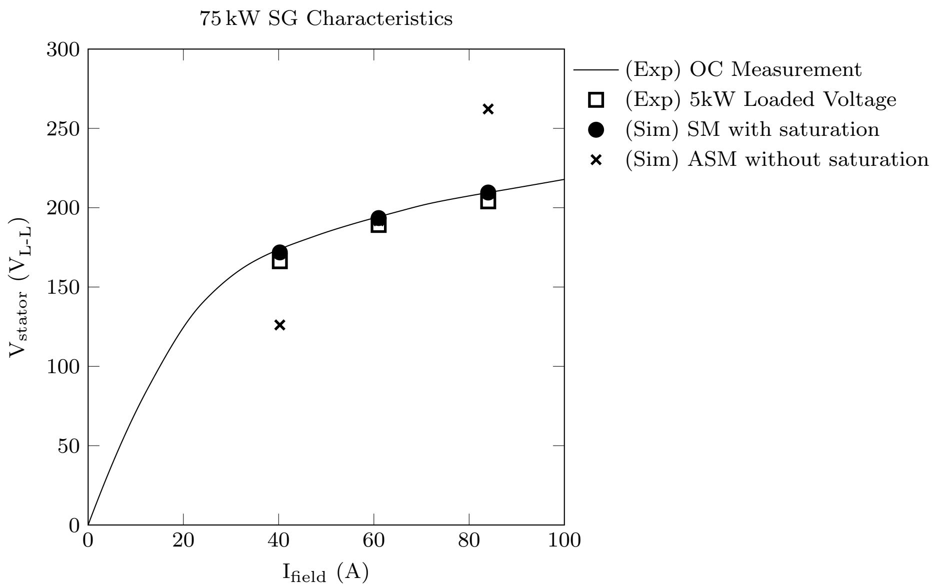


**Figure C.4** Individual Load Test for the 75 kW SG with saturation.

It is clear that in the simulation of the *synchronous machine*, the voltages are saturated, correlating well with the experimental measurements. The simulated voltages are slightly higher than the measured ones since the saturation effect is modelled based on the open circuit measurement. By modelling the saturation of the core, the error reduces from 17.71% to 2.47% between the simulated and measured results.

### C.3.2 Reactive Power, Magnetising Inductance and its Saturation

In the 180 $V_L$ experimental set-up described in Appendix D, the 22 kW generator has a very low excitation voltage and requires the 75 kW generator to supply its magnetising current. However, since the magnetising inductance cannot be modelled with a *synchronous generator* model, the reactive power in the experiment cannot be accurately represented in the simulation.

This effect is also reported in *McMahon et al.* [61], where the authors acknowledge that the error of the model is increasingly worse when the operating voltages (flux densities) are high. It is suggested that the omission of the magnetising branch is only valid when the machine is operated below the saturation point.

This means that the magnetising inductance cannot be ignored during the operating conditions specified, i.e. insufficient excitation for the 22 kW generator and high operating voltage. Therefore, the wound rotor *asynchronous machine* block is used in order to capture the effects of the magnetising reactive current.

However, from the results obtained in Appendix D through the experimental tests conducted, it is realised that the model is unable to represent the machines under all operating conditions. This is because the magnetising inductance is a function of the terminal voltage, and since the core saturation is not modelled, the error cascades.

## C.4 Summary

The use of the *asynchronous machine* and *synchronous machine* blocks creates a trade-off where the former allows the modelling of the magnetising inductance and the latter allows the modelling of $V_t$ *vs.* $I_f$ saturation.

**Table C.1** Field excitation vs. Circulating reactive power.

| **Variables** | $V_t$ | $P_s$ | $P_b$ | $Q_s$ | $Q_b$ |
|---|---|---|---|---|---|
| $E_2 = 0.6\ E_1$ | 104.3 | 2.27 | 2.65 | -2.30 | 4.94 |
| $E_2 = 0.8\ E_1$ | 103.9 | 2.91 | 2.00 | -0.66 | 3.27 |
| $E_2 = 1.0\ E_1$ | 103.8 | 2.90 | 2.02 | 1.06 | 1.42 |

Table C.1 records the simulation results of terminal voltage, active and reactive power of the SGs with various $E_2$. It is seen that by increasing the field current hence raising the terminal voltage, the circulating reactive power can be reduced or eliminated. However, this only solves the problem of circulating reactive power, but not the inaccurate modelling of the saturation. Therefore, instead of raising the terminal voltage of the 22 kW SG, the Example Microgrid voltage is reduced to 120 $V_L$.

Chapter 5 and Chapter 6 show that the Load Tests and the Load Sharing Test at 120 $V_L$. From the results, it is seen that by using the *asynchronous machine* model below the saturation point, the model described and parametrised in this appendix can accurately represent the physical machine.

# APPENDIX D

## Load Sharing Results

This appendix includes additional results of the Example Microgrid load sharing tests at 180 $V_L$ and 120 $V_L$. The reasons for operating the Example Microgrid at 120 $V_L$ is provided by examining the results of the 180 $V_L$ test cases. The role of the digital filter is discussed for the 120 $V_L$ test cases.

### D.1 Load Sharing in Example Microgrid at 180 $V_L$

This section provides additional load sharing test results, which are obtained by operating the Example Microgrid at 180 $V_L$ instead of 120 $V_L$. The testing procedures are identical to the one described in Section 6.2, Chapter 6.

The Example Microgrid is operating at 25 Hz, half of the rated speed of the SGs due to the critical speed limit discussed in Chapter 4. The voltage is halved to accommodate the reduced speed, therefore the Example Microgrid was initially designed to operate at 190 $V_L$. However, due to the output current limitations of the variac, 180 $V_L$ was used. This section aims to demonstrate that the model is unable to accurately represent the physical system at 180 $V_L$, because the saturation of the SG is not modelled and therefore there is an insufficient field current for the 22 kW SG. This section justifies the decision of operating the Example Microgrid at 120 $V_L$ through analysing the results of the load sharing experiments in this section.

#### D.1.1 Set-Up of Load Sharing Test 180 $V_L$

Seven cases are selected with the objective of investigating the Pf- and QV-relationships, as seen in Table D.1, where Cases 1 - 3 have a 5 kW resistive load and Cases 4 - 7 have both a 5 kW resistive and a 1.5 kVAR inductive load. This section examines the correlation between the simulation and the experimental results, while the PF- and QV- relationship are discussed Section D.1.3.

**Table D.1** Description of the test cases at 180 $V_L$.

| **Case** | **1 & 4** | **2 & 5** | **3 & 6** | **7** |
|---|---|---|---|---|
| Loads | R+L (R) | R+L (R) | R+L (R) | R+L (R) |
| Relationship | Pf | QV | Pf | QV |
| InD. Var (Exp) | $DCI_a$ | $I_{f2}$ | $f_{inv}$ | $I_{f1}$ |
| InD. Var (Sim) | $T_2$ | $I_{f2}$ | $T_1$ | $I_{f1}$ |
| D. Var | $P, Q_c$ | $P, Q, Q_c$ | $P, Q_c$ | $P, Q, Q_c$ |
| Constants | $I_{f1}, I_{f2}$ | $T_1, T_2$ | $I_{f1}, I_{f2}$ | $T_1, T_2$ |

Table D.1 summarises the independent and dependent variables of the test cases. The terminal voltage and the torque are the independent variables that control the reactive power and active power respectively. This procedure is identical to the one discussed in Chapter 6. Each case is subjected to three rounds of independent variable adjustments while other variables are kept constant.

### D.1.2 Comparison of Test Results

Case 4 has the DC motor armature current as the independent variable, which controls the coupled shaft speed, hence determines the torque of the 22 kW SG. The torque[1] magnitude increases from 5.47 , 27.50 , 32.44 Nm, while the field currents for both generators are kept constant. Figure D.1 (a) correlates the simulation and the experimental results using the output active and reactive powers of the two SGs.

Case 7 has the 75 kW field current $I_f$ as the independent variable, which determines its terminal voltage as well as influencing the overall bus voltage. The field current decreases from 76.50 , 70.25 , 63.50 A, while the system frequency is kept constant. Similar to Figure D.1 (a), Figure D.1 (b) correlates the simulation and experimental results using the active and reactive powers of both SGs.

Table D.2 and Table D.3 record the experimental and simulation results for Case 4 and Case 7 respectively. It is clear from the Tables and Figures that the measured individual terminal voltages are closely related to the simulated bus voltage, and the output powers are very similar to one another. The reactive power delivered to the load is also identical between the simulated and experimental results, however, the circulating reactive power is a lot higher in the experiments.

[1]Note that the convention adopted in this research is that negative torque means supplying power, while negative reactive power means absorbing reactive power. This means that the 22 kW SG is supplying active power and absorbing reactive power in this case.

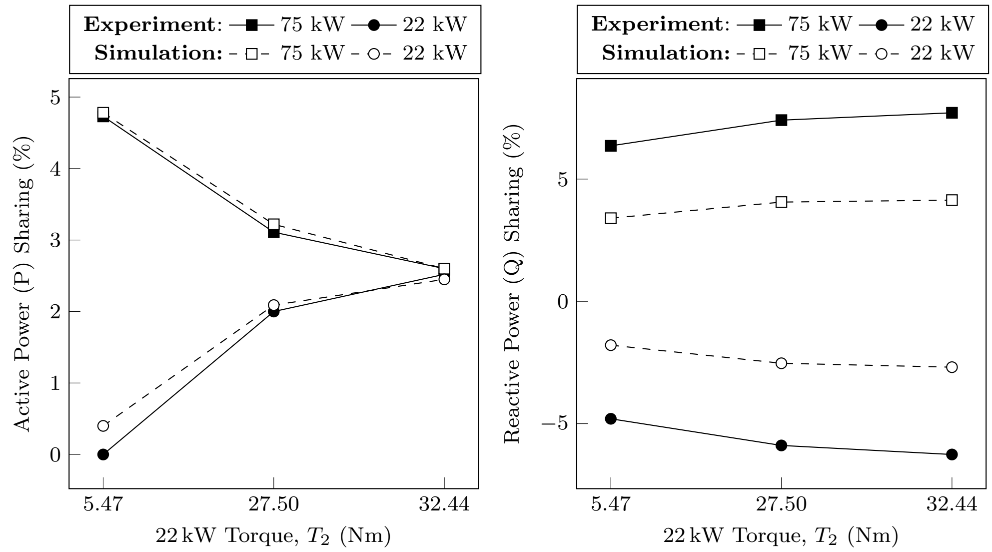


**a.** Case 4.

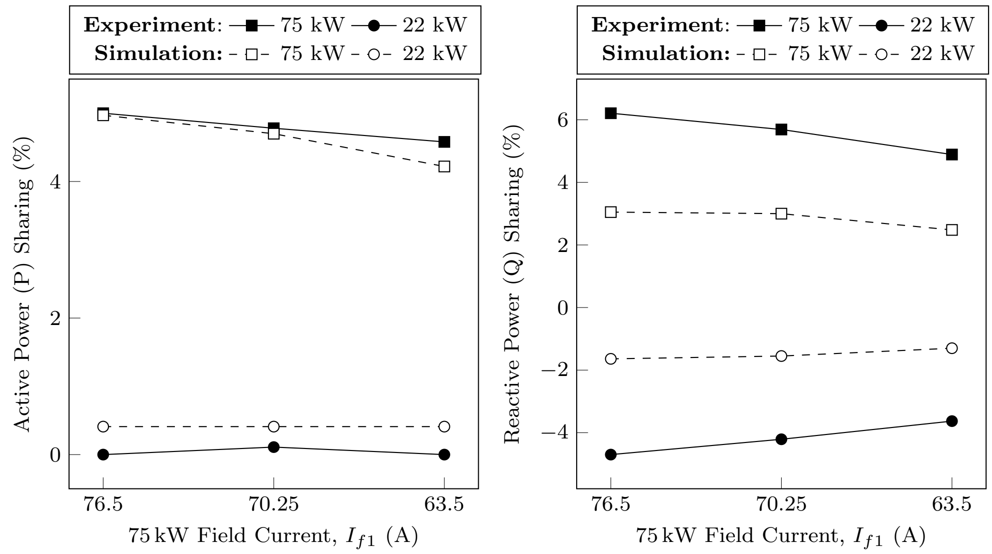


**b.** Case 7.

**Figure D.1** Comparison of the experimental and simulation results for Load Sharing Tests at 180 $V_L$.

**Table D.2** Case 4: Experimental and simulation results.

| Torque (Nm) | **Round 1:** -5.47 | | **Round 2:** -27.50 | | **Round 3:** -32.44 | |
|---|---|---|---|---|---|---|
| SG | Big | Small | Big | Small | Big | Small |
| Exp $V_t$ | 180.0 | 179.2 | 178.7 | 178.8 | 177.1 | 177.8 |
| Sim $V_{bus}$ | 183.1 | | 183.4 | | 179.3 | |
| Exp P | 4.73 | 0.00 | 3.11 | 2.00 | 2.60 | 2.52 |
| Sim P | 4.78 | 0.40 | 3.22 | 2.09 | 2.60 | 2.45 |
| Exp Q | 6.36 | -4.80 | 7.41 | -5.89 | 7.71 | -6.26 |
| Sim Q | 3.40 | -1.79 | 4.06 | -2.53 | 4.14 | -2.69 |

**Table D.3** Case 7: Experimental and simulation results.

| $I_{f(b)}$ (A) | **Round 1:** 76.50 | | **Round 2:** 70.25 | | **Round 3:** 70.80 | |
|---|---|---|---|---|---|---|
| SG | Big | Small | Big | Small | Big | Small |
| Exp $V_t$ | 179.7 | 177.6 | 175.7 | 173.8 | 170.6 | 168.5 |
| Sim $V_{bus}$ | 177.9 | | 175.4 | | 168.7 | |
| Exp P | 5.00 | 0.00 | 4.78 | 0.11 | 4.58 | 0.00 |
| Sim P | 4.97 | 0.41 | 4.70 | 0.41 | 4.22 | 0.41 |
| Exp Q | 6.21 | -4.70 | 5.69 | -4.21 | 4.89 | -3.63 |
| Sim Q | 3.05 | -1.64 | 3.00 | -1.55 | 2.48 | -1.30 |
| Exp $I_f$ | 76.50 | - | 70.25 | - | 63.50 | - |
| Sim $I_f$ | 78.00 | - | 76.50 | - | 70.80 | - |

### D.1.3 Droop Characteristics

This section discusses the droop characteristics based on the results obtained. It is clear from Figure D.1 (a) that varying the torque affects the power sharing between the two SGs. From Round 2 to 3, change of approximately 15% in torque allows the 22 kW SG to pick up 10% more of the load. On the other hand, Figure D.1 (b) shows that $I_f$ has little effect on the active power output, since from Round 1 to 3, a 15% of change in $I_f$ has a minimal effect on the load sharing. It must be noted that although the 75 kW generator has a decrease in power output, it is due to the decrease in bus voltage to the resistor bank ($P = \frac{V^2}{R}$).

The output reactive power in Figure D.1 (a) and Figure D.1 (b) shows that there are large differences between the simulated and the measured results. This discrepancy is attributed to the inadequately modelled magnetising inductance and core saturation, as discussed in Appendix C. From the figures, the reactive power seems to be dependent on both the torque and the voltage; however, a 590% change in torque only results in a 16.3% change in reactive power, whereas a 17.0% change in $I_f$ creates a 21% change in reactive power.

Theoretically, the change in torque has a minimum effect on the reactive power; however, the magnetising current is insufficient in the 22 kW SG to provide for the increased sharing of load without the voltage collapsing. The 75 kW SG is required to provide additional reactive current for voltage support, hence the increase in circulating reactive power.

On the other hand, although the excitation controls the reactive power output of the generators, this is not the reason for changing the reactive power observed in Figure D.1. The decrease in circulating reactive power is because there is a smaller difference between the back emf of the two SGs as the 75 kW $I_f$ decreases. The sharing of the reactive load does not occur in the experiment since the 75 kW SG is providing all the reactive power to the load.

### D.1.4 Analysis and Summary

The Pf-relationship is clearly observed in both the simulation and the experimental, where the power sharing between the two generators can be controlled by varying the speed of each generator. However, the QV-relationship is unclear. The main reason for the circulating reactive power is that the field current of the 22 kW SG is not enough to achieve 180 $V_L$ terminal voltage; therefore, it draws a large magnetising current from the 75 kW SG for voltage support. This means that the 75 kW SG is supplying the inductive load as well as providing voltage support to the 22 kW SG.

It is concluded that since the circulating reactive power is mainly due to the insufficient field current of the 22 kW SG, it can be easily eliminated by either providing a large enough field current or reducing the PCC voltage. This is verified with the experimental results in Chapter 6, where the circulating current is eliminated by operating the Example Microgrid at 120 $V_L$.

This section demonstrates that although the Pf-relationship is confirmed, due to the large magnetising current, the QV-relationship cannot be observed. Therefore, the operating voltage of the Example Microgrid is reduced to 120 $V_L$ as discussed in Chapters 4, 5 and 6.

## D.2 Additional Results of Load Sharing at 120 $V_L$

Figure D.2 compares the original unfiltered results to the results that is processed with the oscilloscope through a 50 Hz filter. It can be seen that the filter successfully extracts the fundamental waveform by filtering out the high-frequency components.

Figure D.3 compares the 5 s waveform to the 20 ms waveform to show the effects of low sampling points on the RMS calculation. It can be seen that the 5 s waveform has a higher peak voltage and current, resulting in the RMS calculated with Eq.(6.2) to also be higher. This may attribute to the error in Section 6.3.3 of Chapter 6.

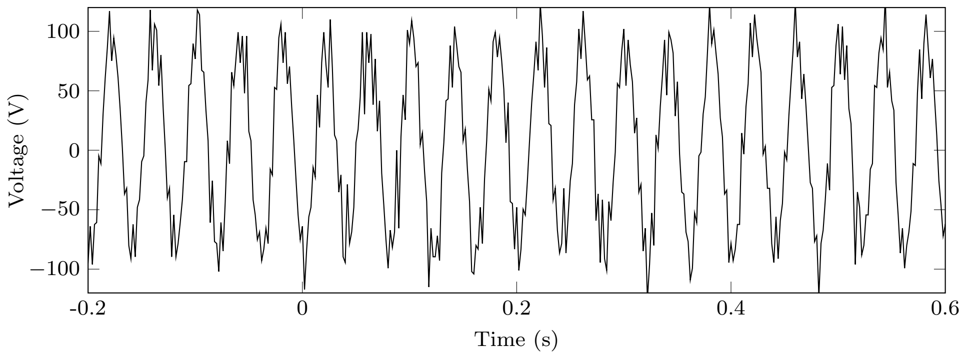


**a.** Unfiltered Signal

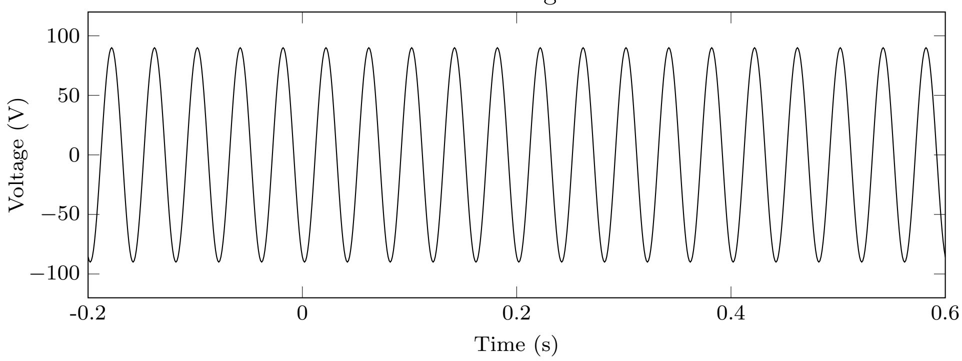


**b.** Filtered Signal

**Figure D.2** Comparison between filtered and unfiltered results

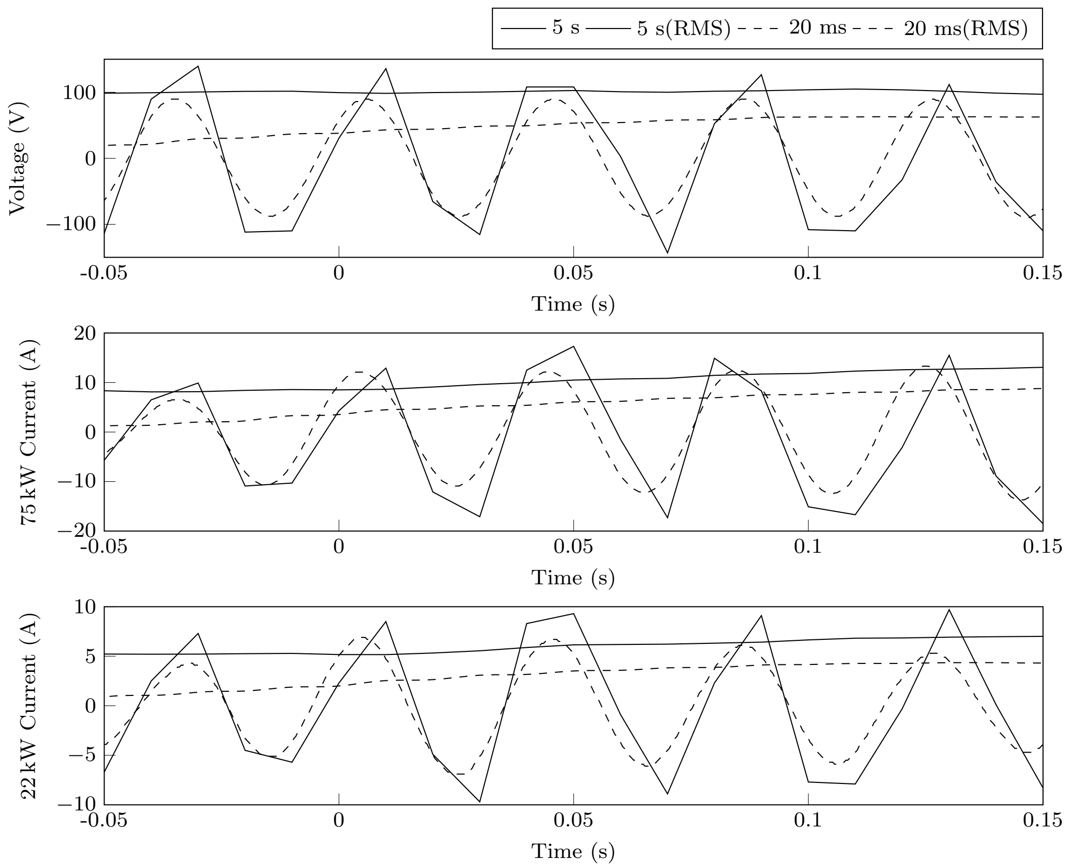


**Figure D.3** Long vs. Short RMS.

# APPENDIX E

## Simulated Transient Behaviour

This appendix includes additional simulation results of the Example Microgrid. The transient load sharing between the SGs is not part of this research, but the transient behaviour of the system is included in this appendix for completeness. The discussion in this section is based on the observation of the simulation results and its correlation to the work of *A.D. Paquette* [29].

### E.1 Impact of Controller Gains on Transient Stability

Figure E.1 illustrates the effect of poorly-tuned controller gains on the transient load sharing. The simulation set-up is identical to Case 2, where there is an equal line impedance between the SGs and the PCC. The controller gains ($k_p, k_i$) are changed, while the droop coefficients remain the same.

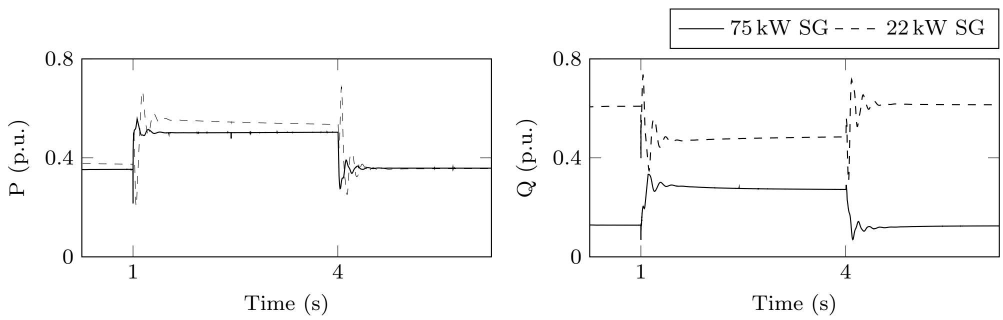


**Figure E.1** Case 10: Increasing controller gains.

The increase in proportional gains allows for a faster tracking and a more responsive controller. However, if the gain is too high an overshoot and instability may occur. Figure E.1 shows that the generators pick up the load as well as reaching steady-state very quickly as compared to Figure 7.5 (b).

For the speed controller in Case 10, the decrease in proportional gain reduces the speed of error tracking, therefore it takes longer to reach a proportional active power sharing. The overshoot is also increased, due to the slow error correction speed.

For the voltage controller in Case 10, it is clear that the increase in proportional gain introduces a significant overshoot and worsens the transient stability as seen in Figure E.1. Similar to the speed controller, the time to steady-state also increases. The controller gain affects only the transient load sharing whilst the steady-state load sharing remains the same in Case 2. However, for a larger step load, it is possible for the system to collapse during transient.

## E.2 Impact of Synchronous Reactance on Transient Load Sharing

With poorly tuned controllers, the transient performance may be severely affected. By magnifying Figure E.1 at the point when the negative step load (loss-of-load) occurs at $t = 4\,\mathrm{s}$, Figure E.2 shows that the smaller SG picks up the majority of the load during the transient period. Figure E.2 shows that both the voltage and current waveforms are sinusoidal and as a load drop occurs, the voltage increases while the current decreases. However, due to the unequal reactive load sharing, the current of 22 kW SG remains approximately constant as it provides the majority of the reactive current.

To explain this effect, for the first few voltage cycles of disturbance, the SGs can be modelled as two ideal voltage sources connected in series with their transient reactance ($X'_d$) [29]. Therefore, it is possible to describe and predict the transient load sharing via:

$$\frac{S_1}{S_1 + S_2} = \frac{X'_{d_1}}{X'_{d_1} + X'_{d_2}} \tag{E.1}$$

The transient reactances ($X'_d$) of the two generators are calculated based on the definition specified by IEEE 115 [74]:

$$X'_d = \frac{E}{I'} \tag{E.2}$$

where $E$ is the open-circuit armature voltage before the short circuit and $I'$ is sum of the transient component before the short circuit and the steady-state component. The two generators' transient reactances are calculated as:

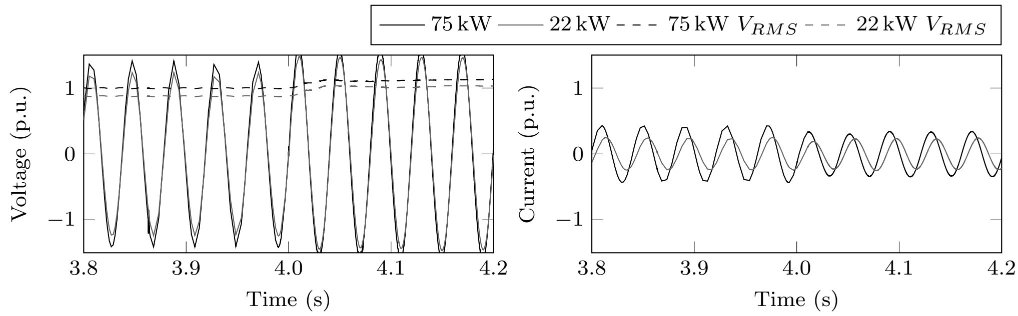


**a.** Voltage and current transient.

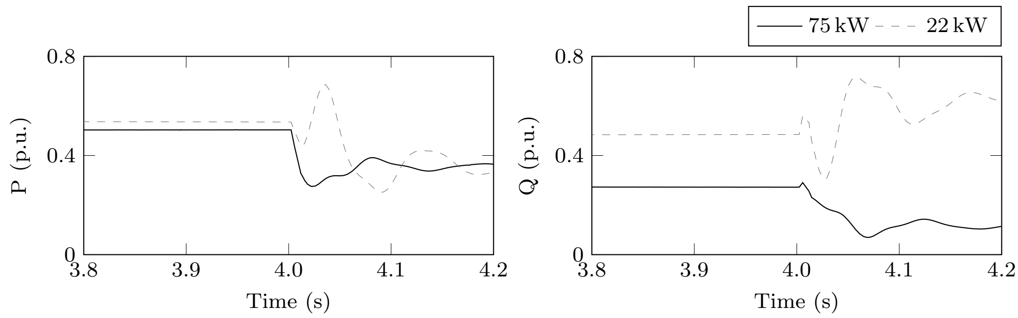


**b.** Active power and reactive power transient.

**Figure E.2** Case 10: Transient response at the negative step load.

$$\begin{aligned} X_{d_1} &= 0.021 \\ X_{d_2} &= 0.058 \end{aligned} \tag{E.3}$$

Eq.(E.4) predicts the load sharing based on the transient reactances. Based on the simulation results in Fig. E.2 (b), Eq.(E.5) calculates the load sharing using the apparent power values at 2.5 cycles after the disturbance. It is clear that the prediction corresponds closely to the simulation result.

$$\frac{X'_{d_1}}{X'_{d_1} + X'_{d_2}} = \frac{0.0211}{0.0211 + 0.0583} = 28.3\% \tag{E.4}$$

$$\frac{S_1}{S_1 + S_2} = \frac{0.3472}{0.3472 + 0.8426} = 29.2\% \tag{E.5}$$

Since the generator ratings are indirectly proportional to their transient reactance, it is inherent that the smaller generator picks up more load during transients. This may overload the generator for a short duration and if the generator ratings are vastly different, it may cause a detrimental effect to the smaller generator.

Through tuning the controller optimally, the poor transient load sharing may be prevented since Case 2 has a slower response time that dampens this effect. In addition, the Example Microgrid has two relatively-sized rotating machines with similar inertias, therefore, the transient stability is less of a concern as compared to a microgrid with both PE- and machine-based generations [32].